UNIVERSITÁ DEGLI STUDI DI PARMA

FACOLTÀ DI SCIENZE MATEMATICHE, FISICHE E NATURALI

DIPARTIMENTO DI FISICA

Numerical simulations of relativistic star oscillations

Gravitational waveforms from perturbative and 3-dimensional codes

Sebastiano Bernuzzi

Supervisor:
Dr. Roberto De Pietri

Tesi sottomessa per il titolo di
DOTTORATO DI RICERCA IN FISICA

Thesis submitted for the award of the degree of
PHD IN PHYSICS

XXI ciclo - January 2009

Contents

List of Figures

List of Tables

Introduction

The computation of the gravitational-wave emission from compact sources like supernova explosions, neutron-star oscillations and the inspiral and merger of two compact objects (like neutron stars or black holes) is one of the most lively subjects of current research in gravitational-wave astrophysics. The final goal of these studies is the theoretical investigation, using numerical simulations, of the dynamical mechanisms in the sources that lead to gravitational radiation emission and the production of the wave templates necessary for the detection in the ground and space-based antennas system (interferometers and resonant bars).

Neutron stars are very compact stars that are born either as the product of gravitational collapse or of the merger of a binary system. They are highly relativistic objects, characterized by magnetic fields and rapid rotation; their internal composition, governed by strong interactions, is, at present, largely unknown. After neutron star formation non-isotropic oscillations are typically present. These oscillations are damped because of the emission of gravitational waves. Although neutron star oscillations do not represent a primary source of gravitational radiation (the most promising system are expected to be binary systems and supernova explosions, and, moreover, for neutron star oscillations, the gravitational wave amplitude strongly depends on the evolutionary process that lead to its formation) their investigation is still very important for, at least, two reasons. First, neutron stars are a unique astrophysical system in which each fundamental interaction, gravity, electromagnetic and nuclear one, play an essential role. The opening of the “gravitational window” in astronomy and the detection of the radiation emitted by neutron star pulsations would lead to observational constraints on high density matter properties and fundamental theories [14]. Second, from a technical point of view, the simulation of a single neutron stars is now a relatively controllable setting in which several degrees of approximation can be introduced to single out and systematically investigate all the different details of the physics as well as the numerical techniques, *e.g.* rotation, internal structure (Equation of State) models, wave extraction methods and evolution schemes for numerical computations.

In principle, only 3D simulations in full nonlinear General Relativity with the inclusion of realistic models for the matter composition (as well as electromagnetic fields) can properly investigate the neutron star birth and evolution scenarios. The first successful steps in this direction have been recently done by different Numerical Relativity groups, *e.g.* [24, 183, 177, 178, 184, 185, 78, 83, 25, 210, 82] (See also the reviews in [126, 37, 176]). The results obtained include the simulations of binary neutron stars system, mixed binaries, gravitational supernova core collapse and neutron star collapse to black hole. In general the perfect fluid approximation with a simplyfied treatment of the nuclear matter (polytropic Equation of State) is employed, but also fundamental aspects as rotation, the use of realistic Equation of State to describe high density matter, micro-physics and neutrinos transport and magnetic fields (ideal magnetohydrodynamics), has been taken into account. However the complexity of the physical details behind the system and the huge technical/computational costs of these simulations are still not completely accessible, and alternative/approximate approaches to the problem are still meaningful.

An approximate route to studying the gravitational radiation emitted by neutron star oscillations is given by perturbation theory, *i.e.* by linearizing Einstein's equation around a fixed background (See *e.g.* Refs. [115, 147]). The perturbative approach has proved to be a very reliable method to understand the oscillatory properties of neutron star as well as a useful tool to calibrate 3D nonlinear numerical codes. In this respect particular success has been obtained recently by time-domain simulations [13, 6, 86, 169, 170, 85, 141, 140, 139, 84, 186, 153, 155] that give direct access to the waveforms. Moreover perturbation theory provide the theoretical background to the development of wave-extraction methods in the Numerical Relativity simulations.

In this thesis we compute, analyze, compare and discuss the gravitational waveforms emitted by non-spherical neutron star oscillations. Our aim is to follow two complementary calculation procedures.

On one hand we follow a perturbative time-domain approach based on linear perturbations of spherical spacetimes. This approach permits the investigation of the radiation from non-rotating star. We developed a new code solving the linearized Einstein equations for all kind of perturbations. Trough a series of simulations we confirm and extend the previous results of Refs. [6, 169] investigating, for the first time, a large sample of realistic Equation of State and of star models, and discussing in detail the properties of the waveforms.

On the other hand, we adopt a full General Relativity 3D approach, *i.e.* we compute a numerical solution of the Einstein equations without approximations except those of the numerical method itself. Another series of simulations within this framework is performed and analyzed with the specific purpose of study the nonlinear effects in the process of neutron star oscillations (as done previously in [79, 155] but using either approximation of General Relativity or second order perturbation theory) and to test the modern wave-extraction techniques. Extracting gravitational waveforms from a spacetime computed numerically in a given coordinate system is, in fact, a highly non-trivial problem that has been addressed in various ways in the literature. In general, two routes have proven successful: (i) The gauge-invariant *curvature*-perturbation theory based on the Newman-Penrose [146] scalar ψ_4, and (ii) the Regge and Wheeler [166], Zerilli [213] theory of *metric*-perturbations of a Schwarzschild space-time, recast in a gauge-invariant framework following the work of Moncrief [137]. This part of the work has much in common with Refs. [180, 157], where a comparison of different extraction techniques has been performed. Following the same inspiration of Ref. [157], we exploit perturbative computations to obtain "exact" waveforms to compare with the numerical-relativity–generated ones. As done in Ref. [180], we use an oscillating neutron star as a test-bed system, but we consider a wider range of possible wave-extraction techniques.

The plan of the thesis is the following. In Chap.1 a review of the basics concepts of relativistic fluid-dynamics necessary for the description neutron stars is presented. Chap.2 introduces some concepts about neutron stars and also the star models and the Equations of State adopted. The perturbation theory and the Einstein equations for linear oscillations of neutron star are treated in Chap.3, togheter with a description of the code to solve them. In Chap.4 we discuss the gravitational waveforms from linear simulations. Chap.5 deals in detail with the current state-of-art techniques to extract gravitational radiation from numerical simulations employed in the simulations. Finally, nonlinear Numerical-Relativity simulations and their comparison with the linear one are discussed in Chap.6.

Units. We use dimensionless units $c = G = M_\odot = 1$, unless otherwise specified for clarity purposes.

Notations. Summation convention over repeated indexes is used. Greek indexes run on $\mu = 0, 1, 2, 3$, Latin indexes run on $i = 1, 2, 3$. Vectors in Euclidean space $\mathbb{R}^N$ are written as $\vec{v}$, 4-vectors on dynamical spacetime $\mathcal{M}$ are $\mathbf{v}$ with components v^μ. The metric tensor signature is $(-, +, +, +)$. The Lie derivative of a vector $\mathbf{v}$ along the vector field $\mathbf{u}$ is written as $\mathcal{L}_\mathbf{v}\mathbf{u}$ while the covariant derivative is $\nabla_\mathbf{v}\mathbf{u}$. Partial derivatives are indicated as $f(x)_{,x}$ or $\partial_x f(x)$.

Some acronyms largely used are: General Relativity (GR), Neutron Star (NS), Gravitational Wave (GW), Equation of State (EOS). Quasi-Normal Mode (QNM).

Publication list

The main results presented in the present thesis have been published in the following journal articles:

- L. Baiotti, S. Bernuzzi, G. Corvino, R. De Pietri and A. Nagar,
  Gravitational-wave extraction from neutron star oscillations: comparing linear and nonlinear techniques
  Phys. Rev. D 79, 024002 (2009)
  arXiV [gr-qc]: http://arxiv.org/abs/0808.4002
- S. Bernuzzi and A. Nagar,
  Gravitational waves from pulsations of neutron stars described by realistic Equations of State
  Phys. Rev. D 78, 024024 (2008)
  arXiV [gr-qc]:http://arxiv.org/abs/0803.3804
- S. Bernuzzi, A. Nagar and R. De Pietri,
  Dynamical excitation of space-time modes of compact objects
  Phys. Rev. D 77, 044042 (2008)
  arXiV [gr-qc]: http://arxiv.org/abs/0801.2090

Chapter 1

Relativistic fluids

A relativistic description of fluid-dynamics is necessary in studying of many astrophysical systems like compact stars, flows around compact objects, jets emerging form from galactic nuclei and gamma-ray burst engines and cosmology. While the description of astrophysical jets can be done within the Special Relativity theory, the strong gravitational field of compact objects and cosmology require the use of the General Relativity theory.

The equations of relativistic hydrodynamics consist of the local conservation laws of the stress-energy tensor (Bianchi identities), the continuity equation for the matter current density and the Equation of State (EOS) of the fluid [88, 97]. In addition, if the electro-magnetic field is considered, the Maxwell equations must be added to the system [19]. The system of equations is a nonlinear system of PDE closed by an algebraic equation, the EOS, and, as mathematical problem, it usually posed as an Initial Value Problem. To obtain a solution usually numerical method are employed, in Numerical Relativity, in particular, the equations are re-written, within the “3+1” ADM formalism [21], in a conservative form that emphasizes their hyperbolic character. In this chapter we give an introduction to General Relativistic Hydrodynamics, a special attention is payed to the “3+1” conservative formulation [31] and to the concept of EOS.

1.1 Definition of stress-energy tensor

In General Relativity the energy and momentum of the matter is described (at a macroscopic level) by a symmetric $(0,2)$ tensor field: $T_{\mu\nu}$. Given an observer $\mathcal{O}$ of 4-velocity $\tilde{\mathbf{u}}$, and given $p^{\alpha}_{\beta} \equiv \delta^{\alpha}_{\beta} + \tilde{u}^{\alpha}\tilde{u}_{\beta}$, the projector to the vector space orthogonal to that generated by $\tilde{\mathbf{u}}$, the following definitions holds:

$$E \equiv T_{\mu\nu}\tilde{u}^{\mu}\tilde{u}^{\nu} \tag{1.1.1a}$$

$$P_{\alpha} \equiv -T_{\mu\nu}\tilde{u}^{\mu}p^{\nu}_{\alpha} \tag{1.1.1b}$$

$$S_{\alpha\beta} \equiv T_{\mu\nu}p^{\mu}_{\alpha}p^{\nu}_{\beta}\,. \tag{1.1.1c}$$

In Eq. (1.1.1) E is the energy density measured by the observer $\mathcal{O}$, P_{α} is the momentum density and $S_{\alpha\beta}$ is the stress tensor.

1.1.1 Perfect fluid approximation

As a model for the matter is often assumed the *perfect fluid*:

$$T_{\mu\nu} = (\varepsilon + p)u_\mu u_\nu + pg_{\mu\nu} \tag{1.1.2}$$

where ε and p are two scalar field and u_μ is a 1-form associated (via the metric tensor) to $\mathbf{u}$: a vector field giving at each point the 4-velocity of the fluid. Considering an observer $\mathcal{O}$ with 4-velocity $\tilde{\mathbf{u}}$, Eq. (1.1.1) in the case of a perfect fluid becomes:

$$\begin{aligned} E &= W^2(\varepsilon + p) - p && \text{(1.1.3a)} \\ P_\alpha &= W^2(\varepsilon + p)U_\alpha && \text{(1.1.3b)} \\ S_{ij} &= p\delta_{ij} + W^2(\varepsilon + p)U^i U^j \ . && \text{(1.1.3c)} \end{aligned}$$

Above W is the Lorentz factor between the fluid frame and the observer and $\mathbf{U}$ is the velocity of the fluid with relative to the observer $\mathcal{O}$. The 4-velocity of the fluid can be expressed as:

$$\mathbf{u} = W\left(\tilde{\mathbf{u}} + \mathbf{U}\right) \ . \tag{1.1.4}$$

In particular in a co-moving frame ($\tilde{\mathbf{u}} = \mathbf{u}$,$W = 1$) we find:

$$\begin{aligned} E &= \varepsilon && \text{(1.1.5a)} \\ P_\alpha &= 0 && \text{(1.1.5b)} \\ S_{ij} &= p\delta_{ij} \ , && \text{(1.1.5c)} \end{aligned}$$

that clarify the physical meaning of the scalar fields. ε and p represent the *total energy density* and the *pressure* (an isotropic pressure) in the fluid frame.

The perfect fluid stress-energy tensor is sometimes written as:

$$T_{\mu\nu} = \rho h u_\mu u_\nu + pg_{\mu\nu} \ . \tag{1.1.6}$$

Above the field ρ is the *rest-mass density* of the fluid and it is introduced with the *specific internal energy*, ϵ, in such a way to write the total energy density as (see also Eq. (1.3.1)):

$$\varepsilon = \rho(1 + \epsilon) \ . \tag{1.1.7}$$

In the case of a *simple fluid* (see Sec. 1.3), $\rho = m_B n$ where n is the *number density* in fluid rest frame (*number proper density*) and m_B the baryonic mass. The other scalar field in Eq. (1.1.6) is the *specific enthalpy*, $h \equiv 1 + \epsilon + p/\rho$.

1.2 Equations of relativistic hydrodynamics

The relativistic equations for the matter are the divergence of the stress-energy tensor:

$$\nabla^\mu T_{\mu\alpha} = g^{\mu\nu}\nabla_\nu T_{\mu\alpha} = 0 \ . \tag{1.2.1}$$

It emerges as a consequence of the Einstein equations, thanks to the Bianchi identities. Differently form the case of a flat (non-dynamical) spacetime, Eq. (1.2.1) expresses only a local conservation law [1] and no conserved quantities can be associated to integrals of $T_{\mu\nu}$ [2].

The equations describing relativistic hydrodynamics are a system composed by Eq. (1.2.1), the Equation of State (EOS) of the fluid (Sec. 1.3), and other field equations independent from the Einstein equations, *e.g.* the Maxwell equations and baryon number conservation. The equations of relativistic hydrodynamics must be solved coupled to the Einstein field equation for the metric tensor.

In the case of a perfect fluid Eq. (1.2.1) becomes

$$\left[u^\mu \nabla_\mu \left(\varepsilon + p\right) + \left(\varepsilon + p\right) \nabla_\mu u^\mu\right] u_\alpha + \left(\varepsilon + p\right) g_{\alpha\nu} u^\mu \nabla_\mu u^\nu + \nabla_\alpha p = 0 \ . \tag{1.2.2}$$

Considering the projection of Eq. (1.2.2) along $\mathbf{u}$ we get the scalar equation:

$$u^\mu \nabla_\mu \varepsilon = -\left(\varepsilon + p\right) \nabla_\mu u^\mu \ , \tag{1.2.3a}$$

while the projection orthogonal to $\mathbf{u}$ gives the 3 equations:

$$\left(\varepsilon + p\right) g_{\alpha\nu} u^\mu \nabla_\mu u^\nu = -\nabla_\alpha p - \left(u^\mu \nabla_\mu p\right) u_\alpha \tag{1.2.3b}$$

that represent the relativistic generalization of the Euler equations. Eq. (1.2.2) (or equivalently Eq. (1.2.3a) plus Eq. (1.2.3b)) are 4 equations for the 5 unknowns ε, p and u^μ (remember that $u^\mu u_\mu = -1$), so an EOS in the form $\bar{\varepsilon}(p)$ is in principle sufficient to close the system. However the EOS relates usually 3 thermo-dynamical quantities and a fundamental law must be still taken into account. It is the conservation of the baryon number:

$$\nabla_\mu J^\mu \equiv \nabla_\mu \left(n u^\mu\right) = 0 \ . \tag{1.2.4}$$

The presence of Eq. (1.2.4) explain why is sometimes preferable the definition of the stress-energy tensor as given in Eq. (1.1.6). In this case Eq. (1.2.2) and Eq. (1.2.4) plus the EOS (see *e.g.* Eq. (1.3.17)) are 6 equations for the 6 unknowns ρ (or n), ϵ, p and u^μ.

1.2.1 "3+1" conservative formulation

The accurate solution of the relativistic hydrodynamics equations to describe relativistic flows in an astrophysical scenario is a highly non-trivial problem.

---

[1] In the sense that they reduce to the conservation law

$$\partial_\mu T_{\mu\alpha} = 0$$

in a local inertial frame.

[2] The energy-momentum 4-vector of the matter is not conserved in a dynamical spacetime but is conserved the energy-momentum 4-vector of the matter and the metric. The stress-energy tensor does not take into account the energy of the gravitational field. In Minkowski spacetime conserved quantities like the energy-momentum 4-vector and the angular momentum, that can be expressed as integrals of $T_{\mu\nu}$, are preserved as a consequence of Poincaré invariance, which does not hold for a general metric tensor. In a similar way however, conserved quantities appear in GR in presence of a symmetry of the metric (Noether theorem), or considering the Landau-Lifshitz *stress-energy pseudo-tensor*, [122]. In the former case a Killing vector K^μ generates a conserved charge from the (covariantly) conserved current $J^\alpha \equiv T^{\alpha\mu} K_\mu$. In the latter case the "energy" of the gravitational field is described by a *pseudo* tensor (a tensor only under linear coordinate transformations) and, using both $T_{\mu\nu}$ and this pseudo-tensor, a conserved energy-momentum 4-vector can be defined.

Even in the case of the perfect fluid approximation without magnetic field, the solution are characterized by the presence of shock waves and high Lorentz factors and their correct representation required the development of sophisticated numerical algorithms [88]. The state of art of these algorithms is based on the Godunov method in classical fluid dynamics, *e.g.* [**?**, 110]. and exploit the hyperbolic and conservative character of the equations. Within the "3+1" formulation of the Einstein equations, the equations of relativistic fluid dynamics can be re-written in a first-order, manifestly hyperbolic and conservative form [133, 31, 110], suitable to the application of modern and accurate numerical schemes.

In the "3+1" formulation, *e.g.* [69], the spacetime is assumed to be globally hyperbolic (admits a Cauchy surface Σ), $\mathcal{M} = \mathbb{R} \times \Sigma$, so that it is foliated in spacelike hypersurfaces Σ_t, *i.e.* exist a smooth and regular [3] scalar field t such that each hypersurface is a level surface of t. The unit timelike 4-vector, normal to Σ_t, is $n^\mu \equiv -\alpha \nabla^\mu t$; the positive function α is called the *lapse* function. The induced 3-metric on Σ_t is $\gamma_{\mu\nu} \equiv g_{\mu\nu} + n_\mu n_\nu$ and the (spacelike) *shift vector* is $\beta \equiv \partial_t - \alpha \mathbf{n}$ ($\beta^\mu n_\mu = 0$). Using coordinates adapted to the foliation, see *e.g.* [98], the line element is:

$$g_{\mu\nu} dx^\mu dx^\nu = -(\alpha^2 - \beta^i \beta_i) dt^2 + 2\beta_i dx^i dt + \gamma_{ij} dx^i x^j \ . \tag{1.2.5}$$

A key role in the "3+1" conservative formulation of hydrodynamics equations is played by Eulerian observers $\mathcal{O}_E$, which are those observer whose 4-velocity is n^μ. They reduce to locally non-rotating or zero angular momentum (ZAMO) observers in the case of axisymmetric and stationary spacetimes, [32, 33]. The fluid velocity measured by $\mathcal{O}_E$ is, using Eq. (1.1.4) and identifying $\mathbf{U}$ with $\mathbf{v}$,

$$v^i = \frac{u^i}{W} + \frac{\beta^i}{\alpha} = \frac{1}{\alpha}\left(\frac{u^i}{u^0} + \beta^i\right) \ . \tag{1.2.6}$$

Above $W \equiv -u^\mu n_\mu = \alpha u^t$ is the Lorentz factor between the fluid frame and $\mathcal{O}_E$ which satisfies $W = 1/\sqrt{1 - v^2}$.

As shown by Ref. [31], in order to write system composed by Eq. (1.2.2) and Eq. (1.2.4) in the flux-conservative form, the 7 *primitive* hydro-dynamical variables ρ, p, v^i, ϵ and W are mapped to the so-called *conserved* variables via the relations

$$D \equiv W\rho \tag{1.2.7a}$$
$$S_i \equiv W^2 \rho h v_i \tag{1.2.7b}$$
$$\tau \equiv \left(W^2 \rho h - p\right) - D \ . \tag{1.2.7c}$$

The quantities D and S_i are nothing else than the rest-mass density and the momentum density (P_i of Eq. (1.1.3b)) measured by $\mathcal{O}_E$. The other quantity is $\tau = E - D$, again measured by the Eulerian observer. It is necessary to note that only 5 of the 7 primitive variables, the ones that form the vector $\vec{w} \equiv (\rho, v_i, \epsilon)$, are independent. The pressure in fact can be obtained using the EOS, while the Lorentz factor from the relation $W = 1/\sqrt{1 - v^2}$.

Once defined the vector

$$\vec{q} \equiv \sqrt{\gamma}(D, S_i, \tau) \tag{1.2.8}$$

---

[3] The gradient of t does not vanish, the hypersurfaces are non-intersecting.

where $\gamma \equiv \det \gamma_{ij}$, Eq. (1.2.2) and Eq. (1.2.4) can be written in a hyperbolic, first-order and flux-conservative form of the type

$$\partial_t \vec{q} + \partial_i \vec{f}^{(i)}(\vec{q}) = \vec{s}(\vec{q}) \ , \tag{1.2.9a}$$

where $\vec{f}^{(i)}(\vec{q})$ are the *flux vectors*:

$$\vec{f}^{(i)} \equiv \sqrt{-g}\left[D\left(v^i - \frac{\beta^i}{\alpha}\right), S_j\left(v^i - \frac{\beta^i}{\alpha}\right) + p\delta^i_j, \tau\left(v^i - \frac{\beta^i}{\alpha}\right) + pv^i\right] \tag{1.2.9b}$$

and $\vec{s}(\vec{q})$ are the *source terms*:

$$\vec{s} \equiv \sqrt{-g}\left[0, T^{\mu\nu}\left(\partial_\mu g_{\nu j} - \Gamma^\delta_{\nu\mu} g_{\delta j}\right), \alpha\left(T^{\mu 0}\partial_\mu \ln\alpha - T^{\mu\nu}\Gamma^0_{\nu\mu}\right)\right] \ . \tag{1.2.9c}$$

Above $g \equiv \det g_{\mu\nu} = -\alpha^2\gamma$.

While the system in Eq. (1.2.9) is not strictly hyperbolic, strong hyperbolicity is recovered in a flat space-time, where $\vec{s} = 0$. The the source terms do not depend on derivatives of the stress-energy tensor, a fundamental property to preserve numerically the hyperbolic character of the equations. We remind to Ref. [152] for a detail analysis of the properties of Eq. (**??**).

Note that source terms contain the $T^{\mu\nu}$, i.e. the primitive variables. They are also present in the RHS of the Einstein equations that must be solved coupled to Eq. (1.2.9). To find primitives variable it is necessary to invert Eq. (1.2.7). The inverse relations are:

$$v^i(p) = \frac{\bar{S}^i}{\bar{\tau} + \bar{D} + p} \tag{1.2.10a}$$

$$\rho(p) = \frac{\bar{D}}{W} \tag{1.2.10b}$$

$$\epsilon(p) = \frac{\bar{\tau} + \bar{D}\left(1 - W\right) + p\left(1 - W^2\right)}{\bar{D}W} \ , \tag{1.2.10c}$$

where $\bar{X} \equiv X/\sqrt{\gamma}$. The common procedure adopted for the inversion [134] is to solve numerically (with a nonlinear root-finder algorithm) an algebraic equation for the pressure (see Eq. (1.3.17)):

$$f(p) = \bar{p}\left(\rho(p), \epsilon(p)\right) - p \ , \tag{1.2.11}$$

and compute then the 3-velocity from the relation in Eq. (1.2.10a), the other primitive variables follows.

The conservative form of the hydrodynamics equations in Eq. (1.2.9a) presents important advantages when they are solved numerically. First, a theorem by Lax and Wendroff [125] guarantees that, if the numerical method converges [4] , it converges to the *weak solutions* that are generalized non-unique solutions of the integral form of the conservation law. These solutions take into account the discontinuities (*shock waves*) that emerge from the nonlinear character of the equations. Second, within the weak solutions, it is possible to select the the physical one, the *entropy-satisfying solution* [202, 128], *i.e.* the vanishing-viscosity-limit solution. Finally, a convergent numerical method in

---

[4] Convergence property is in general proved with some stability criteria, following the Lax's *equivalence theorem* (A numerical scheme is convergent if it is consistent and stable).

non-conservative form converges to the “wrong” solution in presence of a shock wave (Hou-LeFloch theorem, 1994).

A description of the numerical methods to solve the equations presented here can be found in [88] and in [134]. The generalization of these equations in the case of (ideal fluid) magneto-hydrodynamics is discussed in [19].

1.3 Equation of State for the fluid

The final section of this chapter is devoted to the concept of EOS, that describe the thermo-dynamical properties of the fluid from the assumption on its composition.

Assuming that the fluid is composed, at a microscopical level, by a certain number N particles species the total energy density can be written as the sum of two contributes: the rest-mass density and the internal energy

$$\begin{aligned} \varepsilon &= \varepsilon_0 + \varepsilon_{\text{int}} && (1.3.1) \\ &= \underbrace{\sum_{a=1}^{N} m_a n_a}_{\rho c^2} + \underbrace{\varepsilon_{\text{int}}}_{\rho c^2 \epsilon} \,. && (1.3.2) \end{aligned}$$

In Eq. (1.3.1) n_a is the *number proper density* of species a ($a = 1, 2, ..., N$) and m_a the mass, their relation with the fields ρ and ϵ is underlined (re-introducing the light speed for clarity). The internal energy is the contribute due to the (microscopic) kinetic and potential energy of the particles.

The Equation of State (EOS) is a function

$$\varepsilon = \bar{\varepsilon}(n_a, \epsilon) \tag{1.3.3}$$

that relates the total energy density with two other thermo-dynamical quantities: the number proper density and the specific internal energy. Changing the parameterization for the internal energy, it can also be expressed as:

$$\varepsilon = \bar{\varepsilon}(n_a, s) \tag{1.3.4}$$

where s is the *entropy density.*

The first law of thermodynamics applied to the fluid in a volume $\mathcal{V}$ (that can vary) reads:

$$d\mathcal{E} = Td\mathcal{S} - pd\mathcal{V} + \sum_a \mu_a d\mathcal{N}_a \tag{1.3.5}$$

where

$$\begin{aligned} T &\equiv \left(\frac{\partial \mathcal{E}}{\partial \mathcal{S}}\right)_{\mathcal{N},\mathcal{V}} && (1.3.6) \\ \mu_a &\equiv \left(\frac{\partial \mathcal{E}}{\partial \mathcal{N}_a}\right)_{\mathcal{S},\mathcal{V},\mathcal{N}_{b\neq a}} && (1.3.7) \end{aligned}$$

are the temperature and the relativistic [5] chemical potentials. In Eq. (1.3.5) $\mathcal{S} \equiv s\mathcal{V}$ is total entropy in $\mathcal{V}$, $\mathcal{E} \equiv \varepsilon\mathcal{V}$ is the total energy in $\mathcal{V}$, $\mathcal{N}_a \equiv n_a\mathcal{V}$ is

---

[5] The difference with the non-relativistic chemical potential is the mass: $\mu_a = \mu_a^{\text{non-rel}} + m_a$.

number of particles of species a in $\mathcal{V}$. The *speed of sound* is defined as

$$C_s \equiv \sqrt{\frac{\partial p}{\partial \varepsilon}} \; . \tag{1.3.8}$$

An important quantities related to C_s is the *adiabatic exponent*

$$\Gamma \equiv C_s^2 \left(\frac{\varepsilon}{p} + 1 \right) \; . \tag{1.3.9}$$

It is a dimensionless quantity measuring the stiffness of the EOS: a larger Γ means a larger increase of pressure for a given increase in energy density, *i.e.* a stiffer EOS. A degenerate Fermi gas, for example, is characterized by $\Gamma = 5/3$ in the non-relativistic case, and $\Gamma = 4/3$ in the relativistic case. Neutron stars can be modeled by a polytropic EOS Eq. (1.3.25) with $\Gamma = 2$, but for more "realistic" EOS Γ is a function of the energy density (see Chap. 2).

The expression of the *free energy* or *Gibbs free energy* per unit of volume

$$\begin{aligned} G &= \varepsilon + p - Ts && (1.3.10) \\ &= \sum_a \mu_a n_a \; , && (1.3.11) \end{aligned}$$

leads to the identity:

$$p = Ts - \varepsilon + \sum_a \mu_a n_a \; , \tag{1.3.12}$$

that states that the pressure is fully determined by the EOS as a function of n_a and s. Eq. (1.3.12) can be also derived using the first law of thermodynamics and permits to express also the EOS in term of the pressure: $p = \bar{p}(n_a, \epsilon)$.

Using the first law of thermodynamics Eq. (1.3.5) (in a fixed volume), it is straightforward to show that Eq. (1.2.3a) reduces, using the identity Eq. (1.3.12) to:

$$T\nabla_\mu \left(s u^\mu \right) + \sum_a \mu^a \nabla_\mu \left(n_a u^\mu \right) = 0 \; . \tag{1.3.13}$$

In words we can say that, in the case of perfect fluid matter, the only process that can increase the entropy is the creation of particles, [97].

The *simple fluid* is a fluid described by an EOS in the form

$$\varepsilon = \bar{\varepsilon}(n, s) \; , \tag{1.3.14}$$

where n is the baryon (or total) number density. The simple fluid EOS can be used in all the cases when the particle number densities can be obtained from the relation: $n_a = Y_a n$, where Y_a can be a function of (s, n), and it behaves as if it contains a single particle species ($N = 1$). Eq. (1.3.13) and the baryon number conservation (Eq. (1.2.4)) imply immediately that, in the case of a simple fluid,

$$\nabla_\mu \left(s u^\mu \right) = 0 \; , \tag{1.3.15}$$

i.e. the evolution is adiabatic. Moreover it can be showed that the *entropy per baryon* $\tilde{s} = s/n$ is conserved along fluid lines. Eq. (1.3.12) reduce to $p = Ts - \varepsilon + \mu n$, from which it is possible to define the *enthalpy per baryon*:

$$\tilde{h} \equiv \frac{\varepsilon + p}{n} = \mu + Ts = \frac{h}{m_B} \; . \tag{1.3.16}$$

Another form of the simple fluid EOS is:

$$p = \bar{p}(n, \epsilon) \tag{1.3.17}$$

that must be used with the definition of the total energy density $\varepsilon \equiv m_B n(1+\epsilon)$.

A particular case of simple fluid is the *barotropic fluid*:

$$\varepsilon = \bar{\varepsilon}(n) \ . \tag{1.3.18}$$

An isentropic fluid, for which $\tilde{s} = \text{const}$, is described by a barotropic EOS. The EOS for a barotropic fluid is also written as:

$$p = \bar{p}(n) \tag{1.3.19a}$$
$$\epsilon = \bar{\epsilon}(n) \tag{1.3.19b}$$

with $\varepsilon \equiv m_B n(1+\epsilon)$, or directly

$$p = \bar{p}(n) \tag{1.3.20a}$$
$$\varepsilon = \bar{\varepsilon}(n) \ . \tag{1.3.20b}$$

The EOS must be prescribed in such a way Eq. (1.3.12) (or Eq. (1.3.21), see below) holds. Eq. (1.3.20) is 1-parameter EOS and it is applied in the description of the cold dense matter of neutron stars, see Chap. 2. For a barotropic fluid the 5 hydrodynamics equations in Eq. (1.2.2) and Eq. (1.2.4) reduce to 4, and in particular Eq. (1.2.3a) is equivalent to Eq. (1.2.4). In fact, using Eq. (1.3.20), Eq. (1.3.12) can be written as:

$$p(n) = -\varepsilon + n\frac{d\varepsilon}{dn} = n^2 \frac{d}{dn}\left(\frac{\varepsilon}{n}\right) \ , \tag{1.3.21}$$

and Eq. (1.2.3a) becomes

$$\begin{aligned} 0 &= u^\mu \nabla_\mu \varepsilon + (\varepsilon + p)\nabla_\mu u^\mu = && (1.3.22a)\\ &= u^\mu \nabla_\mu \varepsilon - u^\mu \frac{(\varepsilon+p)}{n}\nabla_\mu n + \frac{(\varepsilon+p)}{n}\nabla_\mu\left(n u^\mu\right) = && (1.3.22b)\\ &= u^\mu\left[\frac{d\varepsilon}{dn} - \frac{(\varepsilon+p)}{n}\right]\nabla_\mu n + \frac{(\varepsilon+p)}{n}\nabla_\mu\left(n u^\mu\right) = && (1.3.22c)\\ &= \frac{(\varepsilon+p)}{n}\nabla_\mu\left(n u^\mu\right) \ . && (1.3.22d) \end{aligned}$$

Finally there is an important relation involving the enthalpy per baryon that holds for a barotropic fluid. Using the first law of thermodynamics principle and the definition of the enthalpy per baryon given above, is simple to show that

$$\frac{dp}{\varepsilon + p} = d\ln\tilde{h} \equiv dH \ , \tag{1.3.23}$$

which also defines the *heat function* H.

1.3.1 Analytic EOS

An EOS widely used in numerical relativity is the *ideal fluid* EOS:

$$\bar{p}(n,\epsilon) = (\Gamma-1)m_B n\epsilon \tag{1.3.24}$$

Above Γ is a parameter to be fixed. This is a simple fluid EOS of the type Eq. (1.3.17) that allows transfer of kinetic energy to thermal energy and, thus, shock heating.

The *polytropic* EOS is a barotropic fluid EOS in the form of Eq. (1.3.20):

$$\begin{aligned} \bar{p}(n) &= Kn^\Gamma && (1.3.25a) \\ \bar{\varepsilon}(n) &= m_B n + K\frac{n^\Gamma}{\Gamma-1} && (1.3.25b) \end{aligned}$$

where K and Γ are parameters to be fixed [201]. The latter in particular coincides with the adiabatic exponent. Note that (substituting the first equation into the second) Eq. (1.3.25) is consistent with ideal fluid EOS. For this reason it is often used in the computation of the equilibrium models (it amounts only in fixing the entropy to a certain value) that can successively evoluted both with the polytropic or the ideal EOS.

For the polytropic EOS it is easy to show that

$$H(n) = \ln\left(1+\frac{K}{m_B}\frac{\Gamma}{\Gamma-1}n^{\Gamma-1}\right) \ , \tag{1.3.26}$$

and, inverting this formula, one obtains also:

$$n(H) = \left[\frac{\Gamma-1}{\Gamma}\frac{m_B}{K}(\exp(H)-1)\right]^{1/(\Gamma-1)} \ . \tag{1.3.27}$$

These relations involving the heat function reads are particularly useful in the computation of equilibrium models of rotating NS, see Sec. 2.4.2.

Finally we notice that Eq. (1.3.25) is different from

$$\bar{p}(\varepsilon) = K\varepsilon^\Gamma \tag{1.3.28}$$

described in Ref. [200], for which Γ reduces to the adiabatic exponent only in the Newtonian limit.

1.3.2 "Realistic" EOS

The term *realistic* EOS usually refers to a variety of models that describe the cold dense matter of a NS or, more in general, also matter models with temperature-dependent components. Realistic EOS take into account various chemical and physical aspects of the composition of the fluid: molecular interactions, relativistic effects, quantization and nuclear physics. They are usually calculated a priori from many body theories and supplied as tables for their use in hydrodynamics codes [191]. In Chap. 2 some realistic EOS for neutron star, and how to use them, are described.

Chapter 2

Neutron star models

The equilibrium configuration of a NS must be computed solving the Einstein field equations as well as the equations for hydro-stationary equilibrium. The equilibrium properties of a relativistic star depend on the strong interactions governing the high nuclear matter in the interior. This kind of information is contained in the EOS and represent the most intriguing aspect of NSs, being largely unknown. Observational constraints, mainly based on astrophysical data, are the only way to infer about the NS EOS. The principal astrophysical sources are pulsar object, tough to be rapidly rotating highly magnetized neutron stars and emitting electromagnetic radiation from the radio to the X-ray band, and observation of neutrinos from proto-neutron star, but also heavy-ion collisions laboratory experiment can give information on dense matter EOS. A detailed discussion and many references can be found in [123, 131, 187], to introduce this chapter we give here only some general ideas. For example pulsar glitches permits to estimate that the departures from a perfect fluid matter, due to the presence of a crust, are of the order 10^{-5}. A NS is generally assumed to have zero-temperature since is thermal energy ($\ll 1$ MeV) is smaller than the Fermi energy of the interior (> 60 MeV). As a consequence perfect fluid matter with a barotropic EOS is usually employed in the description. Binary and millisecond pulsars data constraints the observed NS to have a rotational period $P < 1.56$ ms and a non-rotating limit configuration with gravitational mass $M = 1.44\ M_\odot$. The limiting radius is in this case around $R = 14.3$ km. The compactness can be estimated from the observation of Low-Mass X-ray Binary (LMXB) and it is of the order of $M/R = 0.23$. Finally, NS are expected to be rotating differentially at birth but shear viscosity, convective and turbulent motion and magnetic breaking are all phenomena that can lead to uniform rotation on time-scales ranging from few years to minutes.

2.1 Neutron star matter

Neutron stars are composed by high density baryonic matter. The exact nature of the internal structure, determined essential by strong interactions, is unknown. To model the NS interior (approximated) many-body theories with effective Hamiltonians are usually employed. The principal assumptions are that the matter is strongly degenerate and that it is at the thermodynamics

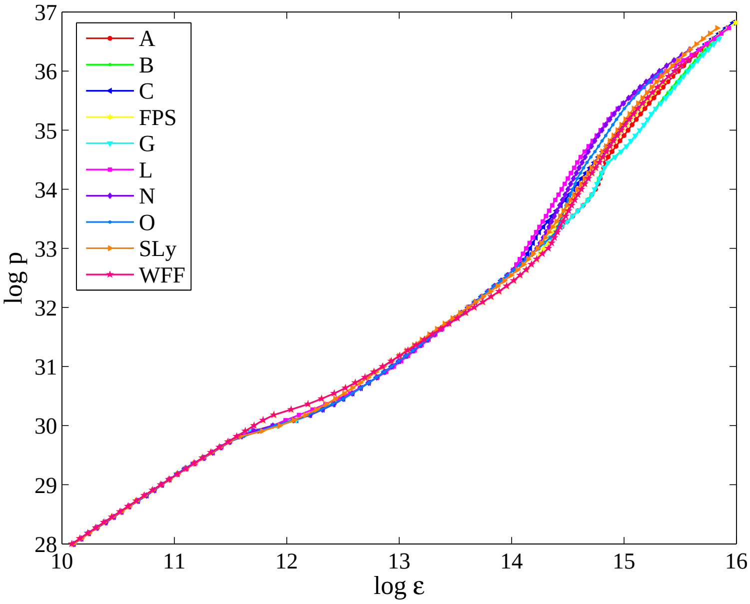

Figure 2.1: Equation of State sample. Pressure as a function of the total energy density. The EOS used are listed in Tab. 2.1. Notice here we are using cgs units.

equilibrium. Consequently, temperature effects can be neglected and the matter is in its ground state. Under the above conditions we speak of *cold catalyzed matter*, and the EOS has one-parameter character: $p = \bar{p}(n)$ and $\varepsilon = \bar{\varepsilon}(n)$, see Eq. (1.3.20).

The composition of a NS consists qualitatively of three parts separated by transition points, see Fig. 2.1. At densities below the *neutron drip*, $\varepsilon < \varepsilon_{\rm d} \sim 10^{11}$ $\rm g\,cm^{-3}$ (the *outer crust*) the nuclei are immersed in an electron gas and the electron pressure is the principal contribute to the EOS. In the *inner crust*, $\varepsilon_{\rm d} < \varepsilon < 10^{14}$ $\rm g\,cm^{-3}$, the gas is also composed of a fraction of neutrons unbounded from the nuclei and the EOS softens due to the attractive long-range behavior of the strong interactions. For $\varepsilon > 10^{14}$ $\rm g\,cm^{-3}$ a homogeneous plasma of nucleons, electrons, muons and other baryonic matter (*e.g.* mesons, hyperons), composes the *core* of the star. In this region the EOS stiffens because of the repulsive short-range character of the strong interactions.

Fig. 2.2 shows the adiabatic exponent which, under the assumption of thermodynamics equilibrium, determines the response of pressure to a local perturbation of density. We mention that, as explained in detail in Ref. [81], in a pulsating NS the “actual adiabatic exponent” can be higher than that obtained from the EOS because the time-scale of the beta processes are longer than the dynamical time-scales of the pulsations. Thus the fraction of particles in a perturbed fluid element is assumed fixed to the unperturbed values (frozen composition). We refer the reader to [105] for all the details on neutron star structure and the complex physics behind it (*e.g.* elasticity of the crust, possible super-fluid interior core, magnetic fields).

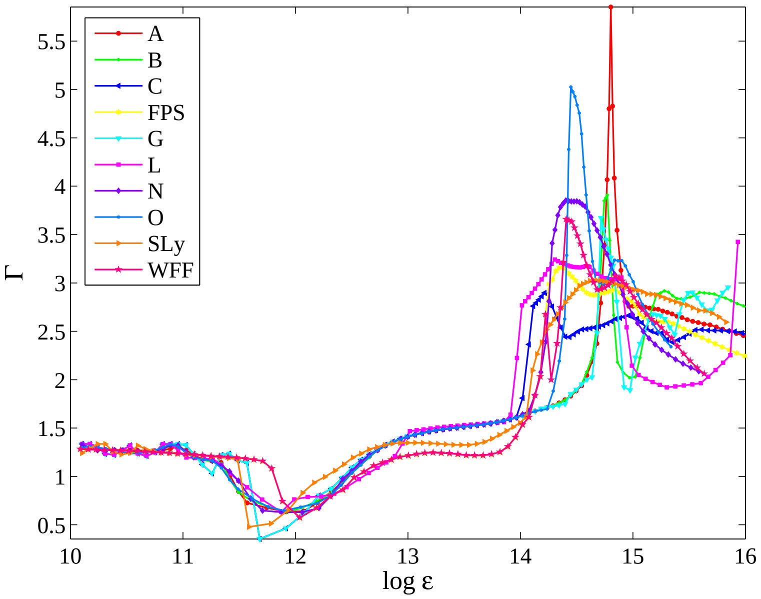

Figure 2.2: Equation of State sample. Adiabatic exponent as a function of the total energy density. The EOS used are listed in Tab. 2.1. Notice here we are using cgs units.

To compensate the ignorance on the interior part of the star it is common to consider in numerical relativity simulations a large set of EOS derived from different models. In Fig. 2.1 we consider a sample of 10 EOS that exhibit all the same qualitative features describe above, but that differ significantly for what concern the description of the core and the NS models produced (see Sec. 2.4.1). Seven EOS of the sample were already used in [20], and in many other works (see for example Refs. [129, 14, 42, 113, 41] on pulsations of relativistic stars, and [171, 189, 148] on equilibrium models of rotating stars). Maintaining the same notation of [20], they are called A, B, C, G, L, N and O EOS. Most of the models in the sample are based on non-relativistic interactions modeled with Reid soft core type potentials. EOS N [207] and O [56, 55] are instead based on relativistic interaction and many-body theories. Model G [63] is an extremely soft EOS, while L [20] is extremely stiff. EOS A [150] and C [47] are of intermediate stiffness. In addition, the sample include the FPS EOS [91, 130], and the SLy EOS [81], modeled by Skyrme effective interactions. The FPS EOS, in particular is a modern version of Friedman and Pandharipande EOS [91]. The FPS and SLy EOSs are an example of *unified* EOS, that means that they are obtained by a many-body calculation from a single effective nuclear Hamiltonian valid in all the NS interior. The last EOS considered is the UV14+TNI (here renamed WFF) EOS of [209], which is an intermediate stiffness EOS based on two-body Urbana UV14 potential with the phenomenological three-nucleon TNI interaction. The composition is assumed to be of neutrons. For all the EOS models the inner crust is described by the BBS [39] or the HP94 [103] EOS,

Table 2.1: A list of EOS with references.

Name	Authors	References
A	Pandharipande	[150]
B	Pandharipande	[151]
C	Bethe and Johnson	[47]
FPS	Lorenz, Ravenhall and Pethick	[91, 130]
G	Canuto and Chitre	[63]
L	Pandharipande and Smith	[20]
N	Walecka and Serot	[207]
O	Bowers, Gleeson and Pedigo	[56, 55]
SLy	Douchin and Haensel	[81]
WFF	Wiringa, Fiks and Farbroncini	[209]

while for outer crust the BPS EOS [40] is used. We refer to Tab. 2.1 and cited references for further details. A most modern EOS widely used in numerical relativity is the APR [3] EOS.

2.2 EOS Tables

Realistic EOS are usually given through tables. To use them in a numerical context it is necessary to interpolate between the tabulated values. The interpolation scheme can not be chosen arbitrarily but must properly take into account the first law of thermodynamics, see *e.g.* [106], that, in the case of a zero temperature EOS, is contained in Eq. (1.3.21):

$$p(n) = n^2 \frac{d}{dn}\left(\frac{\varepsilon}{n}\right) \ . \tag{2.2.1}$$

A thermodynamically consistent procedure was introduced in Ref. [191] and it is based on Hermite polynomials. Essentially the method permits to interpolate a function forcing the match on the tabulated points both of the function and of its derivatives. The use of 3rd order (cubic) Hermite polynomials, as done in Ref. [148], permits to impose Eq. (2.2.1).

Consider a function $y(x)$, given the tables of y_j and y'_j and a point $x_{\rm j} < x < x_{\rm j+1}$ the interpolated value $y(x)$ is:

$$\begin{aligned} y(x) \quad &= \quad y_i H_0(w) + y_{i+1} H_0(1-w) + \qquad (2.2.2)\\ &\quad + \left(\frac{dy}{dx}\right)_j \Delta x_j H_1(w) + \left(\frac{dy}{dx}\right)_{j+1} \Delta x_j H_1(1-w) \end{aligned}$$

where

$$\Delta x_j \equiv (x_{j+1} - x_j) \tag{2.2.3}$$

$$w(x) \equiv \frac{x - x_j}{\Delta x_j} \tag{2.2.4}$$

and

$$H_0(w) = 2w^3 - 3w^2 + 1 \tag{2.2.5}$$
$$H_1(w) = w^3 - 2w^2 + w \tag{2.2.6}$$

are the cubic Hermite functions. The principal properties of this method are that for $x \to x_j$

$$y(x) \to y_j \tag{2.2.7}$$
$$y'(x) \to y'_j \; . \tag{2.2.8}$$

The EOS tables are usually given as 3 column tables with the values for n, ε and p. If, for example, one needs to compute $\bar{\varepsilon}(p)$ and the speed of sound C_s^2, the thermodynamics consistency can be achieved by computing, for a given value of p, first $\bar{n}(p)$ and then $\bar{\varepsilon}(n)$ imposing the derivative through Eq. (2.2.1). Then the speed of sound is computed consistently with the interpolation. To obtain more accurate numerical data, it is possible to perform such calculations not directly on the functions but taking logarithms.

In the PerBaCCo (see Sec. 3.3) this kind of routines are implemented to use EOS from tables. Violation of the first law of thermodynamics are typically less than 0.1%. By contrast the use of other interpolation schemes, *i.e.* linear or spline interpolation, gives violation of the thermodynamic principle of some percents [1]. The implementation has been checked using the analytic EOS of Eq. (1.3.25) against the same but tabulated with tables of different numbers of entries. The results perfectly agree and with any dependence on the tabulated points. In the case of some (specific) tables (EOS FPS, SLy4 and L), we found that "high-order" interpolation (cubic Hermite and spline) did not permit an accurate reconstruction of the sound speed. This is due to spurious oscillations introduced by the high order derivatives. In all these cases the problem can be cured simply adopting a linear interpolation.

2.3 EOS analytic representation

An alternative method to the use of the tabulated EOS is the analytic representation method. It is been introduced quite recently by Haensel and Potekhin [104] and implemented in a 3D full GR code by Shibata et al [183] to simulate the merge of two NSs.

The main idea behind this method is to represent the EOS with analytic functions which relate the logarithms of the pressure, the energy density, *etc.* , and which depend on a number of parameters fixed by a fit with the tables. Basically the different parts of the EOS are fitted by means of a fractional-polynomials of low order and matched together by the "Fermi functions"

$$f(x) = \frac{1}{1+e^x} \tag{2.3.1}$$

---

[1] However we point out that in the specific case of the PerBaCCo the use of other interpolation schemes did not produce significant differences in the final result of the computation, *i.e.* the gravitational wave signal. This happens because the global numerical errors of the code are dominant over the errors related to the violation of the thermodynamics principle. See [43].

that serves as "smooth theta" functions. The differences with the tables are of the order of 2%, [104].

Analytic fits have the important property that derivatives of quantities can be calculated analytically and easily implemented. In this way it is possible to avoid the problems related to different choices of the interpolation. Moreover, analytic fits can be used in such a way to respect the thermodynamics relations. A possible drawback could be the computational cost (especially in 3D evolution code) required for the exponential and logarithms functions [76].

2.4 Equilibrium star models

The equilibrium configurations of relativistic stars have been widely studied in the literature, both in the case of non-rotating and of rotating star, see *e.g.* [69, 175, 187].

In the former case the spacetime is asymptotically flat, spherically symmetric and static, so it reduces to Schwarzschild solution in the exterior. Equilibrium sequences are parameterized by one parameter, *e.g.* the central energy density, and there is only one family of stable equilibrium configuration, solution of Eq. (2.4.2) (see below), that describes NS models. An upper limit on the maximum mass of non-rotating NS can be estimated in the range $4 - 6.7\ M_\odot$ depending on the assumptions on the EOS [109].

In the latter case the spacetime is stationary, axisymmetric and asymptotically flat, equilibrium sequences are parameterized by two quantity, *e.g.* the central energy density and one to control the rotation rate (plus eventually the parameters for the rotation law model). Typically, with respect to a non-rotating star of the same central density, the equatorial radius is 15-20% greater and the maximum mass increases of about 30-40% supported by the centrifugal force. However these properties depends strongly on the EOS and the rotation law that are assumed in the computation of the star model. There are for example interesting solutions, such as supra-massive sequences [72] (that spin up even if they lose angular momentum), highly flattered configurations [17], or "quasi-toroidal" stars (supported by the differential rotation and that can be the unstable to bar-mode deformation [23]), that significantly differ from the spherical stars. The maximum angular velocity allowed is determined by the *mass-shedding limit*, *i.e.* when the angular velocity of the star reaches the angular velocity of a particle in a circular Keplerian orbit at the equator.

In what follow we review only the basics equations and present the computation of some equilibrium sequences of non-rotating stars described by different EOS. We assume always perfect fluid stress-energy tensor in the form of Eq. (1.1.6).

2.4.1 Non-rotating stars

The spacetime of a spherical symmetric star is given, in spherical (Schwarzschild) coordinates, by:

$$g_{\mu\nu}dx^\mu dx^\nu = -e^{2\alpha}dt^2 + e^{2\beta}dr^2 + r^2(d\theta^2 + \sin^2\theta d\phi^2) \tag{2.4.1}$$

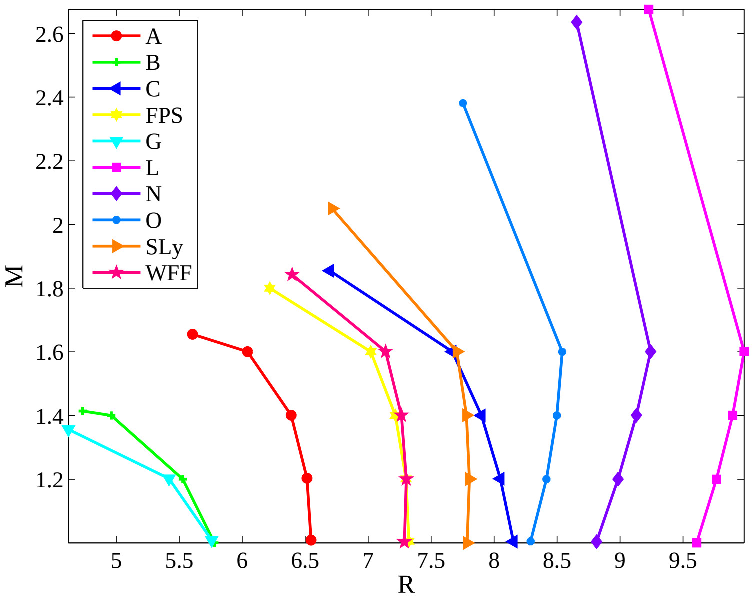

Figure 2.3: Non-rotating NS models. Mass-radius diagram for the NS models of Tab. 2.3.

where α and β are function of r only. The equilibrium configuration is the solution of the Tolmann-Oppenheimer-Volkoff (TOV) equations [197, 149]:

$$\begin{aligned} m_{,r} &= 4\pi r^2\varepsilon && \text{(2.4.2a)} \\ p_{,r} &= -(\varepsilon+p)\alpha_{,r} && \text{(2.4.2b)} \\ \alpha_{,r} &= \frac{1}{2}\frac{(m+4\pi r^3 p)}{(r^2-2mr)} \ , && \text{(2.4.2c)} \end{aligned}$$

with the boundary conditions:

$$\begin{aligned} m(0) &= 0 && \text{(2.4.3a)} \\ p(R) &= 0 && \text{(2.4.3b)} \\ \alpha(R) &= \ln\left(1-\frac{2M}{R}\right) \ . && \text{(2.4.3c)} \end{aligned}$$

Above $m(r)$ is the mass function defined as $e^{-2\beta(r)} = 1-2m(r)/r$ and represents the mass of the star inside a sphere of radius r. The system must be closed with an EOS. Eq. (2.4.3b) formally defines the star radius, R. Eq. (2.4.2) define the structure of the fluid and its spacetime in the interior, *i.e.* $r < R$, the exterior solution is matched with the Schwarzschild solution, Eq. (2.4.3c).

Sometimes isotropic coordinates are preferred than the Schwarzschild's ones. The line element for a spherical spacetime in isotropic coordinates reads

$$g_{\mu\nu}dx^\mu dx^\nu = -e^{2a}dt^2 + e^{2b}\left[d\bar{r}^2 + \bar{r}^2(d\theta^2 + \sin^2\theta d\phi^2)\right] \qquad (2.4.4)$$

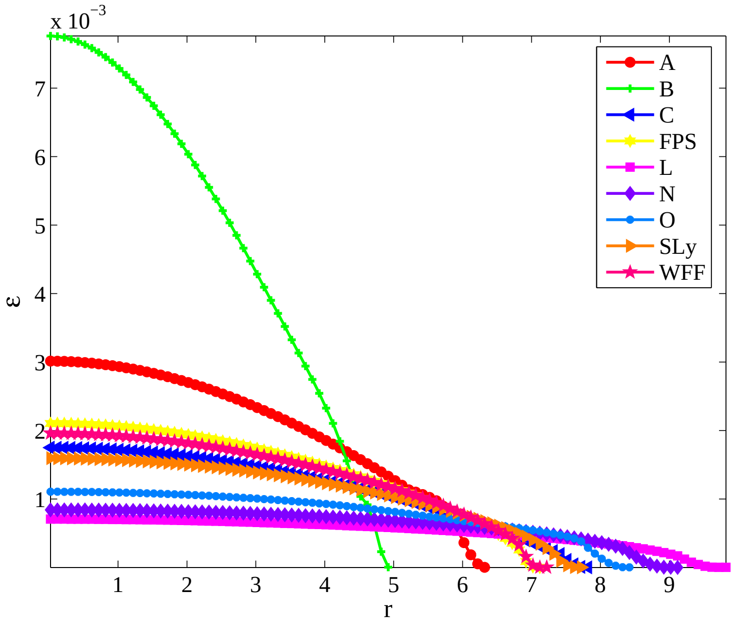

Figure 2.4: Non-rotating NS models. Radial profile of the total energy density, ε, for all models of Tab. 2.3 with $M = 1.4$.

where a, b are functions of the isotropic radius $\bar{r}$. The relations between the Schwarzschild and isotropic radial coordinates in the exterior are given by

$$r = \bar{r}\left(1+\frac{M}{2\bar{r}}\right)^2 \tag{2.4.5a}$$

$$\bar{r} = \frac{1}{2}\left(\sqrt{r^2-2Mr}+r-M\right) \tag{2.4.5b}$$

and in the interior by

$$r = \bar{r}e^{2b(\bar{r})} \tag{2.4.5c}$$

$$\bar{r} = \frac{I(R)}{2R}\left(\sqrt{R^2-2MR}+R-M\right)rI(r) \tag{2.4.5d}$$

where

$$I(r) \equiv \exp\left[-\int_0^r dx \frac{1-\sqrt{1-2m(x)/x}}{x\sqrt{1-2m(x)/x}}\right]. \tag{2.4.5e}$$

For each EOS of Tab. 2.1 the principal equilibrium properties of a representative set of NS models with $M = 1$, 1.2, 1.4, 1.6 and a model whose mass is close to the maximum mass allowed, for a total of 47 different neutron stars, are listed inTab. 2.3.

The mass-radius diagram is showed in Fig. 2.3 for all the models. The order of stiffness of the EOS can be estimated, on average, as: G $<$ B $<$ A $<$ FPS $<$ WFF $<$ SLy $<$ C $<$ O $<$ N $<$ L. For all the models described by a particular

EOS, the compactness M/R increases from about 0.1 to 0.3, corresponding to the increase of the star mass and the decrease of the radius. The maximum mass is $M = 1.36$ for the softer EOS (EOS G), while it is $M = 2.68$ for the stiffer (EOS L). The total energy density profile as a function of the radial coordinate is showed in Fig. 2.4 and explains that most of the mass is due to matter with density comparable to the central (maximum) density of the star. So the maximum mass of the star is essentially determined by the EOS of the core. On the other hand, the star radius depends on the properties of the matter at lower densities due to Eq. (2.4.3b). In the model computed it spans a range from $R \sim 5$ (in the case of EOS B and G) to $R \sim 9-10$ (for EOS L and N).

2.4.2 Rotating stars

In a stationary, axisymmetric, asymptotically flat spacetime and in absence of meridional convective currents [2], the metric can be expressed as [53]

$$\begin{aligned} g_{\mu\nu}dx^\mu dx^\nu &= -e^{2\nu}dt^2 + g_{\phi\phi}\left(d\phi - \omega dt\right)^2 + \\ &+ g_{11}(dx^1)^2 + 2g_{12}dx^1dx^2 + g_{22}(dx^2)^2 \end{aligned} \tag{2.4.6}$$

where t and ϕ are coordinates adapted to the symmetries, *i.e.* the killing vectors are $\partial/\partial t$ and $\partial/\partial\phi$. The other two coordinates are usually chosen of cylindrical type, $(x^1, x^2) = (\rho, \zeta)$, or spherical type, $(x^1, x^2) = (r, \theta)$, and *quasi-isotropic*: $g_{\rho\zeta} = 0$ and $g_{\zeta\zeta} = g_{\rho\rho}$ or $g_{r\theta} = 0$ and $g_{\theta\theta} = r^2 g_{rr}$. The functions ν, ω, g_{11}, g_{12} and g_{22} depend only on (x^1, x^2).

The Einstein equations reduces to a set of 4 elliptic equations for the metric coefficients and form a well posed boundary values problem. The equations of motion for the matter admit, in the case of perfect fluid matter, a first integral of the motion which involves the heat function defined in Eq. (1.3.23):

$$H + \nu + \int_{\Omega_c}^{\Omega} F(\Omega)d\Omega = \text{const} . \tag{2.4.7}$$

Above $\Omega \equiv u^\phi/u^t$ is the coordinate angular velocity of the matter (the fluid 4-velocity is $\mathbf{u} = (u^t, 0, 0, u^\phi)$) and $F \equiv u_\phi u^t$ is a function of Ω to be prescribed: the rotation law. Eq. (2.4.7) and the EOS close the system. The numerical solution of these equations have been computed by many authors [57, 58, 92, 117, 118, 53, 71, 73, 171, 172, 189, 38, 18]. Ref. [51] presents the first calculation of rotating stars with magnetic field.

The asymptotic expressions of the solutions for $r \to \infty$:

$$\nu \sim -\frac{M}{r} \tag{2.4.8}$$

$$\omega \sim \frac{2J}{r} , \tag{2.4.9}$$

---

[2] If t^μ is timelike the Killing vector (at spatial infinity) and ϕ^μ the spacelike axial Killing vector (remember that the asymptotic flatness gives $t^\mu t_\mu = -1$, $\phi^\mu\phi_\mu = +\infty$ and $t^\mu\phi_\mu = 0$), the stress-energy tensor must satisfy:

$$T^\alpha_\mu t^\mu = c_1 t^\alpha + c_2\phi^\alpha$$

$$T^\alpha_\mu \phi^\mu = c_3 t^\alpha + c_4\phi^\alpha$$

where the c's are numbers.

Table 2.2: Equilibrium properties of the the sequence AU. The sequence is composed by uniformly rotating NS models described by the polytropic EOS $\bar{p}(\rho) = K\rho^{\Gamma}$ with $K = 100$ and $\Gamma = 2$. From up to down the rows report: central mass density, central energy density, gravitational mass, rest-mass, circumferential radius, angular momentum, ratio $\beta \equiv T/|W|$ between rotational kinetic and gravitational binding energy, angular velocity, ratio between coordinate polar and equatorial radii and Kerr parameter. This sequence has been introduced in Refs. [89, 79].

Model		AU0	AU1	AU2	AU3	AU4	AU5
ρ_c	$(\times 10^{-3})$	1.28	1.164	1.072	0.978	0.883	0.799
ε_c	$(\times 10^{-3})$	1.44	1.30	1.187	1.074	0.961	0.863
M		1.399	1.404	1.408	1.411	1.415	1.420
M_0		1.506	1.506	1.506	1.506	1.506	1.506
R		9.58	10.19	10.79	11.55	12.64	14.93
J	$(\times 10^{-1})$	0	5.687	7.974	10.09	12.25	14.32
β	$(\times 10^{-2})$	0	1.952	3.645	5.502	7.548	9.544
Ω	$(\times 10^{-2})$	0	1.293	1.655	1.888	2.029	2.085
Ω_K	$(\times 10^{-2})$	3.987	3.635	3.359	3.055	2.694	2.105
r_p/r_e	$(\times 10^{-1})$	10	9.194	8.522	7.780	6.980	5.750
J/M^2	$(\times 10^{-1})$	0	2.884	4.025	5.068	6.113	7.099

define the global quantities such as the total gravitational mass M and the total angular momentum, J. In addition there is the circumferential radius R defined as the radius measured by the Eulerian observes.

The exterior in general can not be matched with the Kerr solution, even if the latter is a vacuum solution that posses the same symmetries. The multipoles in general differs from the Kerr [121, 54] (see also [35] in the case of a thin disk in uniform rotation).

As an example we show in Fig. 2.2 a sequence of uniformly rotating NSs with fixed rest mass of $M_0 = 1.506\ M_{\odot}$, see also Refs. [89, 79]. The sequence has a non-rotating member and ends at the Keplerian limit $\Omega = \Omega_K$. The EOS is the polytropic one with $K = 100$ and $\Gamma = 2$, and some equilibrium properties are listed in Tab. 2.2. For example from the table one can note how, as the central density and the ratio between polar and equatorial radii decreases, the mass and the angular velocity increase.

Since this thesis mainly deals with non-rotating stars we refer the reader to [187] for a review on equilibrium properties of rotating stars.

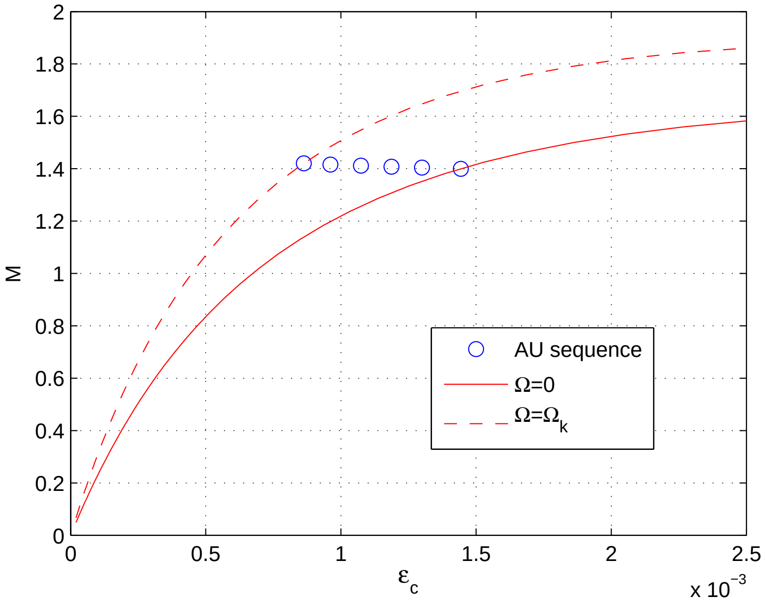

Figure 2.5: Rotating NS models. The masses of a sequence of non-rotating NSs and a sequence of uniformly rotating NSs at the mass-shedding limit are showed for a range of central energy densities. Between them some models of the sequence AU of uniformly rotating NS of fixed rest-mass $M_0 = 1.506\ M_\odot$ are plotted. Equilibrium properties are listed in Tab. 2.2.

Table 2.3: Non-rotating NS models. From left to right the columns report: the name of the model, the EOS type, the mass M, the radius R, the compactness M/R, the central energy density $\varepsilon_{\rm c}$ and the central pressure p_c.

Model	EOS	M	R	M/R	$\varepsilon_{\rm c}$	$p_{\rm c}$
A10	A	1.00	6.55	0.15	1.96×10^{-3}	2.35×10^{-4}
A12	A	1.20	6.51	0.18	2.38×10^{-3}	3.76×10^{-4}
A14	A	1.40	6.39	0.22	3.01×10^{-3}	6.50×10^{-4}
A16	A	1.60	6.04	0.26	4.46×10^{-3}	1.49×10^{-3}
Amx	A	1.65	5.60	0.29	6.78×10^{-3}	3.24×10^{-3}
B10	B	1.00	5.78	0.17	1.37×10^{-3}	5.13×10^{-4}
B12	B	1.20	5.53	0.22	1.59×10^{-3}	1.02×10^{-3}
B14	B	1.40	4.96	0.28	1.88×10^{-3}	3.42×10^{-3}
Bmx	B	1.41	4.73	0.30	4.65×10^{-3}	5.33×10^{-3}
C10	C	1.00	8.15	0.12	3.35×10^{-3}	1.05×10^{-4}
C12	C	1.20	8.05	0.15	4.45×10^{-3}	1.67×10^{-4}
C14	C	1.40	7.90	0.18	7.76×10^{-3}	2.65×10^{-4}
C16	C	1.60	7.67	0.21	9.76×10^{-3}	4.49×10^{-4}
Cmx	C	1.85	6.69	0.28	1.18×10^{-3}	1.94×10^{-3}
FPS10	FPS	1.00	7.32	0.14	1.44×10^{-3}	1.50×10^{-4}
FPS12	FPS	1.20	7.30	0.16	1.75×10^{-3}	2.30×10^{-4}
FPS14	FPS	1.40	7.22	0.19	2.22×10^{-3}	3.64×10^{-4}
FPS16	FPS	1.60	7.02	0.23	4.77×10^{-3}	6.38×10^{-4}
FPSmx	FPS	1.80	6.22	0.29	1.45×10^{-3}	2.50×10^{-3}
G10	G	1.01	5.76	0.17	1.73×10^{-3}	5.36×10^{-4}
G12	G	1.20	5.42	0.22	2.10×10^{-3}	1.20×10^{-3}
Gmx	G	1.36	4.62	0.29	2.72×10^{-3}	5.65×10^{-3}
L10	L	1.00	9.61	0.10	5.55×10^{-3}	4.15×10^{-5}
L12	L	1.20	9.76	0.12	3.52×10^{-3}	5.60×10^{-5}
L14	L	1.40	9.89	0.14	5.03×10^{-3}	7.41×10^{-5}
L16	L	1.60	9.98	0.16	7.81×10^{-4}	9.75×10^{-5}
Lmx	L	2.68	9.23	0.29	5.80×10^{-4}	9.17×10^{-4}
N10	N	1.00	8.81	0.11	6.38×10^{-4}	5.70×10^{-5}
N12	N	1.20	8.98	0.13	7.05×10^{-4}	7.59×10^{-5}
N14	N	1.40	9.13	0.15	7.81×10^{-4}	9.97×10^{-5}
N16	N	1.60	9.24	0.17	2.33×10^{-3}	1.30×10^{-4}
Nmx	N	2.63	8.65	0.30	7.08×10^{-4}	1.20×10^{-3}
O10	O	1.00	8.29	0.12	1.41×10^{-3}	7.39×10^{-5}
O12	O	1.20	8.41	0.14	1.64×10^{-3}	1.03×10^{-4}
O14	O	1.40	8.50	0.16	1.96×10^{-3}	1.43×10^{-4}
O16	O	1.60	8.54	0.19	2.45×10^{-3}	1.97×10^{-4}
Omx	O	2.38	7.75	0.31	5.15×10^{-3}	1.66×10^{-3}
SLy10	SLy4	1.00	7.78	0.13	7.72×10^{-4}	1.12×10^{-4}
SLy12	SLy4	1.20	7.80	0.15	8.41×10^{-4}	1.66×10^{-4}
SLy14	SLy4	1.40	7.78	0.18	9.17×10^{-4}	2.45×10^{-4}
SLy16	SLy4	1.60	7.70	0.21	2.57×10^{-3}	3.70×10^{-4}
SLymx	SLy4	2.05	6.71	0.30	8.74×10^{-4}	2.50×10^{-3}
WFF10	WFF3	1.00	7.29	0.14	9.86×10^{-4}	1.46×10^{-4}
WFF12	WFF3	1.20	7.30	0.16	1.10×10^{-3}	2.18×10^{-4}
WFF14	WFF3	1.40	7.26	0.19	1.23×10^{-3}	3.34×10^{-4}
WFF16	WFF3	1.60	7.14	0.22	3.36×10^{-3}	5.48×10^{-4}
WFFmx	WFF3	1.84	6.40	0.29	1.18×10^{-3}	2.18×10^{-3}

Chapter 3

Perturbations of non-rotating stars

Perturbation theory of spherical spacetimes [166, 213, 206, 137, 138] has been, historically, the first approach to the study GW emitted from an oscillating black hole [160, 75], during gravitational collapse [164, 165] and as consequence of NS oscillations. Although most of the work in perturbation theory has been done using a frequency-domain approach in order to accurately compute the wave frequencies [66, 34, 136, 111, 163, 194, 195, 62, 129, 67, 14], time-domain simulations are also needed to compute full waveforms [13, 6, 86, 169, 170, 85, 141, 140, 139, 84, 186, 153, 155]. In particular, Allen et al. [6], via a multipolar expansion, derived the equations for the even parity perturbations of spherically symmetric relativistic stars and produced explicit waveforms. The problem was reduced to the solution of a set of 3 wave-like hyperbolic PDE, coupled to the Hamiltonian constraint: two equations for the metric variables, in the interior and in the exterior of the star, and one equation for the fluid variable in the interior. The Hamiltonian constraint was preserved, modulo numerical errors, during the evolution. Ruoff [169] derived the same set of equations directly from the ADM [21, 69] formulation of Einstein's equations and used a similar procedure for their solution.

We present in this Chapter the equations governing the perturbations of non-rotating stars obtained specifying to the Regge-Wheeler gauge and to a static background, the general gauge-invariant and coordinate-independent formalism developed in [94, 95, 101, 135] by Gerlach and Sengupta, and Gundlach and Martin-Garcia (GSGMG formalism, hereafter). The resulting system of equations is equivalent to the formulation of [6, 169]. Then the main features of a new time-domain code solving these equations are described. In particular, for the even-parity perturbation equations, a *constrained* algorithm, different from any in [6, 169] and proposed by Nagar [139, 141, 140], is adopted and implemented in the new code with standard finite differencing methods. This scheme permits long-term and stable simulations and give very accurate results in studying the gravitational waveforms (as we will demonstrate in Chap. 4).

3.1 Gauge-invariant coordinate-independent formalism for spherical spacetime perturbations

The gauge-invariant coordinate independent formalism for spherical spacetime perturbations was originally introduced by Gerlach and Sengupta [94, 95] and further developed by Gundlach and Martin-Garcia [101, 135]. It can be applied to the description of linear perturbation of system that have small non-spherical deviations from spherical symmetry. The formalism has many interesting features: it is coordinate independent (equations are expressed using the *frame derivatives*), the perturbations fields are linearly gauge-independent and the only hypothesis on the background is the spherical symmetry (the common assumption of static background is relaxed). In astrophysics this framework can be applied to the investigations of the gravitational radiation emission from supernova explosion as well as from stellar oscillations.

The most general spherically symmetric spacetime is a manifold $\mathcal{M} = M^2 \times S^2$, product of a Lorentzian 2-metric with the 2-spheres. The metric is given by:

$$g_{\mu\nu} \equiv \text{diag}\left(g_{AB}, r^2 s_{ab}\right) \ , \tag{3.1.1}$$

where g_{AB} is the metric on M^2 to be determined via Einstein equations ($A, B = 0, 1$, upper case Latin indices will be used in the following for quantities in M^2), r is a scalar in M^2 (that can also be used as coordinate): $r = 0$ identifies the boundary of M^2 and each point $p \in M^2$ is a sphere of area $4\pi r^2$, and s_{ab} (lower case Latin indices will be used in the following for quantities in S^2) is the unit curvature metric of S^2. The general stress-energy tensor in spherical symmetry can be written as follow:

$$T_{\mu\nu} \equiv \text{diag}\left(T_{AB}, Qr^2 s_{ab}\right) \ . \tag{3.1.2}$$

The spherical symmetry of the background allows to expand the perturbative fields in tensorial spherical harmonics on S^2, in such a way to specify the perturbation equations to the unknown submanifold M^2. Scalar spherical harmonics on S^2 are defined as the solution of:

$$s^{ab} Y^{\ell m}_{:ab} = -\ell(\ell+1) Y^{\ell m} \tag{3.1.3}$$

where ":" indicates the covariant derivative in S^2. A basis for the vector fields on S^2 defined for $\ell \geqq 1$ is:

$$Y^{\ell m}_{:a} \qquad \text{and} \qquad S^{\ell m}_a \equiv \epsilon_a^{\ b} Y^{\ell m}_{:b} \tag{3.1.4}$$

where ϵ_{ab} is the totally covariant unit tensor. A basis for the symmetric 2-tensors instead is:

$$Y^{\ell m} s_{ab} \qquad S^{\ell m}_{a:b} + S^{\ell m}_{b:a} \qquad \text{and} \qquad Z^{\ell m}_{ab} \equiv Y^{\ell m}_{:ab} + \frac{\ell(\ell+1)}{2} Y^{\ell m} s_{ab} \ , \tag{3.1.5}$$

where the last two tensor vanish for $\ell = 0, 1$. Linear perturbation of spherically symmetric spacetime with different values of (ℓ, m) decouple, and each component (or *multipole*) can be considered separately. The index m is degenerate and the equations do not depend on it.

In addition the perturbations with defined ℓ divide in *odd-parity* (or *axial*) and *even-parity* (or *polar*). Fields containing an even parity power of ϵ_{ab} are called polar or even, *e.g.* $Y^{\ell m}_{:a}$, while those containing an odd power, *e.g.* $S^{\ell m}_a$, are called axial or odd. Alternatively stated, if (θ, ϕ) are the standard coordinate of S^2, under a parity transformation: $(\theta, \phi) \to (\pi - \theta, \pi + \phi)$, the axial spherical harmonics transform as $(-1)^{\ell+1}$ and the polar ones as $(-1)^{\ell}$.

The metric perturbations can be parameterized [1] as follows [101]:

$$\delta g^{(\mathrm{o})}_{\mu\nu} = \begin{pmatrix} 0 & h^{\mathrm{odd}}_A S^{\ell m}_a \\ '' & h(S^{\ell m}_{a:b} + S^{\ell m}_{b:a}) \end{pmatrix} \tag{3.1.6a}$$

$$\delta g^{(\mathrm{e})}_{\mu\nu} = \begin{pmatrix} h_{AB} Y^{\ell m} & h^{\mathrm{even}}_A Y^{\ell m}_{:a} \\ '' & r^2 (K Y^{\ell m} s_{ab} + G Y^{\ell m}_{:ab}) \end{pmatrix} , \tag{3.1.6b}$$

the matter perturbations instead are:

$$\delta T^{(\mathrm{o})}_{\mu\nu} = \begin{pmatrix} 0 & \Delta T^{\mathrm{odd}}_A S^{\ell m}_a \\ '' & \Delta T(S^{\ell m}_{a:b} + S^{\ell m}_{b:a}) \end{pmatrix} \tag{3.1.7a}$$

$$\delta T^{(\mathrm{e})}_{\mu\nu} = \begin{pmatrix} \Delta T_{AB} Y^{\ell m} & \Delta T^{\mathrm{even}}_A Y^{\ell m}_{:a} \\ '' & r^2 \Delta T^3 Y^{\ell m} s_{ab} + \Delta T^2 Z^{\ell m}_{ab} \end{pmatrix} . \tag{3.1.7b}$$

These expressions, when inserted into the (linearized) Einstein field equations, give scalar, vectorial and tensorial equations on M^2 that connect the 10 metric fields h^{odd}_A, h, h_{AB}, h^{even}_A, K, G with the matter ones: $\Delta T^{\mathrm{odd}}_A$, ΔT, ΔT_{AB}, $\Delta T^{\mathrm{even}}_A$, ΔT^3, ΔT^2. All the equations depends on the coordinate system (gauge) used.

The problem that naturally arise at this point is the definition of gauge invariant linear perturbations. Even if the coordinate system of the background is fixed, in fact, it is impossible to distinguish between an infinitesimal physical perturbations of the background and an infinitesimal coordinate transformation on the unperturbed background (a "gauge perturbation"). Given a tensor field X on the background spacetime, its linear perturbation δX transform under an infinitesimal coordinate transformation $x^\mu \to x^\mu + \xi^\mu$ as:

$$\delta X \to \delta X + \mathcal{L}_\xi X \tag{3.1.8}$$

and it is mixed with the background field. The perturbation is defined *gauge-invariant* if and only if $\mathcal{L}_\xi X = 0$. Because of the spherical symmetry of the background, it turns out that gauge-invariant perturbations are possible only for $\ell \geqq 2$.

Starting from the general form of the infinitesimal displacement:

$$\xi_\mu = (\xi_A Y^{\ell m}, r^2 \xi^{(\mathrm{e})} Y^{\ell m}_{:a} + r^2 \xi^{(\mathrm{o})} S^{\ell m}_a) \tag{3.1.9}$$

it is possible to construct as linear combinations of the perturbative quantities in Eq. (3.1.6) and in Eq. (3.1.7) new gauge-invariant variables [94]. In the polar case there are 3 infinitesimal coordinate transformation (ξ_A and $\xi^{(\mathrm{e})}$) and 7 metric perturbations leaving 4 gauge-invariant fields. From the axial infinitesimal coordinate transformation and the axial 3 metric perturbation result 2 axial gauge-invariant perturbations. The common procedure is then to fix in a arbitrary gauge the fields h, h^{odd}_A and G and to obtain all the other perturbations in term of them and of the gauge-invariant quantities. A particular choice is the Regge-Wheeler gauge [166]: $h = h^{\mathrm{odd}}_A = G = 0$.

---

[1] Since the multipoles separate, we will consider once at time omitting the up-script $^{(\ell m)}$.

All the gauge-invariant tensor fields are expressed [101, 135] (for a perfect fluid stress-energy tensor) in term of the basis of M^2 composed by the fluid velocity timelike unit vector u_A ($u_\mu = (u_A, 0)$ in spherical symmetry) and the spacelike unit vector $n_A \equiv -\epsilon_{AB} u^B$. In this *fluid frame* all fields are reduced to scalar fields and all the equations are scalar equations written in term of *frame derivatives*:

$$\dot{f} \equiv u^A f_{|A} \qquad f' \equiv n^A f_{|A} \tag{3.1.10}$$

where $|$ indicates the covariant derivative on M^2. The introduction of the fluid frame and the frame derivatives permits the development of a general coordinate independent formalism and, moreover, leads to distinguish evolution equations from constraints and to define a well posed IVP.

3.2 Stellar perturbation equations

The perturbation equations for a non-rotating star can be obtained by specializing to the static case and Regge-Wheeler gauge the general gauge-invariant and coordinate-independent formalism for metric perturbations of spherically symmetric spacetimes described in the previous Section.

The background metric is given in Eq. (2.4.1), assuming perfect fluid matter (see Chap. 2), the equilibrium configuration is the solution of the TOV equations Eq. (2.4.2). In the following we will consider only fluid described by a one-parameter EOS (barotropic fluid), since we are interested in neutron stars. See Appendix A of [139] for the extension of the equations to a two-parameter EOS.

In the Regge-Wheeler gauge, the even-parity metric perturbation multipoles are parameterized by three (gauge-invariant) scalar functions (k, χ, ψ) as [2]

$$\delta g_{\mu\nu}^{(\mathrm{e})} = \begin{pmatrix} (\chi + k)\ e^{2\alpha} & -\psi\ e^{\alpha+\beta} & 0 & 0 \\ '' & (\chi + k)\ e^{2\beta} & 0 & 0 \\ '' & '' & k\ r^2 & 0 \\ '' & '' & '' & k\ r^2 \sin^2\theta \end{pmatrix} Y^{\ell m} \tag{3.2.1}$$

where $Y^{\ell m}$ are the usual scalar spherical harmonics. Here χ parameterizes the actual GW inside matter, while k is the perturbed conformal factor. Since the background is static, the third function ψ is not independent from the others, but can be obtained from k and χ solving the equation [101] (for $r < R$)

$$\psi_{,t} = -e^{\alpha-\beta} \left[2e^{2\beta} \left(\frac{m}{r^2} + 4\pi r p \right) (\chi + k) + \chi_{,r} \right] . \tag{3.2.2}$$

This equation also holds for $r > R$ with $m(r) = M$. In addition, when the background is static the metric perturbations are actually described by two degrees of freedom, (k, χ), only in the interior [101], while only one degree of freedom remains in the exterior.

A priori there is no unique way of selecting which evolution equations to use for numerical simulations (the ones most convenient mathematically could not be so numerically) so that different formulations of the problem have been numerically explored in the literature [6, 169, 101, 141]. In particular, Ref. [141]

---

[2] We omit hereafter the multipolar indexes for convenience of notation, *e.g.* , $k \equiv k_{\ell m}$, $\chi \equiv \chi_{\ell m}$ and $\psi = \psi_{\ell m}$.

showed that it can be useful to formulate the even-parity perturbations problem using a *constrained scheme*, with one elliptic and two hyperbolic (wave-like) equations. One hyperbolic equation is used to evolve χ in the interior and exterior; the other hyperbolic equation serves to evolve, in the interior, the perturbation of the relativistic enthalpy $H \equiv \delta p/(p+\varepsilon)$ (do not confuse it with the heat function defined in Chap. 1), where δp is the pressure perturbation. The quantity H parameterizes the pulsations of the fluid. The system is closed by the elliptic equation, the Hamiltonian constraint, that is solved for k. Following Ref. [141] we express the equations in term of an auxiliary variable $S \equiv \chi/r$, whose amplitude tends to a constant for $r \to \infty$ and thus is more convenient for the numerical implementation. We recall that the variable S is the same used by Ruoff [169] and the relationship with the variables of Allen et al. [6] is given by $k = F_{\text{Allen}}/r$ and $S = e^{-2\alpha}S_{\text{Allen}}$. In the star interior, $r < R$, the evolution equation for S reads

$$\begin{aligned}-S_{,tt}+e^{2(\beta-\alpha)}S_{,rr}=e^{2\alpha}\Bigg\{&-\left[4\pi r(5p-\varepsilon)+\frac{6m}{r^2}\right]S_{,r}+\\ &+\left[-4e^{2\beta}\left(\frac{m}{r^2}+4\pi rp\right)^2-4\pi(3\varepsilon+5p)+\frac{2}{r^2}\left(1+\frac{m}{r}\right)+\frac{(\ell-1)(\ell+2)}{r^2}\right]S+\\ &-\left[2e^{2\beta}\left(\frac{m}{r^2}+4\pi rp\right)^2+8\pi\varepsilon-\frac{6m}{r^3}\right]\frac{2k}{r}\Bigg\}\ ,\end{aligned} \tag{3.2.3}$$

the one for H becomes

$$\begin{aligned}-H_{,tt}+C_s^2e^{2(\beta-\alpha)}H_{,rr}=e^{2\alpha}\Bigg\{&\left[\frac{m}{r^2}(1+C_s^2)+4\pi pr\left(1-2C_s^2\right)+\right.\\ &\left.+\left(4\pi r\varepsilon-\frac{2}{r}\right)C_s^2\right]H_{,r}-\left[4\pi(p+\varepsilon)(3C_s^2+1)-C_s^2\frac{\Lambda}{r^2}\right]H+\\ &+\frac{1}{2}\left(\frac{m}{r^2}+4\pi pr\right)(1-C_s^2)(rS_{,r}-k_{,r})+\\ &+\left[\frac{2(m+4\pi pr^3)^2}{r^3(r-2m)}-4\pi C_s^2(3p+\varepsilon)\right](rS+k)\Bigg\}\end{aligned} \tag{3.2.4}$$

and finally the Hamiltonian constraint is

$$\begin{aligned}\left(1-\frac{2m}{r}\right)k_{,rr}+\left[\frac{2}{r}-\frac{3m}{r^2}-4\pi\varepsilon r\right]k_{,r}-\left[\frac{\Lambda}{r^2}-8\pi\varepsilon\right]k=-\frac{8\pi(p+\varepsilon)}{C_s^2}H+\\ +\left(1-\frac{2m}{r}\right)S_{,r}+\left[\frac{2}{r}-\frac{2m}{r^2}+\frac{\Lambda}{2r}-8\pi\varepsilon r\right]S\end{aligned} \tag{3.2.5}$$

where $\Lambda \equiv \ell(\ell+1)$. Eq. (3.2.3) and Eq. (3.2.5) are also valid in the exterior, with $C_s^2 = p = H = 0$, $m(r) = M$ and $e^{2\alpha} = 1-2M/r$. Since in the star exterior the spacetime is described by the Schwarzschild metric, the perturbation equations can be combined together in the Zerilli equation [213]

$$\Psi^{(\text{e})}_{,tt}-\Psi^{(\text{e})}_{,r_*r_*}+V^{(\text{e})}_\ell\Psi^{(\text{e})}=0 \tag{3.2.6}$$

for a single, gauge-invariant, master function $\Psi^{(\text{e})}$, the *Zerilli-Moncrief function* [213, 137]. The function $V^{(\text{e})}_\ell$ is the Zerilli potential (see for example [143]) given by

$$V^{(\mathrm{e})} = -\left(1-\frac{2M}{r}\right)\frac{\Lambda(\Lambda-2)^2r^3+6(\Lambda-2)^2Mr^2\left[(\Lambda-2)+6M\right]+72M^3}{r^3\left[(\Lambda-2)r+6M\right]^2}\times \tag{3.2.7}$$
$$\times\frac{\Lambda(\Lambda-2)^2r^3+6(\Lambda-2)^2Mr^2+36(\Lambda-2)M^2r^2+72M^3}{r^3[(\Lambda-2)r+6M]^2}\,,$$

and

$$r_* \equiv r + 2M\ln\left[\frac{r}{2M}-1\right] \tag{3.2.8}$$

is the Regge-Wheeler tortoise coordinate. In terms of the gauge-invariant functions χ and k, the Zerilli-Moncrief function reads

$$\Psi^{(\mathrm{e})} = \frac{2r(r-2M)}{\Lambda[(\Lambda-2)r+6M]}\left[\chi - rk_{,r}+\frac{r\Lambda+2M}{2(r-2M)}k\right]\,. \tag{3.2.9}$$

The inverse equations can be found, for instance, in Ref. [169]. In our notation they read

$$k = 2e^{2\alpha}\Psi^{(\mathrm{e})}_{,r}+\left\{\frac{\Lambda}{r}-\frac{12Me^{2\alpha}}{r[r(\Lambda-2)+6M]}\right\}\Psi^{(\mathrm{e})}, \tag{3.2.10}$$

$$\chi = 2e^{2\alpha}\Psi^{(\mathrm{e})}_{,rr}+\frac{2M}{r^2}\left(1-\frac{6re^{2\alpha}}{r(\Lambda-2)+6M}\right)\Psi^{(\mathrm{e})}_{,r}+ \tag{3.2.11}$$
$$+\frac{2}{r^2}\left[\frac{3M}{r}-\Lambda+\frac{6M}{r(\Lambda-2)+6M}\left(3-\frac{8M}{r}-\frac{6Me^{2\alpha}}{r(\Lambda-2)+6M}\right)\right]\Psi^{(\mathrm{e})}\,.$$

Let's mention briefly the boundary conditions to impose to these equations. At the center of the star all the function must be regular, and this leads to the conditions:

$$\chi \sim r^{\ell+2} \tag{3.2.12a}$$
$$k \sim r^{\ell+1} \tag{3.2.12b}$$
$$H \sim r^{\ell}\,. \tag{3.2.12c}$$

At the star surface S is continuous as well as its first and second radial derivatives. On the contrary, k and its first radial derivative are continuous but $k_{,rr}$ can have a discontinuity due the term $8\pi(p+\varepsilon)H/C_s^2$ in Eq. (3.2.5). At the star surface, $r=R$, Eq. (3.2.4) reduces to an ODE for H, that is solved accordingly.

The odd parity perturbations are related with stellar rotation rather than stellar pulsation. In the latter case, in fact, the fluid should experience pressure oscillations that are perturbation with a scalar spherical harmonics angular dependence: there are no scalar spherical harmonics with odd parity. On a static background moreover, the odd-parity perturbations are described by a single, gauge-invariant, dynamical variable $\Psi^{(\mathrm{o})}$, that is totally decoupled from matter. This function satisfies a wave-like equation of the form [94, 67]

$$\Psi^{(\mathrm{o})}_{,tt}-\Psi^{(\mathrm{o})}_{,\bar{r}_*\bar{r}_*}+V^{(\mathrm{o})}_{\ell}\Psi^{(\mathrm{o})}=0, \tag{3.2.13}$$

with a potential

$$V^{(\mathrm{o})}_{\ell} = e^{2\alpha}\left(\frac{6m}{r^3}+4\pi(p-\varepsilon)-\frac{\Lambda}{r^2}\right)\,. \tag{3.2.14}$$

This equation has been conveniently written in terms of the "star-tortoise" coordinate $\bar{r}_*$ defined by

$$\frac{\partial \bar{r}_*}{\partial r} = e^{\beta-\alpha} \; . \tag{3.2.15}$$

In the exterior, $\bar{r}_*$ reduces to the Regge-Wheeler tortoise coordinate r_* introduced above and Eq. (3.2.13) becomes the well-known Regge-Wheeler equation [166]. The relation between $\Psi^{(\mathrm{o})}$ and the odd-parity metric multipoles is given, for example, by Eqs. (19)-(20) of Ref. [143].

The principal quantities for GWs are the gauge-invariant functions $\Psi^{(\mathrm{e/o})}$. These functions are directly related to the "plus" and "cross" polarization amplitudes of the GWs by (see *e.g.* [143, 132] and Chap. 5):

$$h_+ - \mathrm{i}h_\times = \frac{1}{r}\sum_{\ell=2}^{\infty}\sum_{m=-\ell}^{\ell} N_\ell \left(\Psi^{(\mathrm{e})}_{\ell m} + \mathrm{i}\Psi^{(\mathrm{o})}_{\ell m}\right) {}_{-2}Y_{\ell m}(\theta,\phi) \tag{3.2.16}$$

where $N_\ell = \sqrt{(\ell+2)(\ell+1)\ell(\ell-1)}$ and ${}_{-2}Y_{\ell m}$ are the spin-weighted spherical harmonics of spin-weight $s=-2$. The GWs luminosity at infinity is given by

$$\frac{dE}{dt} = \frac{1}{16\pi}\sum_{\ell=2}^{\infty}\sum_{m=-\ell}^{\ell} N_\ell^2 \left(\left|\dot{\Psi}^{(\mathrm{e})}_{\ell m}\right|^2 + \left|\dot{\Psi}^{(\mathrm{o})}_{\ell m}\right|^2\right) \tag{3.2.17}$$

where the over-dot stands for derivative with respect to coordinate time t. The energy spectrum reads

$$\frac{dE}{d\omega} = \frac{1}{16\pi^2}\sum_{\ell=2}^{\infty}\sum_{m=-\ell}^{\ell} N_\ell^2\omega^2 \left(\left|\tilde{\Psi}^{(\mathrm{e})}_{\ell m}\right|^2 + \left|\tilde{\Psi}^{(\mathrm{o})}_{\ell m}\right|^2\right) \tag{3.2.18}$$

where $\tilde{\Psi}^{(\mathrm{e/o})}_{\ell m}$ indicates the Fourier transform of $\Psi^{(\mathrm{e/o})}_{\ell m}$, $\omega = 2\pi\nu$ and ν is the frequency.

3.3 The PERBACCO

PERBACCO (*Pertur**Ba**tive **C**ostrained **Co**de*) is a code to solve in the time domain the equations for all kind of perturbations of a TOV star. It is a development of that described in [139] and successfully used in many works [140, 141]. The original routines have been re-written in `FORTRAN 90` and merged in a unique code with the addition of new evolution schemes, new initial data, a subroutine to solve radial perturbations and the possibility to use tabulated EOS.

The TOV equations Eq. (2.4.2) are integrated numerically from the center outward, for a given value of central pressure p_c, using a standard fourth-order Runge-Kutta integration scheme with adaptive step size.

To evolve numerically the perturbations equations, we introduce an evenly spaced grid in r with uniform spacing Δr and we adopt finite differencing approximation schemes for the derivatives. In particular, in the construction of the the computational grid we set $\Delta r = (R - r_{\min})/(J_i - 1/2)$ with $r_{\min} \simeq 0$, the origin $r = 0$ is excluded and we located the first point at $r = \Delta r/2$. The resolution is measured as the number of point J_i inside the star radius. The star surface is located at a cell center $r_{J_i-1} < R < r_{J_i}$.

In the even-parity case the hyperbolic evolution equations for S and H are all solved with standard, second order convergent in time and space, algorithms (leapfrog, upwind or Lax-Wendroff). The Hamiltonian constraint is used to update, at every time step, the variable k. This elliptic equation is discretized in space at second order and reduced to tridiagonal linear system that is inverted using robust and fast ($\mathcal{O}(J_i)$ operations) LU decomposition [161]. For this reason the evolution scheme of the polar perturbations can be considered a *constrained evolution*. The inner boundary conditions of Eq. (3.2.12) are implemented by setting to zero the variables at the first grid point. At the outer boundary, standard radiative Sommerfeld conditions are imposed.

The Zerilli-Moncrief function has been obtained in two (independent) ways. On the one hand, it has been computed from S (χ) and k using Eq. (3.2.9) for every value of r. On the other hand, it has been computed using Eq. (3.2.9) only at the star surface ($r = R$, the "matching point") and then evolved using Eq. (3.2.6). The second method is used only as an independent consistency check.

In the odd-parity case Eq. (3.2.13) is also solved with standard algorithms, second order convergent in time and space. Boundary conditions are implemented in the same way of even-parity case. Finally, for the radial perturbations, the equation for the Lagrangian displacement (see [69]) is solved in a similar manner.

We performed extensive simulations to test the code. The scheme is stable and permits us to accurately evolve the equations as long as we wish. Simulations of about one second are showed and discussed in Sec. 4.3.3, during these evolutions the norms of the evolved quantities are almost constant with small oscillations around the initial value. To check convergence of the waves, in addition to what previously done in [139], we ran simulations with polytropic EOS and resolutions $J_i = \{50, 149, 446\}$ which correspond, respectively, to $\Delta r = 0.2$ and $\Delta r/3$ and $\Delta r/9$. The initial data were (see below) of type 3 for the axial part and of type 1 for the polar one. We check both the convergence of the waves in time, *i.e.* $\Psi^{(\mathrm{e/o})}(t)$ and the convergence in space of an "energy" defined by means of Eq. (3.2.17) but computed at finite radius [3] . For what concern the axial part, the Regge-Wheeler function converge as expected at second order, *i.e.* up to terms, $\mathcal{O}(\Delta r^2)$. In the polar sector, the Zerilli-Moncrief function computed by Eq. (3.2.9) from the constrained evolution does not exhibit, unfortunately, pure second order convergence but only first order is fully reached. All the schemes used in the algorithm are second order convergent but first order approximations are used for the boundaries: while this does not represent a problem for the hyperbolic equations (the loss in convergence is "localized" and to cure it is sufficient to use grids large enough), in the case of the elliptic equation the entire solution is affected by that inaccuracy. On the other hand the use of first order boundaries permits to reduce the elliptic equation in tridiagonal form and thus to adopt a faster and simpler algorithm for the inversion. A lower convergence factor is the "price" we pay for the stability, but we believe that this is not a real limitation since large resolutions runs can be easily handed even on workstations. At sufficient high resolution the properties of the waves extracted are not affected: comparing the relative differences in amplitude be-

---

[3] The time derivative in Eq. (3.2.17) has been computed with 4-th order finite differencing scheme while the integral with trapezi rule. This settings do not introduce, in principle, further numerical inaccuracies being second order, or more, accurate.

tween resolution $J_i = 50$ and $J_i = 149$ and between $J_i = 149$ and $J_i = 446$, we checked that they are of the order 3% and 1% respectively, while relative differences in frequencies are below 1% and 0.3%. For all practical purpose, running simulations with resolution $J_i \geq 300$ ensure to be in the convergent regime.

Some results that validate the physical results of the code can be found in Ref. [140] while a detailed discussion is the subject of Chap. 4.

3.3.1 Initial data

In principle the choice of the initial data for the perturbation equations should take into account, at least approximately, the astrophysical scenario in which the neutron star is born. Such scenario could be, for example the gravitational collapse or the merger of two neutron stars. Only long-term simulations in full general relativity can investigate highly nonlinear and non-isotropic system until they settle down in a, almost spherical, quasi-equilibrium configuration. A perturbative analysis could then start from this point once the metric and matter tensors had been projected along the corresponding (tensorial) spherical harmonics. This approach, in principle possible, is however beyond the scopes of the present work.

Inspired by previous perturbative calculations [6, 169], we implement in the PerBaCCo different kinds of initial data such that they are the simplest, well-posed and involve perturbations of both the fluid and/or the metric quantities.

In the case of the even parity perturbations 3 different initial excitations can be evolved:

1. *Conformally Flat Initial Data.* We set $S(0,r) = 0$ and give a fluid perturbation of type:

   $$H(0,r) = A\left(\frac{r}{R}\right)^{\ell-1} \sin\left(\pi(n+1)\frac{r}{R}\right). \tag{3.3.1}$$

   The function $k(0,r)$ is computed consistently solving the Hamiltonian constraint. The profile of H in Eq. (3.3.1) is chosen in order to approximate the behavior of an enthalpy eigenfunction with n nodes. In this way, only some modes can be (prominently) excited. To focus for example the principal fluid modes one could chose a *zero-nodes* initial data setting $n = 0$.

2. *Radiative Initial Data.* We set $k(0,r) = 0$ and $H(0,r)$ as Eq. (3.3.1). The function $S(0,r)$ is computed consistently solving the Hamiltonian constraint.

3. *Scattering-like Initial Data.* We set $H(0,r) = 0$ and $\Psi^{(\mathrm{e})}(0,r)$ as a Gaussian pulse:

   $$\Psi^{(\mathrm{e})}(0,r) = A\exp\left(-\frac{(r-r_{\mathrm{c}})^2}{b^2}\right), \tag{3.3.2}$$

   The functions $k(0,r)$ and $S(0,r)$ are computed consistently from Eq. (3.2.10) and Eq. (3.2.11).

Initial data of type 1 and 2 are chosen to be time-symmetric ($S_{,t} = k_{,t} = H_{,t} = 0$). On the one hand, this choice can be physically questionable because the system has an unspecified amount of incoming radiation in the past. On the other hand, it is the simplest choice and guarantees that the momentum

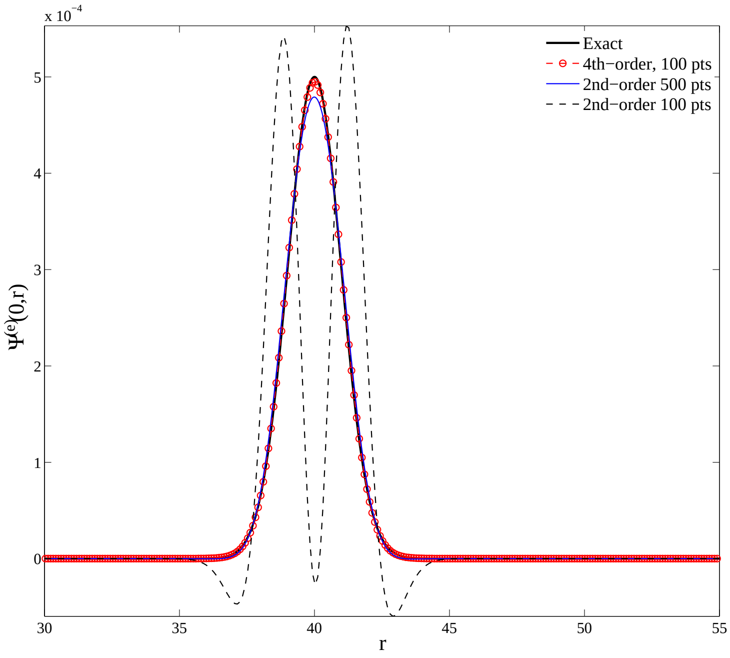

Figure 3.1: Initial data of type 3 (See text) for a perturbative evolution. Convergence of the Zerilli-Moncrief function as a function of the radial coordinate. Only high resolution and/or an high accuracy in the computation in the (finite differencing) derivative $\partial_r k$ give reliable initial data.

constraints are trivially satisfied and only the Hamiltonian constraint needs to be used for the setup. The Gaussian in type 3 initial data is *in-going*, i.e. $\Psi_{,t} = \Psi_{,r_*}$, and the derivatives of the other variables are computed consistently with this choice.

In the case of odd-parity perturbations we start the evolution using an in-going narrow Gaussian as in Eq. (3.3.2) for $\Psi^{(\mathrm{o})}(0, r)$. We stress that this is a simple, but sufficiently general, way to represent a “distortion” of the space-time (whose intimate origin depends on the particular astrophysical setting), and to introduce in the system a proper scale through the width of the Gaussian.

In some situations, the convergence of the Zerilli-Moncrief computed from Eq. (3.2.9) can be particularly delicate. For example, in case of type 3 initial data, a very accurate computation of the radial derivative $k_{,r}$ is needed to obtain an accurate and reliable $\Psi^{(\mathrm{e})}$ from k and S. Fig. 3.1 summarizes the kind of problem that one can find computing the Zerilli-Moncrief function too naively. It refers to $\Psi^{(\mathrm{e})}(r)$ for $(\ell, m) = (2, 0)$ at $t = 0$. We consider (for simplicity of discussion) a polytropic model, *i.e.* $p = K\rho^{\Gamma}$ with $K = 100$, $\Gamma = 2$ and $\rho_c = 1.28 \times 10^{-3}$ with type 3 initial data ($A = 0.1$, $b = M$ and $r_c = 40$). We fixed $\Psi^{(\mathrm{e})}$ by Eq. (3.3.2), we computed χ and k from Eq. (3.2.10) and Eq. (3.2.11), $\partial_r k$ numerically using finite differencing schemes and then we reconstructed

$\Psi^{(\mathrm{e})}$ via Eq. (3.2.9). Fig. 3.1 shows that, for low resolution ($J_i = 100$), using a second-order finite-differencing standard stencil to compute $\partial_r k$ is clearly not enough, as the reconstructed (thicker dashed-dot line) and the "exact" (solid line) $\Psi^{(\mathrm{e})}$ are very different. Increasing the resolution (to 500 points) improves the agreement, which is however not perfect yet (thinner dashed-dot line). A visible improvement is obtained using higher order finite-differencing operators: the figure shows that a 4th-order operator (already in the low-resolution case with $J_i = 100$ points) is sufficient to have an accurate reconstruction of the Zerilli-Moncrief function.

The conclusion is that one needs to use *at least* 4th-order finite-differencing operators to compute accurately $\Psi^{(\mathrm{e})}$ from χ and k. If this is not done, the resulting function is not reliable and it can't be considered a solution of Eq. (3.2.6). Typically, we have seen that, when this kind of inaccuracy is present, the amplitude of (part of) the Zerilli-Moncrief function (usually the one related to the w-mode burst) grows linearly with r instead of tending to a constant value for $r \to \infty$. A very detailed discussion of this problem will be presented in Sec. 6.6.

Chapter 4

Gravitational waves from neutron star linear oscillations

The pioneering works of Vishveshwara [205], Press [160] and Davis, Ruffini and Tiomno [75], unambiguously showed that a non-spherical gravitational perturbation of a Schwarzschild black hole is radiated away via exponentially damped harmonic oscillations. These oscillations are interpreted as space-time vibrational modes. The properties of these *quasi-normal modes* (QNMs henceforth, see App. A) of black holes have been thoroughly studied since then, see for example Refs. [68, 93, 115] and references therein.

Gravitational waves from relativistic stars are also characterized by the sign of the proper mode of oscillations the emitting star. The QNMs frequencies carry information about the internal composition of the star and, once detected, they could, in principle, be used to put constraints on the values of mass and radius and thus on the Equation of State (EOS) of a NS [14]. In general these non-spherical oscillations are of two types [187, 115, 147]: *fluid modes*, related to the fluid pulsations and which have a Newtonian counterpart, and *spacetime* or *curvature* modes, which exist only in relativistic stars and are weakly coupled to matter. The former in particular are classified [114], as the *fundamental* or f-mode with typical frequencies around $\nu_f \sim 3$ kHz and damping time $\tau_f \sim 0.1$ s, *pressure* or p-modes whose restoring force is pressure ($\nu_{p_1} > 4$ kHz, $\tau_{p_1} \sim 0.6$ s) and *gravity* or g-modes whose restoring force is gravity (present only in non-isentropic star, $T \neq 0$) and *rotational* or r-modes typical of rotating stars. The latter are spacetime vibrational modes, the so-called w-modes [116]. The fundamental w-mode frequency of a typical NS is expected to lie in the range of $10 \div 12$ kHz and to have a damping time of $\sim 10^{-4}$ s [15].

In this Chapter we present results obtained by PerBaCCo simulations: various kind of initial data for odd and even-parity perturbations have been evolved for 47 NS models computed from 10 different EOS. The GW computed have been studied in great details and in different aspect: comparing star w-modes with black hole QNMs, investigating the effect of the EOS and the compactness on proper frequencies, and exploring techniques to extract them from the waves. These results extend and complete the previous work by Allen et al. [6]

and Ruoff [169]. Moreover, the results obtained prove the performances of the PERBACCO and pose the basis to be used as test-bed for nonlinear code.

4.1 Analysis methods

Once obtained a waveform $\Psi(t)$ from a numerical simulation it is in general necessary to understand the physical (dynamical) origin of the different parts of the wave, and in particular to "quantify" the signal, *i.e.* to extract amplitude, phase and frequencies.

Two complementary methods can be used to obtain such important knowledge. On the one hand, one can use the Fourier analysis and look at the energy spectrum of the wave (See Eq. (3.2.18)) On the other hand, one can perform a "fit analysis" based on specific template for the wave. In the case of stellar oscillations around the equilibrium configuration, the wave are expected to be characterized by one or more frequencies related to the proper modes of the star, *i.e.* the QNMs. As a consequence it is natural to assume that, on a given interval $\Delta t = [t_{\rm i}, t_{\rm f}]$, the waveform can be written as a superposition of N exponentially damped sinusoids, the QNMs expansion:

$$\Psi(t) = \sum_{n=0}^{N} A_n \cos\left(\omega_n t + \phi_n\right) \exp\left(-\alpha_n t\right) \ , \tag{4.1.1}$$

of frequencies $\nu_n = \omega_n / 2\pi$ and damping times $\tau_n \equiv 1/\alpha_n$. Using a non-linear fit procedure one can estimate the values of ω_n, α_n, A_n and ϕ_n from the signal $\Psi(t)$ that are, a priori, unknown. Typically the method used is the standard least-squares fit based on the reduced χ^2 minimization [161]. Alternatively the fit can be performed with different techniques like, for example, the least-square Prony methods, already used to this specific purpose (see *e.g.* Ref. [45]).

The outcome of a numerical simulation is a time series f_j, *i.e.* a discrete set of (floating-point) numbers describing the the physical quantity $\Psi(t)$. After a Fourier or fit analysis, *i.e.* after knowing the proper frequencies of the system, the questions that emerge in the analysis of the waveforms are: "How far" are two signals? What is the "global difference" between two signals? (and also "How good" is the fit?). The answer requires a way to quantify the "distance" between two time series. To this aim, and taking into account that we are typically dealing with functions of the type in Eq. (4.1.1), we consider the (l^2) scalar product

$$\Theta(f,g) \equiv \frac{\sum_j f_j g_j}{\sqrt{\sum_j \left(f_j\right)^2}\sqrt{\sum_j \left(g_j\right)^2}} \ , \tag{4.1.2a}$$

from which one can define the "residual"

$$\mathcal{R}(f,g) \equiv 1 - \Theta(f,g) \tag{4.1.2b}$$

which is bounded in the interval [0, 1], and it is exactly 0 when the two time series are identical. This residual gives a measure of a "relative" distance between f_j and g_j. As a second measure of the global distance (agreement) of two time series we use the l^∞ distance:

$$\mathcal{D}(f,g) \equiv \max_j |f_j - g_j| \, , \tag{4.1.3}$$

that gives the maximum, or "absolute", difference between f_j and g_j.

In the following Sections (and Chapters) we use systematically and all together these methods to investigate the waveforms explicitly computed from time-domain code, showing how, in most of all the cases, they are simple and powerful instruments to extract reliable informations from gravitational wave signals.

4.2 Odd-parity waves

As stated in Sec. 3.2 odd-parity perturbations of stars do not involve fluid pulsations but they are related to pure spacetime vibrations. The gravitational waves from odd-parity perturbations of relativistic star are indeed interpreted, in analogy with the black holes case, a sum of *curvature* or "w" (quasi-normal) modes [147, 115].

The issue of the excitation of w-modes in astrophysically motivated scenarios has been deeply investigated in the literature. Andersson and Kokkotas [13] showed that, in the odd-parity case, the scattering of a Gaussian pulse of gravitational waves off a constant density non rotating star generates a waveform that, in close analogy with the black hole case, is characterized by three phases: (i) A *precursor*, mainly related to the choice of the initial data and determined by the backscattering of the background curvature while the pulse is entering in the gravitational field of the star; (ii) A *burst*; (iii) A *ring-down* phase dominated by w-modes, whose presence was inferred by looking at the Fourier spectrum of the signals. Since the star is non-rotating, the signal eventually dies out with a power-law *tail* typical of Schwarzschild space-time [164, 165]. Allen and coworkers [6] and Ruoff [169] addressed, by means of time-domain perturbative analysis, the same problem in the even-parity case, focusing on gravitational wave scattering scenarios. They considered a large sample of initial configurations as well as star models of different compaction. Their main findings were: (i) w-modes are present only for non-conformally flat initial data (*i.e.* , some radiative field needs to be injected in the system) and (ii) The strength of the w-mode signal depends on the compaction of the star. These pioneering studies were later extended or refined in Refs. [198, 86, 199, 170, 154, 153, 159, 99, 41, 12, 11]. In particular, Refs. [198, 86, 199, 170] considered the scattering off the star of particles moving along open orbits and realized that the w-mode excitation strongly depends on the orbital parameters: the closer the turning point of the orbit is to the star (*i.e.* , the higher is the frequency of the gravitational wave instantaneously emitted by the particle), the larger is the presence of w-modes. Consistently, Ref. [141] showed that (modulo a simplified treatment of the star surface) if the source of perturbation is a spatially extended axisymmetric distribution of fluid matter (like a quadrupolar shell) plunging on the star, the w-modes are not excited, but the energy spectrum is dominated by low-frequency contributions due to curvature backscattering. In addition, Ref. [156] addressed the late-time decay of the *trapped* mode for ultra-compact, highly relativistic constant density stars. The presence of trapped w-modes in stars with a first-order phase transition (a density discontinuity) was also discussed in Ref. [16].

Table 4.1: Equilibrium properties of NS models described by the polytropic EOS in Eq. (1.3.28) and by constant-energy density EOS $\varepsilon = \text{const}$ (the latter models are labeled by the subscript $_C$). From up to down the rows report: the polytropic constant K, the polytropic index Γ, the mass of the star M, its radius R, the central pressure p_c, the central total energy density ε_c and the compaction parameter M/R, for all the stellar models considered.

Model	A	B	A_C	B_C
K	56.16	82.69	—	—
Γ	2	2	—	—
M	1.40	1.40	1.40	1.40
R	6.64	9.10	6.64	9.10
p_c	8.84×10^{-4}	1.83×10^{-4}	2.13×10^{-4}	4.98×10^{-5}
ε_c	3.96×10^{-3}	1.48×10^{-3}	1.14×10^{-3}	4.43×10^{-4}
M/R	0.21	0.15	0.21	0.15

4.2.1 Comparison with black holes

Mathematically the problems of the odd-parity perturbations of a black hole is described by the Regge-Wheeler function solution of Eq. (3.2.13), where the star-tortoise coordinate is substituted by the standard tortoise coordinate and the potential is everywhere the potential of the star exterior (*i.e.* Eq. (3.2.14) with $p = \varepsilon = 0$ and $m = M$). The only important differences are that, in the black hole case, the tortoise coordinate, Eq. (3.2.8), spans the range $(-\infty, \infty)$ and the potential, as a function of this coordinate, has a maximum around $r_* \sim 3M$, and decays exponentially for $r_* \to -\infty$. In the case of the star the star-tortoise coordinate, Eq. (3.2.15), spans the range $(0, +\infty)$, the potential is different in the star interior, it goes to $+\infty$ for $\bar{r}_* \to 0$ and, like the black hole case, it behaves as $\sim \ell(\ell+1)/r_*^2$ for $r_* \to +\infty$.

We analyze in this section the gravitational wave response of relativistic stars of $M = 1.4$ and of a black hole of the same mass to an impinging gravitational wave-packet of the form Eq. (3.3.2). We focus on the dependence of the excitation of the star $\ell = 2, 3$ w-modes (and of the black hole QNMs) ring-down on the width b.

The NS models are described by two different EOS, namely a polytropic EOS of type Eq. (1.3.28) and a, quite unphysical, constant-energy density EOS: $\varepsilon = const$, for which the TOV equations (Eq. (2.4.2)) admit an analytic solution (see *e.g.* [69]). For each EOS two representative models, A and B, are computed in such a way to contrast results from different compactness stars: $M/R = 0.21$ and $M/R = 0.15$ respectively. Tab. 4.1 list the equilibrium properties.

Let us also summarize the basilar elements of the numerical procedure. As done in the PerBaCCo for the star case, in the black hole case Eq. (3.2.13) has been discretized on an evenly spaced grid in r_* (in r for the star) and solved using a standard implementation of the second-order Lax-Wendroff method. A resolution of $\Delta r_* = 0.01$ and $\Delta r = 0.015$ is sufficient to be in the convergence regime. Since standard Sommerfeld outgoing boundary conditions are implemented (see Ref. [124] for improved, non-reflecting boundary conditions), to minimize spurious reflections coming back from boundaries one need to choose radial grids

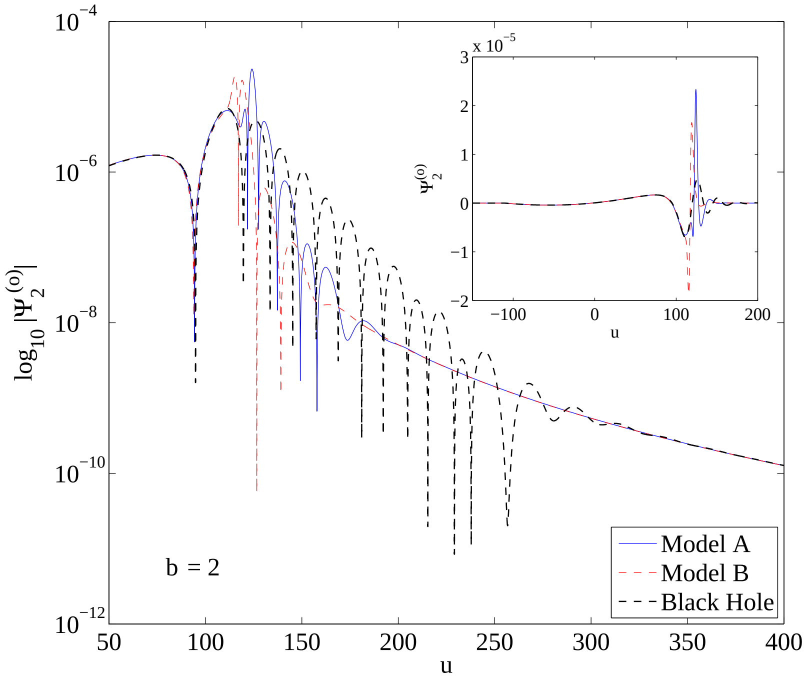

Figure 4.1: Spacetime modes excitation in odd-parity $\ell = 2$ waves from stars models of Tab. 4.1 and a Schwarzschild black hole of the same mass $1.4M_{\odot}$. Dependence of the ring-down phase on the width b of the initial Gaussian pulse: for $b = 2$ the process of excitation of the space-time modes shows the same qualitative features for the black hole and for the stars.

sufficiently extended. In this case $r_* \in [-2000, 2000]$ and $r \in [0, 2000]$ are sufficient to avoid that this effect contaminates the late-time tails of the signals (see Fig. 4.1). The initial Gaussian is centered at $r_c = 100$; the waveforms are extracted at $r = 900$ ($r_* = 916$) and shown versus observer retarded time $u = t - r_*$.

The $\ell = 2$ waveforms (we omit the index $m = 0$) are exhibited, for Model A, Model B and the Black Hole, for $b = 2$ (Fig. 4.1), $b = 8$ (Fig. 4.2) and $b = 20$ (Fig. 4.3). The main panel depicts the modulus on a logarithmic scale, in order to highlight the late-time non-oscillatory tail. Let us first discuss the main features of the signal of Fig. 4.1, *i.e.* starting with the “narrow”pulse, $b = 2$. In the case of the Black Hole, the ring-down has the “standard” shape dominated by the fundamental mode that is quoted in textbooks. In the case of the stars, a damped harmonic oscillations due to w-modes appears (we shall make this statement more precise below). The waveforms show the common “global” behavior *precursor - burst - ring-down - tail* [75]. The precursor is determined by the choice of initial data and by the long-range features of the potential; this implies that, until $u \simeq 100$, the three waveforms are superposed. At later

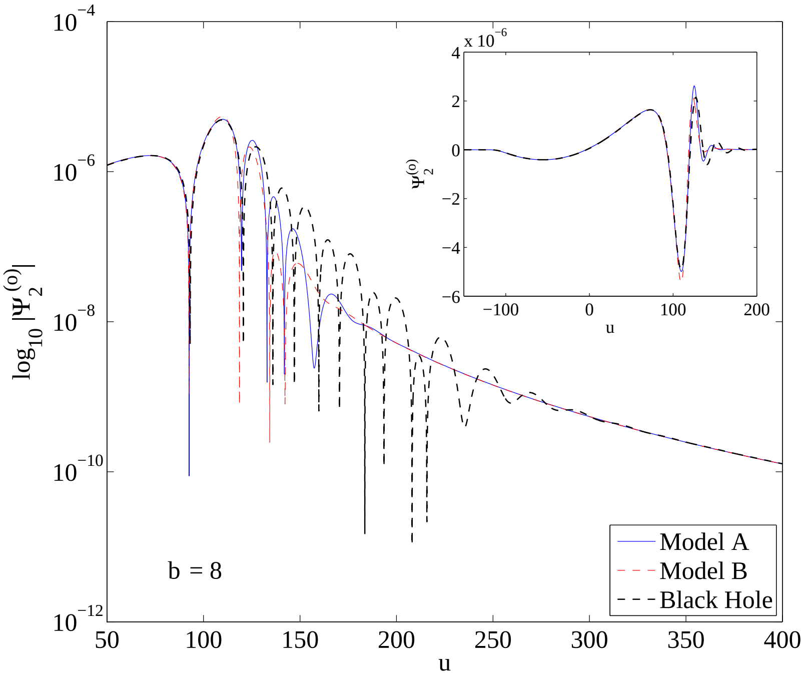

Figure 4.2: Spacetime modes excitation in odd-parity $\ell = 2$ waves from stars models of Tab. 4.1 and a Schwarzschild black hole of the same mass $1.4M_\odot$. Dependence of the ring-down phase on the width b of the initial Gaussian pulse: for $b = 8$ the process of excitation of the space-time modes shows the same qualitative features for the black hole and for the stars.

times, the short-range structure (burst-ring-down) becomes apparent. For the Black Hole the burst is related to the pulse passing through the peak of Regge-Wheeler potential. After the pulse the quasi-harmonic oscillatory regime shows up. When b is increased ($b = 8$, see Fig. 4.2), the features remain unchanged, but, although the non-oscillatory tail is not dominating yet, the amplitude of the damped oscillation is smaller and lasting for a shorter time. A further enlargement of the Gaussian causes the in-going pulse to be almost completely reflected back by the “tail” of the potential, so that the emerging waveform is unaffected by the properties of the central object. Fig. 4.3 highlights this effect for $b = 20$: no quasi-normal oscillations are present. It turns out that the waveforms are perfectly superposed and any characteristic signature of the Black Hole or of the star (for any star model, see below) disappears. We have checked through a linear fit that the tail is asymptotically in perfect agreement with the Price law: $t^{-2\ell+3}$ [164, 165].

The absence of QNMs for large values of b is qualitatively explained by means of the following argument (see also Sec. IX of Ref. [10]): in the frequency domain, the Gaussian perturbation Eq. (3.3.2) equivalent to a Gaussian of variance $\sigma_\omega = \sqrt{2}/b$ and contains all frequencies. However this means that the amplitudes of

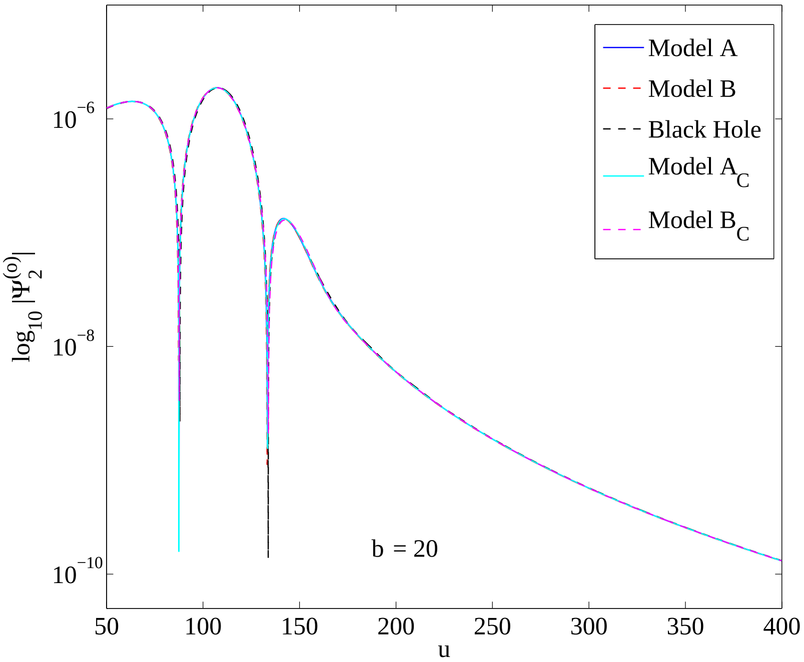

Figure 4.3: Spacetime modes excitation in odd-parity $\ell = 2$ waves from stars models of Tab. 4.1 and a Schwarzschild black hole of the same mass $1.4M_\odot$. Dependence of the ring-down phase on the width b of the initial Gaussian pulse: for $b = 20$ there are basically no difference between the gravitational wave signal backscattered from the stars and from the Black Hole.

the modes excited by this kind of initial data will be exponentially suppressed if their frequencies are greater than the one corresponding to three standard deviations, *i.e.* if their frequency is greater than a sort of "effective maximum frequency" given by $\omega^b_{\max} \simeq 3\sigma_\omega = 3\sqrt{2}/b$. Generally speaking, we expect to trigger the space-time modes of the star (or of the Black Hole) only when b is such that $\omega^b_{\max}$ is *larger* than the frequency of the least damped quasi-normal mode of the system. In order to show how this argument works, let us note that we have $\omega^2_{\max} \simeq 2.12$, $\omega^8_{\max} \simeq 0.53$, $\omega^{14}_{\max} \simeq 0.30$ and $\omega^{20}_{\max} \simeq 0.21$. Tab. 4.2 lists the first six w-modes [1] of Model A (for $\ell = 2$): since the lowest frequency mode has $\omega_{02} \simeq 0.29$, it immediately follows that for $b \gtrsim 14$ the w-mode frequencies can't be found in the Fourier spectrum. This argument is confirmed by the analysis of the energy spectra, that are depicted in Fig. 4.4. The frequency distribution is consistent with the value $\omega^b_{\max} \simeq 3\sqrt{2}/b$ and thus the w-modes can be excited only for $b \lesssim 14.4$. Note that the different amplitudes of the spectra in Fig. 4.4 are due to the convention used for the normalization of the initial data.

---

[1] These numbers have been computed by a frequency domain code whose characteristics and performances are described in Refs. [159, 99, 41, 100].

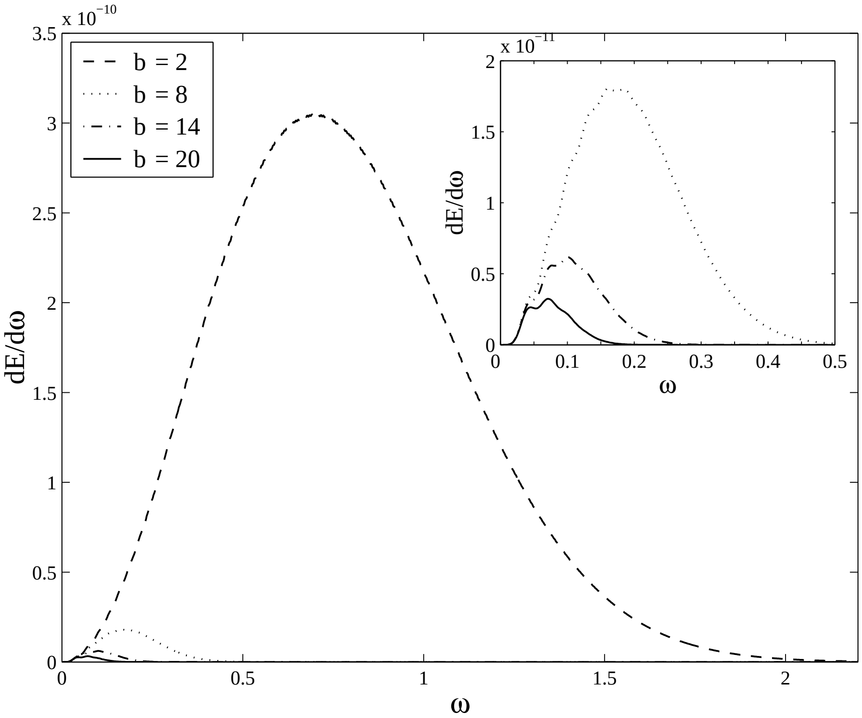

Figure 4.4: Energy spectra of the $\ell = 2$ odd-parity waveforms of Model A for different values of b. The maximum frequency is consistent with $\omega_{\rm max} \simeq 3\sqrt{2}/b$. See text for discussion.

The same argument holds for the Black Hole. Since we have $M = 1.4$ the fundamental QNMs frequency is 0.2669 (See Tab. 4.3 built from Table 1 of [115]); as a result, one must have $b \lesssim 15.9$ to trigger the fundamental mode (that dominates the signal) although the overtones (that have lower frequencies) can already be present in the waveform. In any case, $\omega^2_{\rm max}$ is smaller than the fourth overtone only and, due to the correspondingly large damping time, this is not expected to give a recognizable signature in the waveform.

On the basis of these considerations, we can summarize our results by saying that, for these $M = 1.4M_\odot$ models, when $b \gtrsim 16$, the incoming pulse is totally unaffected by the short-range structure of the object and the signals backscattered by any of the stars and by the Black Hole are identical in practice. This information, deduced by inspecting the waveforms, can be synthesized by comparing, as a function of b and for a fixed ℓ, the energy released by the star ($E_{\rm NS}$) and by the Black Hole ($E_{\rm BH}$) computed from Eq. (3.2.17). Fig. 4.5 exhibits the ratio $E_{\rm BH}/E_{\rm NS}$ for $\ell = 2$ and $\ell = 3$ (the latter for Model A only). This quantity decreases with b because (see Ref. [205]) for small b the Black Hole, contrarily to the star, partly absorbs and partly reflects the incoming radiation. On the other hand, the ratio tends to one for $b \gtrsim 16$, in good numerical agreement with the value of the threshold, needed to excite the quasi-normal modes, that we estimated above. Notice that the saturation to one for $\ell = 3$ occurs for values

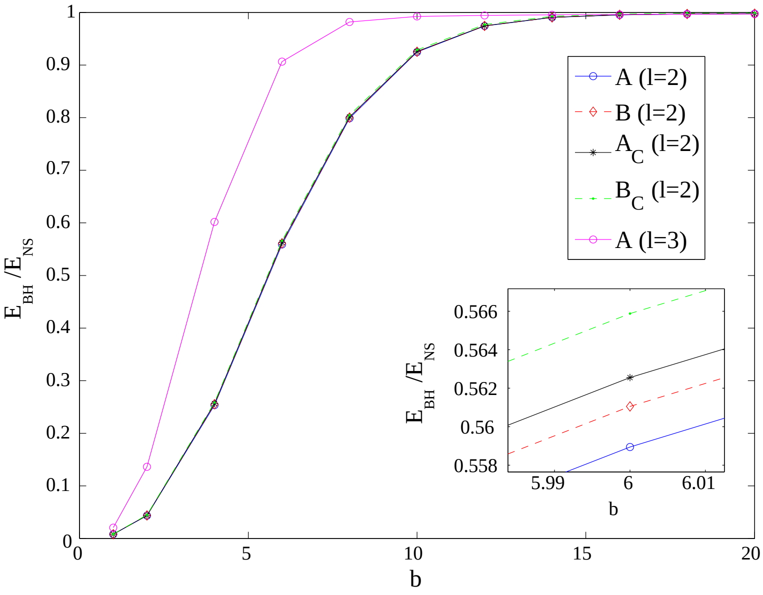

Figure 4.5: The ratio, as a function of b, of the energy released in odd-parity $\ell = 2$ gravitational waves by the Black Hole and different star models.

of b *smaller* than for $\ell = 2$. This is expected: in fact, the QNMs frequencies increase with ℓ and thus one needs narrower b (and thus a larger ω^b_{max}) to trigger space-time vibrations.

We conclude this section by discussing the possibility of identifying "unambiguously" the presence of w-modes in the waveforms and in the corresponding energy spectrum. Ideally, one would like to find precise answers to the following points: (i) Understand which part of the waveform can be written as a superposition of w-modes; (ii) "How many" modes one should expect to be excited and (iii) How does this depend on b.

Although these questions have been widely investigated in the past (see for example Chapter 4 of [93], Ref. [115] and references therein), still they have not been exhaustively answered in the literature. The major conceptual problems underlying this difficulty are (i) The fact that the quasi-normal-modes sets are not complete and (ii) The so called *time shift problem*. The former is intrinsic in the definition of the quasi-normal modes and prevents, in fact, to associate an energy to each excitation mode. The latter is related to the exponential decay of the quasi-normal modes and it implies that, if the same signal occurs at a later time, the magnitudes of the modes will be larger with respect to that of the same signal occurred at an earlier time. As a consequence, the use of the magnitude of the amplitudes A_n (see Eq. (4.1.1)) is not a good measure of the excitation of the quasi-normal modes. We refer to the review of Nollert [147] for a thorough discussion of such problems.

Beside these conceptual difficulties, from the practical point of view it is

Table 4.2: The fundamental and the first three overtones frequencies, ν_{n2}, and damping times, τ_{n2}, of w-modes for $\ell = 2$ of Model A. They have been computed by means of a frequency domain code described in Ref. [159, 99, 41]. The third and fourth column of the table list the corresponding *complex* frequencies $\omega_{n2} - \mathrm{i}\alpha_{n2}$ in dimensionless units. The conversion is given by $\omega_{n2} = 2\pi\nu_{n2}M_{\odot}G/c^3$.

n	ν_{n2} [Hz]	τ_{n2} [μs]	ω_{n2}	α_{n2}
0	9497	32.64	0.29393	0.15091
1	16724	20.65	0.5176	0.23853
2	24277	17.21	0.75136	0.28621
3	32245	15.43	0.99796	0.31923

Table 4.3: The fundamental and the first three overtones of the first four $\ell = 2$ QNMs (complex) frequencies $\omega_{n2} - \mathrm{i}\alpha_{n2}$ of a $M = 1.4$ Black Hole in dimensionless units (Derived from the values published in Table 1 of [115]).

n	ν_{n2} [Hz]	τ_{n2} [μs]	ω_{n2}	α_{n2}
0	8624	77.52	0.2669	0.0635
1	8002	25.18	0.2477	0.1956
2	6948	14.42	0.2150	0.3416
3	5804	9.78	0.1796	0.5037

however important to extract as much as information as possible about the quasi-normal modes by analyzing the ringing phase of the signal. To do so we perform the fit analysis by means of a modified least-square Prony method (see *e.g.* the discussion of Ref. [45]) to fit the waveforms. A feedback on the reliability of our fit procedure is done by comparing the values of frequency and damping time, $\omega_{n\ell}$ and $\alpha_{n\ell}$, obtained by the fit with those of Tab. 4.2 and Tab. 4.3 that we assume to be the correct ones.

The typical outcome of the fit analysis, using only the fundamental mode ($n = 0$), are shown in Fig. 4.6 for the Black Hole with $b = 2$ and in Fig. 4.7 and Fig. 4.8 for the star Model A with $b = 2$ and $b = 8$. When $b = 2$, for which the largest spacetime mode excitation is expected, for both the star and the Black Hole the fits show excellent agreement with the numerical waveform at early times, that progressively worsen due to the power-law tail contribution. The reliability of the procedure is confirmed by the values of ω_{02} and α_{02} that we obtain from the fit. For the Black Hole, we have $\omega_{02} = 0.2660$ and $\alpha_{02} = 0.0631$, which differ of respectively 0.3% and 0.6% from the "exact" values of Tab. 4.3. We can thus conclude that the fundamental mode is essentially the only mode excited for $b = 2$. For the star, Model A, we obtain $\omega_{02} = 0.2739$ and $\alpha_{02} = 0.1636$ and they differ respectively of 7% and 8% from the "exact" values of Tab. 4.2. Since the damping time of the fundamental star w-mode is generically smaller than that of an equal mass black hole, the ringing is shorter and it is more difficult to obtain precise quantitative statements. In this case one could try to include more modes in the template (Eq. (4.1.1)) used for the fit in order to precisely quantify the real contribution due to the presence

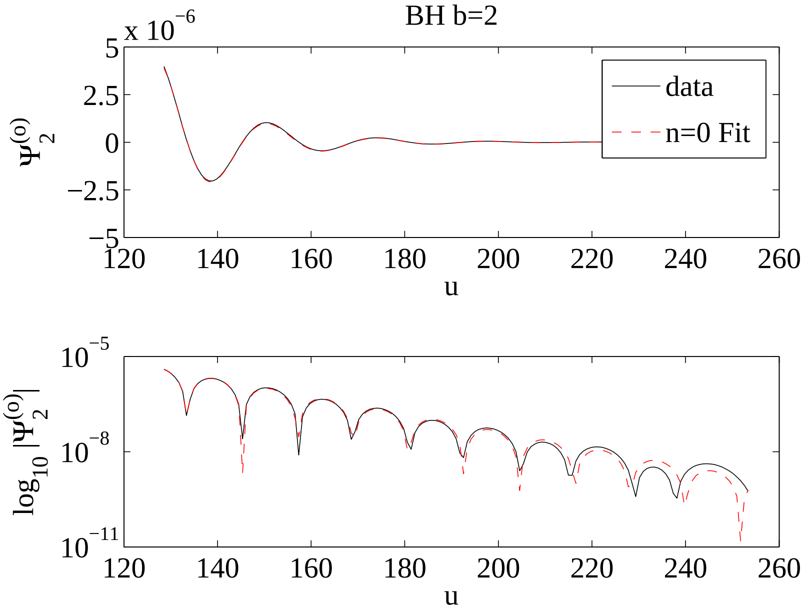

Figure 4.6: Odd-parity $\ell = 2$ waveforms for a Black Hole excited by a $b = 2$ Gaussian pulse: fits of the ring-down part of the waveform with the fundamental ($n = 0$) space-time mode. The waveform $\Psi^{(o)}_{20}(t)$ and its absolute value are showed on a logarithmic scale to highlight the differences with the fit.

of overtones in the signal. Unfortunately, in this like in most of all the cases (See Sec. 4.2.2), the fit procedure is badly conditioned and one could not obtain a sensible feedback of the frequencies even if the global result of the fit (having more adjustable parameters) is better.

The choice of the time window to perform this analysis turns out to have a strong influence on the result of the fit. This choice is delicate and it is related to the aforementioned problem of the time shift. Ideally, the window should start with the ring-down (*i.e.* at the end of the burst) and it must be both sufficiently narrow, in order not to be influenced by the non-oscillatory tail, and sufficiently extended to include all the relevant information. There are no theoretical ways to predict or estimate the correct window, but some systematic procedures have actually been explored in the literature. We decided to use a method very similar to the one discussed in details in Ref. [80]: it consists in setting $u_{\rm f}$ at the end of the oscillatory phase, which is clearly identifiable in a logarithmic plot, and choosing the initial time of the window $u_{\rm i}$ such as to minimize the difference between the real data and the waveform synthesized from the results of the fitting procedure. This difference is estimated by means of Eq. (4.1.2).

Fig. 4.9 shows such a determination for the Black Hole (right panel) and Model A (left panel) with $b = 2$: both curves exhibit a clear minimum of the quantity $\mathcal{R} \equiv 1-\Theta$ at, respectively, $u_{\rm i} = 129$ and $u_{\rm i} = 131$. The time window

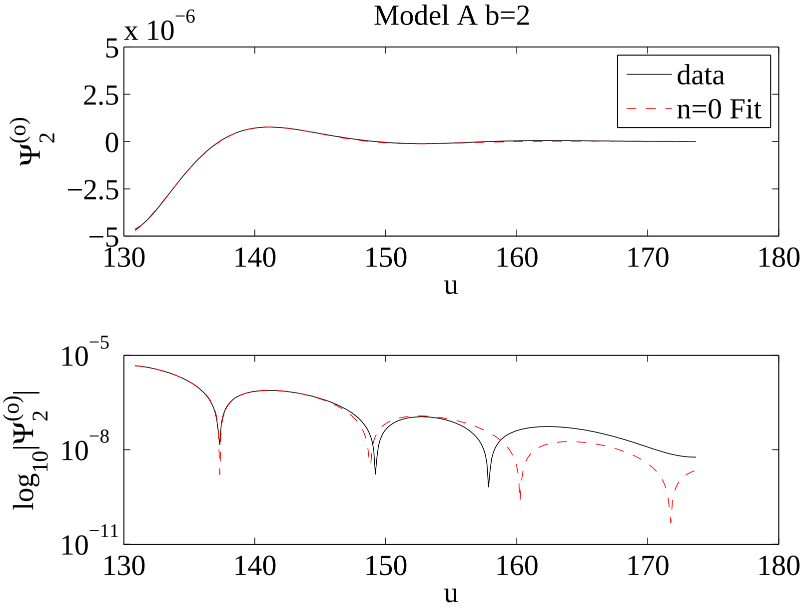

Figure 4.7: Odd-parity $\ell = 2$ waveforms for the stellar Model A excited by a $b = 2$ Gaussian pulse: fits of the ring-down part of the waveform with the fundamental ($n = 0$) space-time mode. The waveform $\Psi^{(o)}_{20}(t)$ and its absolute value are showed on a logarithmic scale to highlight the differences with the fit.

extends to $u_{\rm f} = 254$ (Black Hole) and $u_{\rm f} = 174$ (Model A), respectively. As can be seen in Fig. 4.10 one has that even a small change of initial time $u_{\rm i}$ of the window used produces sensible variation of the estimated values of the frequency and the damping time of the fundamental mode. However, it should be noticed that the estimated values obtained for the best window are those in best agreement with the expected values.

Repeating the analysis for the datasets relative to wider Gaussian pulses and focusing on the representative $b = 8$ case, leads to same picture with two main differences. First, the "global" quality of the fit, given by $\mathcal{R}$ is less good than in the $b = 2$ case; this is particularly evident for the star, where the fitted frequencies differ from the "exact" ones by more than 10%. Second, the fitting window becomes narrower and narrower as b is increased (see column seven of Tab. 4.4), thereby the the fit analysis quickly becomes meaningless.

For the reasons outlined above we have found this procedure not as effective as we hoped. We think that the problem of the unambiguous determination of the "right" time interval for the fit and of the presence and quantification the overtones in numerical data deserves further considerations.

4.2.2 Effect of the compactness

The gravitational wave "scattering experiment" described in the previous section has been repeated for all the star models described by realistic EOS pre-

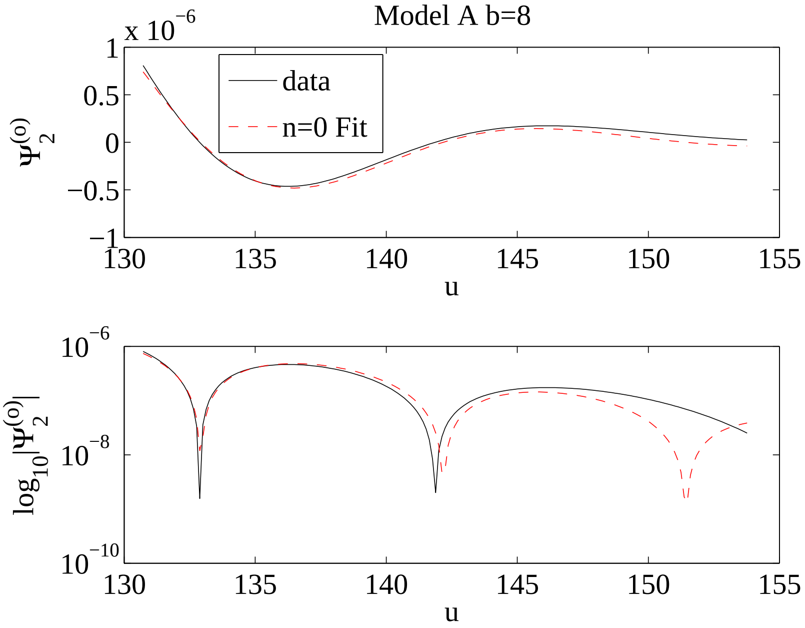

Figure 4.8: Odd-parity $\ell = 2$ waveforms for the stellar Model A excited by a $b = 8$ Gaussian pulse: fits of the ring-down part of the waveform with the fundamental ($n = 0$) space-time mode. The waveform $\Psi^{(\mathrm{o})}_{20}(t)$ and its absolute value are showed on a logarithmic scale to highlight the differences with the fit.

sented in Tab. 2.3. A comparison of the waves of Model A and Model B in Fig. 4.1 suggests that, if the initial perturbation "contains" a frequency sufficiently high to excite w-modes, the compactness of the star is the only relevant parameter in the whole process. This picture in confirmed by the following systematic investigation of the waves from different EOS and compactness.

The simulations we are going to discuss are done with the PERBACCO using a resolution of $J_i = 400$ points, and a Courant-Friedrichs-Lewy factor set to $\Delta t/\Delta r = 0.4$. For each model, the outer boundary of the grid is at $r = 600M$ and the final evolution time is $t^{\mathrm{end}} = 800M$. The Gaussian width is chosen as $b = M$ since the star mass introduces a natural length scale in the system. The amplitude of the perturbation A is chosen equal to 0.01. The waves are extracted at $r = 300M$.

As a representative case, because the global qualitative features are common to all EOS, Fig. 4.23 exhibits the $\ell = 2$ waveforms computed with EOS A. The waveform is characterized by the structure precursor-burst-ringdown-tail described in detail in the previous section for the case of polytropic EOS stars and of black holes. The compactness of the model increases from top to bottom; the left panels exhibit the waveforms on a linear scale, while the right panels their absolute values on a logarithmic scale. Since the damping time increases with the star compactness, the maximum mass model, Amx, presents the longest w-mode ringdown. On the contrary, model A10 exhibits only a one–cycle, small–amplitude ringdown oscillation that quickly disappears in the power-law tail.

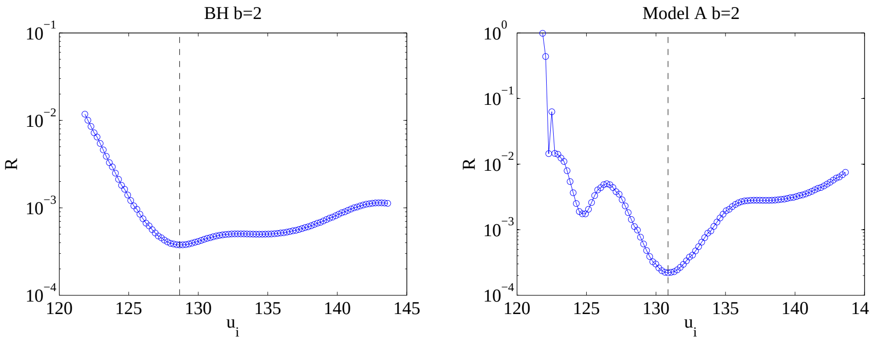

Figure 4.9: The residual $\mathcal{R}$ (See Eq. (4.1.2)) of the fits of the waveform of the response to a $b = 2$ Gaussian pulse of the Black Hole (right panel) and the stellar Model A (left panel) as a function of the initial time ($u_{\rm i}$) of the fitting window around its best values that it is $u_{\rm i} = 129$ for a Black Hole and $u_{\rm i} = 131$ for Model A.

Table 4.4: The results of the fit analysis on the $\ell = 2$ odd-parity waveforms for the Black Hole and for the stellar Model A generated in the response to Gaussian pulse with $b = 2$ and $b = 8$. Only one mode, *i.e.* the fundamental one, is used in the fit. The best fit window $[u_{\rm i}, u_{\rm f}]$ is determined using the minimum of the residual $\mathcal{R}$ criteria (See Fig. 4.9 and Eq. (4.1.2)). The reported errors refer to relative difference between the fitted values and reference values reported in Tab. 4.2 and Tab. 4.3.

Model	b	ω_{02}	$\delta\omega_{02}$ [%]	α_{02}	$\delta\alpha_{02}$ [%]	$[u_{\rm i}, u_{\rm f}]$	$\mathcal{R}$
A	2	0.2739	7	0.1636	8	$[131, 174]$	2×10^{-4}
A	8	0.3396	15	0.1302	13	$[131, 154]$	1×10^{-2}
BH	2	0.2660	0.3	0.0631	0.6	$[129, 254]$	4×10^{-4}
BH	8	0.2614	0.2	0.0591	0.7	$[129, 229]$	$5 \times 10^{q-3}$

Let us focus on model Amx, that presents the longest and clearest ring-down waveform. Using a standard least-squares fit and the same procedure of Sec. 4.2.1 we estimate the frequency of the fundamental w-modes to be $\nu_w^{(\rm o)} = 9452$ Hz, with a damping time $\tau_w^{(\rm o)} \simeq 0.07$ ms. For comparison, we note that a Schwarzschild black hole of the same mass has the fundamental $\ell = 2$ frequency and damping time equal to, respectively, $\nu^{\rm BH} = 7317$ Hz and $\tau^{\rm BH} = 0.09$ ms. The energy spectrum of the waveform, computed starting from $u \sim 170$ (the first zero after the burst), has a single peak centered at a frequency that differs from $\nu_w^{(\rm o)}$ of about a few percents.

However, as discussed in Sec. 4.2.1, we found that this information is in general very difficult to extract, especially for the lowest mass models, due to the rapid damping of the modes and their "localization" in a narrow time window. The errors in this computation are estimated comparing our results with those of Ref. [14] where a frequency domain approach is employed. The comparison with frequency domain data (See Tab. 4.4 and Tab. 4.6) shows that the errors on the numbers presented above are of the order of 5%. The error on the frequencies increases up to about 12% for models with $M \sim 1.4$ and to

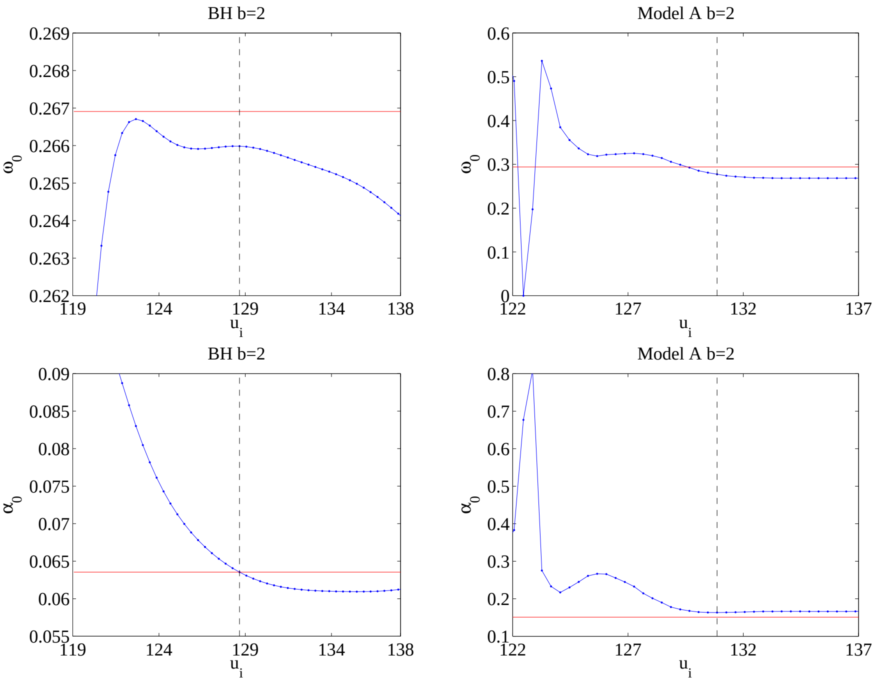

Figure 4.10: Determination of the best window for the fit of the Black Hole waveform and Model A ($b = 2$). The initial time $u_{\rm i}$ is chosen so to minimize the residual $\mathcal{R}$ between the data and the fit. The picture show the frequency and the inverse of the damping time as a function of the initial time. As a best fit value for the Black Hole we obtain $u_{\rm i} = 129$ ($u_{\rm f} = 254$), while for Model A we have $u_{\rm i} = 131$ ($u_{\rm f} = 174$). The horizontal line indicates the "exact" values of the considered model reported in Tab. 4.2 and Tab. 4.3.

about 20% for models with smaller mass. Moreover, the damping times can not be reliably estimated with a fit procedure when they are too short.

In summary, although the extraction of the proper frequencies from odd-parity waveforms through a fit procedure works for some particular models, in general it seems uncapable to give numbers as robust and reliable as those provided by a standard frequency domain approach. See for example Ref. [41] for details about this approach.

4.3 Even-parity waves

Even-parity waveforms from linearly oscillating NS are characterized by a mixture of fluid modes, which are related to stellar fluid pulsations and have a Newtonian counterpart, and curvature modes. Former studies [6, 169, 139] showed that for various kinds of initial data, both fluid and spacetime modes are present, but they have different relative amplitudes depending on the initial excitation of the system. In particular the presence of spacetime modes can be almost totally suppressed using conformally flat initial data, while scattering-like initial data lead, generically, to the clearest contribute of spacetime modes in the waveforms.

All the previous studies use a simplified description of the internal composition of the star, *i.e.* a polytropic EOS with adiabatic exponent $\Gamma = 2$. In addition Ref. [169] explored also the use of one realistic EOS. The author found a numerical instability related to the dip in the sound speed at neutron drip point. This instability was independent either of the formulation of the equations or of the numerical (finite differencing) scheme used. The use of a particular radial coordinate was proposed to cure the problem.

Here we reexamine the problem of the evolution of the perturbation equations for relativistic stars investigating systematically the gravitational radiation emitted from the oscillations of non-rotating neutron star models described by a large sample of realistic EOS. As we will see the constrained algorithm implemented in the PerBaCCo permits long-term and stable simulations and it is free from the problems of Ref. [169]. For each model of Tab. 2.3, we numerically evolve the initial data presented in Sec. 3.3.1 for the even-parity perturbations as described in Sec. 3.2 using the PerBaCCo (Sec. 3.3). In the following two Sections we will discuss the results obtained focusing on the $\ell = 2$ multipole (the quadrupole), as this is the principal responsible of the gravitational wave emission. The waves are extracted at different radii, $r = \{50,\ 100,\ 200,\ 300\}M$. We checked the convergence of the waves and the differences between the extraction at $r = 200M$ and $r = 300M$ are very small, so that we can infer to be sufficiently far away from the source (See also Sec. 4.3.3). The gravitational waveforms we discuss in the following have always been extracted at the farthest observer, $r = 300M$ and they are plotted versus observer's retarded time $u = t - r_*$. The simulations require a resolutions of $J_i = 800$ and the Courant-Friedrichs-Lewy factor is set to $\Delta t/\Delta r = 0.4$. For each model, the outer boundary of the grid is at $r = 600M$ and the final evolution time is $t^{\rm end} = 3000M$. The amplitude of the perturbation A is everywhere chosen equal to 0.01.

The last Section is devoted to a detailed analysis of the waveform obtained from an accurate and long evolution of type 1 initial data. The waveform is characterized only by fluid modes only for which we obtain also the damping times. These results will be used to contrast with results from nonlinear simulations.

4.3.1 Waveforms from different ID

Let's start presenting together waveforms generated by conformally flat (type 1) and radiative (or non-conformally flat, type 2) initial data. Former studies with polytropic EOS [169, 139] showed that initial data of type 1 determine the excitation of fluid modes only. On the contrary, initial data of type 2 produce a gravitational wave signal where both spacetime and fluid modes are present. As expected, this qualitative picture is confirmed also for realistic EOS. Fig. 4.11 exhibits the waveform $\Psi^{(\rm e)}_{20}$ for the representative model WFF14. For conformally flat initial data (solid line) the figure shows that the Zerilli-Moncrief function oscillates at (mainly) one frequency, of the order of the kHz. The corresponding energy spectrum (solid line in Fig. 4.12) reveals that the signal is in fact dominated by the frequency $\nu_f = 2126$ Hz, but there is also a second peak at $\nu_p = 6909$ Hz. This two frequencies are recognized as those of the fundamental fluid mode f and of the first (pressure) p-mode.

For non-conformally flat initial data (dashed line in Fig. 4.11) the first part

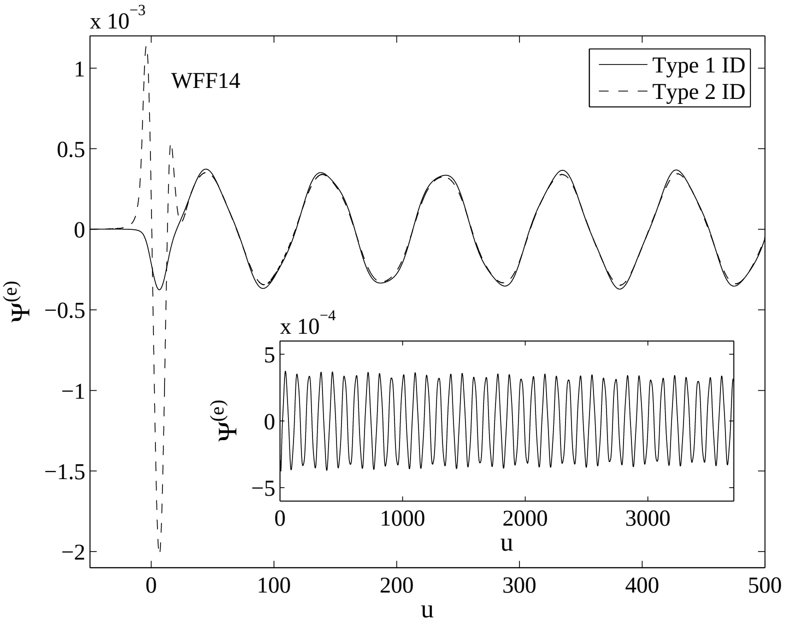

Figure 4.11: Even-parity waveforms for model WFF14 generated by initial data of type 1 (solid line) and type 2 (dashed line). In the first case, only fluid modes (the f-mode and the first p-mode) are present; in the second case, w-mode oscillations are present at early times ($0 \lesssim u \lesssim 50$). The inset shows long-term evolution (corresponding to a total time of ~ 20 ms) used to compute the energy spectrum of Fig. 4.12.

of the signal, *i.e.* $0 \lesssim u \lesssim 50$, is dominated by a high-frequency and strongly-damped oscillation typical of curvature modes. For $u \gtrsim 50$, the type 1 and type 2 waveforms are practically superposed. The corresponding energy spectrum (dashed line in Fig. 4.12) has, superposed to the two narrow peaks of the fluid modes, a wide peak centered at higher frequency (~ 11 kHz) that is typical of the presence of spacetime excitation [115] [2] .

The information of Fig. 4.12 is complemented by the Fourier spectrum of the metric variable S in Fig. 4.13. In contrast to the fluid variable H, which contains only narrow peaks for both kind of initial data, for type 2 waveforms the metric variable S also exhibits a broad peak which is absent for type 1 initial data. Note, that the picture that we have discussed so far for model WFF14 remains qualitatively unchanged for all the other EOS.

Finally we discuss now the waveforms generated by initial data of type 3. This kind of "scattering-type" initial condition constitutes the even-parity analogue of that discussed in Sec. 4.2 for the odd-parity case. In Fig. 4.14 we show the $\Psi^{(e)}_{20}$ waveforms from 3 models of EOS WFF. The waveforms in the

---

[2] Note that, in order to obtain the cleanest fluid-mode peaks, in the Fourier transform of type 1 waveform we discarded the first four GW cycles, which are contaminated by a transient due to the initial excitation of the system. On the other hand, for type 2 waveform, we considered the full time-series. In this case, it is not possible to cut the first part of the signal because it also contains the curvature mode contribution that we want to analyze.

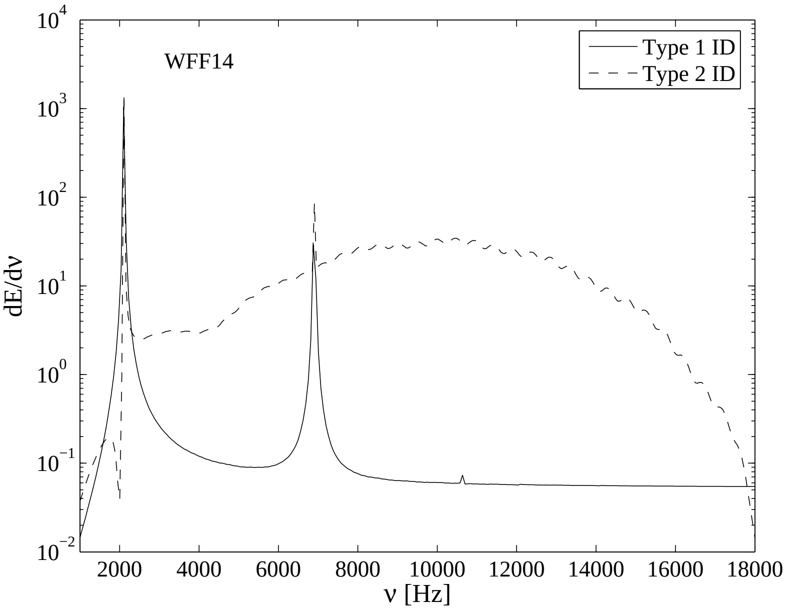

Figure 4.12: Energy spectra of the type 1 (solid line) and type 2 (dashed line) initial data evolution of Fig. 4.11. The two narrow peaks at 2126 Hz and 6909 Hz correspond to the f-mode and the first p-mode frequencies. The wide peak at $\simeq$ 11 kHz corresponds to w-mode excitation.

top panel of the figure are very similar to those of the left panels of Fig. 4.23. The logarithmic scale (bottom panel) highlights the main qualitative difference: *i.e.* fluid-mode oscillations are present, in place of the non-oscillatory tail, after the w-mode ringdown. Note that, in principle, the tail will emerge in the signal after that all the fluid modes have damped (*i.e.* on a time scale of a few seconds).

The process of w-mode excitation is instead exactly the same as for the odd parity case: the ringdown phase is longer (and thus clearly visible) for the more compact models. The frequencies are also very similar. For example, for model WFFmx (the one discussed in the figure) we have $\nu_w^{(\mathrm{e})} = 8638$ Hz and a damping time $\tau_w^{(\mathrm{e})} \simeq 0.05$ ms, while for model Amx $\nu_w^{(\mathrm{e})} = 9798$ Hz and $\tau_w^{(\mathrm{e})} \simeq 0.05$ ms (to be compared with $\nu_w^{(\mathrm{o})} = 9452$ and $\tau_w^{(\mathrm{o})} \simeq 0.07$ ms).

4.3.2 Effect of the EOS

Since the numerical scheme of the PerBaCCo allows to evolve the system in time as long as one wish (See *e.g.* Sec. 4.3.3), we produced simulations of about 30 ms to accurately extract, via Fourier analysis, the fluid mode frequencies. In addition we performed a fit analysis with a one-mode ($N = 1$) QNMs template (Eq. (4.1.1)) and we extracted also the damping times from the waveform. The choice of $N = 1$ is due to the fact that, to capture in the fit the simulations the first p-mode, one needs considerably longer time-series (See Sec. 4.3.3).

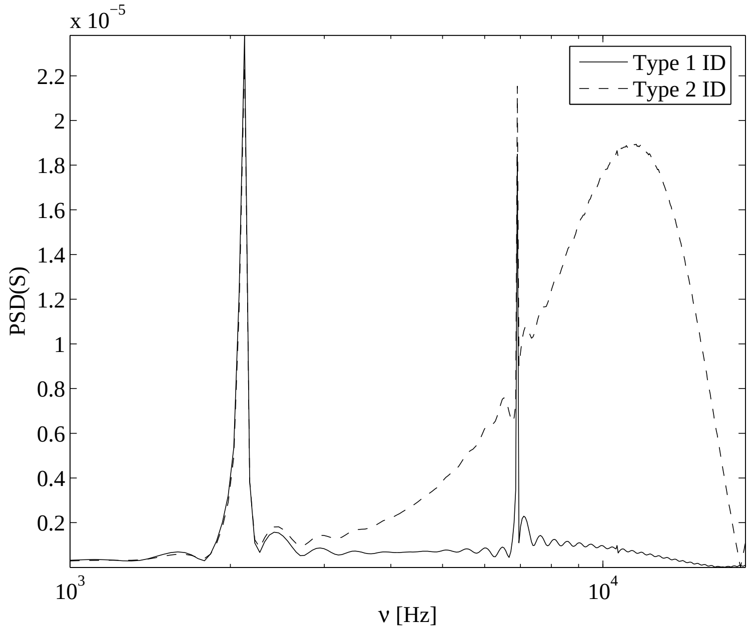

Figure 4.13: Power spectrum of the variable S for model WFF14 in the case of initial data of type 1 and 2.

The results of the analysis for all the models considered are reported in Tab. 4.8. For a fixed EOS, the frequencies increase with the star compactness. For a model of given mass, the f-mode frequency generally decreases if the EOS stiffens. The same (on average) is true for the first p-mode frequency. The frequencies computed via the energy spectra consistently agree with those computed via the fit analysis. Damping times generically decrease with the star compactness as already noted.

Following Ref. [14, 42], we present in Fig. 4.15, Fig. 4.16 and Fig. 4.17 the results in a form that highlights functional relations involving the star parameter. From general considerations it is, in fact, possible to establish empirical relations relating frequencies and damping times with the star mass and radius. In particular the f-mode frequencies are almost a linear function of the mean density $\sqrt{M/R^3}$ of the star, while the p-mode frequencies multiplied by M can be linearly fitted with the star compactness M/R. The f-mode damping time is roughly proportional to the oscillation energy divided by the power emitted in GWs, and this give the functional relation in Fig. 4.17. In principle a detection of a GW signal from an oscillating NS could constraint the value of mass and radius and infer the EOS from the GW experimental data.

To validate the physical results of the PerBaCCo we compare the frequencies extracted from our simulations with values computed via a frequency domain approach. In the case of the polytropic EOS, the results reported in Ref. [140] showed that the errors on fluid frequencies are less than 1%. Spacetime frequencies for polytropic EOS models are checked as discussed in Sec. 4.2. In this

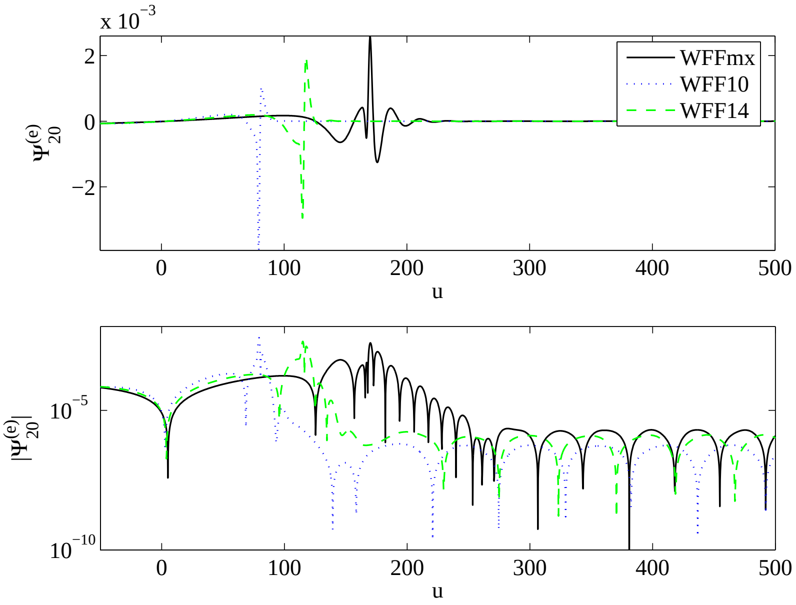

Figure 4.14: Excitation of even-parity w-modes for some WFF models from given initial data of type 3. As in the odd-parity case (compare with Fig. 4.23), the ringdown is more pronounced for more compact models.

case, when the damping times are sufficiently long (*i.e.* when a narrow Gaussian pulse is used and the star model is very compact), it is possibile to estimate ν and τ using a fit procedure, with an error of the order of 6%, see Tab. 4.4.

The accuracy of the frequencies does not change when we use realistic EOS. To validate this assertion, we compared the frequencies extracted from our waveforms with those of Andersson and Kokkotas [14] for EOS A with mass $M = 1.653$, $M = 1.447$ and $M = 1.050$ (See Table A.1 of Ref. [14]). Our results are listed in Tab. 4.5 and Tab. 4.6, together with the data of [14] for completeness. Both method (Fourier and fit) were used for the analysis and gave consistent results within few percents. In the latter case, in particular, the fits were performed with only one mode, $N = 1$. Fluid frequencies are typically captured with an accuracy below 1%, while spacetime frequencies and damping times can be estimate with decent accuracy (5%) only for the maximum mass model. As a consequence, we expect that a similar accuracy for fluid modes, *i.e.* of the order of 1%, should be expected for the 47 NS models of Tab. 2.3.

4.3.3 Detailed analysis of type 1 waveforms

In this last Section we focus on the waveforms emitted from an oscillating star excited with conformally flat initial data. Initial data are described in detail in Sec. 6.3, but they are a simple variation of type 1 initial already discussed. The star is described by the model A0 (See Tab. 6.1, or AU0 in Tab. 2.2): a polytropic EOS of type $p = K\rho^{\Gamma}$ with $K = 100$, $\Gamma = 2$ and $\rho_c = 1.28 \times$

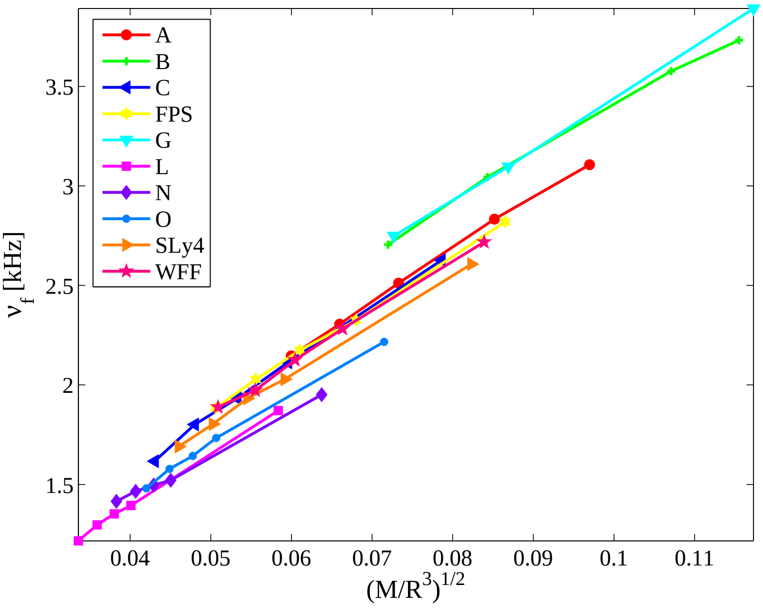

Figure 4.15: Frequencies of the $\ell = 2$ fundamental fluid modes for different EOS. The f-mode frequencies is showed as a function of $\sqrt{M/R^3}$.

10^{-3}. We give in the following a detailed "identikit" of this kind of wave that will serves as a starting point to compare with nonlinear simulations described in Chap. 6. The data we are presenting comes from very long simulations by the PERBACCO : the final time is about 1 s. The full waveforms is plotted in Fig. 4.18. The extraction radii for the Zerilli-Moncrief function extend as far as $\bar{r} = 420$ ($\simeq 300M$, we will use in this section also the isotropic radius to facilitate then the comparison with nonlinear results). The resolution of the radial grid is $\Delta r = 0.032$, which corresponds to $J_i = 300$ points inside the star.

Fig. 4.19 shows the Zerilli-Moncrief function $\Psi^{(\rm e)}_{20}$ extracted at different radii. It is plotted versus the observer retarded time and showed at different radii. The farther observers that are shown in the figure are sufficiently deep in the wave-zone that the initial offset, that is typically present due to the initial profile of k_{20}, see *e.g.* Fig. 6.3, is small enough to be considered negligible. We checked the convergence of the waves with the extraction radius using as a reference point the maximum of $\Psi^{(\rm e)}_{20}$. This point can be accurately fitted, as a function of the extraction radius, with

$$\max\left(\Psi^{(\rm e)}_{20}\right) \simeq a^{\infty} + \frac{a^1}{r} \,. \tag{4.3.1}$$

The extrapolated quantity a^{∞} allows an estimate of the error related to the extraction at finite distance

$$\delta a \equiv \frac{\left|a^{\infty} - \max\left(\Psi^{(\rm e)}_{20}(r)\right)\right|}{a^{\infty}} \,. \tag{4.3.2}$$

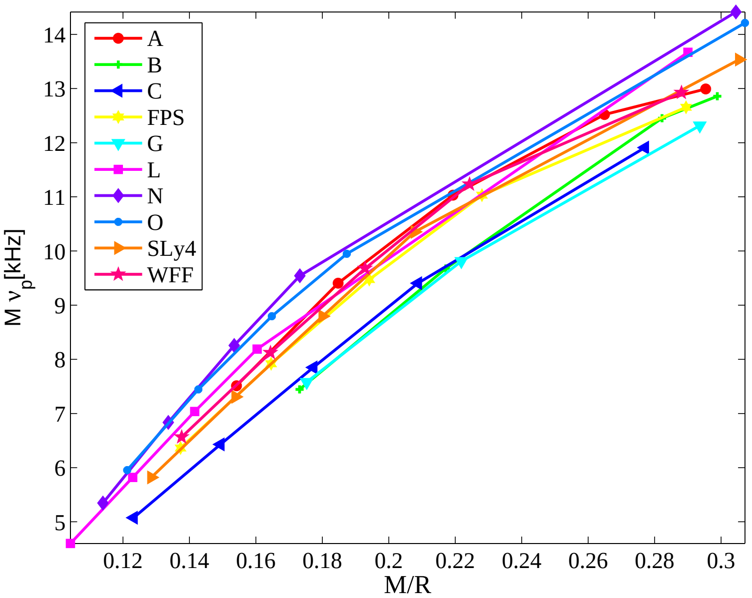

Figure 4.16: Frequencies of the $\ell = 2$ first pressure modes for different EOS. The first p-mode frequency (multiplied by the mass M) is showed as a function of the compactness M/R.

The values of δa for different radii are $\delta a \simeq 0.5$ for $r = 25M$, $\delta a \simeq 0.09$ for $r = 50M$, $\delta a \simeq 0.017$ for $r = 100M$ and $\delta a < 0.016$ for $r > 200M$. Indeed, the difference in amplitude of a wave extracted a $r > 200M$ with respect to a wave extracted (properly) at infinity can be estimated to be of the order of less than 2%, frequency are not affected (in the system under investigation) by finite extraction effects.

The waveform can be described by two different phases: (i) An initial transient, of about half a gravitational-wave cycle, say up to $u \simeq 50$, related to the setup of the initial data [3], followed by (ii) A quasi-harmonic oscillatory phase, where the matter dynamics is described in terms of the stellar quasi-normal modes. From the Fourier spectrum of $\Psi^{(\mathrm{e})}_{20}$ over a time interval from 1 to about 30 ms (namely $u \in [50, 6000]$), we found that the signal in Fig. 4.18 is dominated by the f-mode (at frequency $\nu_f = 1581$ Hz) with a much lower contribution of the first p-mode (at frequency around $\nu_{p_1} = 3724$ Hz). The frequency of the f-mode agrees with that of Ref. [90] within $1-2\%$. The accuracy of the PerBaCCo for these frequencies obtained from Fourier analysis on such long time series has been checked in Ref. [140] and Sec. 4.3.2 and is better

---

[3] In practice, the first half cycle of the waves cannot be expressed as a superposition of quasi-normal modes and it is related to the initial data setup. This initial transient is related to two facts: (i) That we use the conformally flat approximation; (ii) That we assume $\dot{k}_{\ell m} = 0$ even if our initial configuration (a star plus a non-static perturbation) is evidently not time symmetric, since a velocity perturbation is present and thus also a radiative field related to the past evolutionary history of the star.

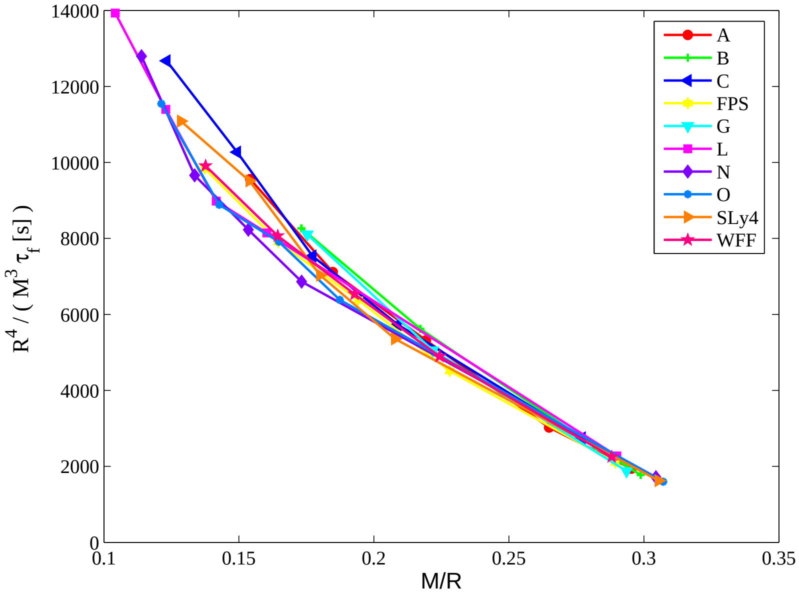

Figure 4.17: Frequencies of the $\ell = 2$ first pressure modes for different EOS. The first p-mode frequency (multiplied by the mass M) is showed as a function of the compactness M/R.

than 1% on average. We mention that the Fourier analysis of the matter enthalpy variable H permits to capture some higher overtones than the p_1 mode, although they are essentially not visible in the gravitational-wave spectrum.

On the interval $u \in [50, 6000]$, the waves can be perfectly represented by a one-mode expansion, $N = 1$ in Eq. (4.1.1), as the waveform is dominated by f-mode oscillations. The frequency we obtain by the fit analysis, $\nu_{20} = 1580.79 \pm 0.01$ Hz, is perfectly consistent with that obtained via Fourier analysis; for the damping time, we estimate $\alpha_{02} = 3.984 \pm 0.066\,\text{sec}^{-1}$ and thus $\tau_{02} = \alpha_{02}^{-1} \simeq 0.25$ s. As a "goodness" indexes of the fit we found $\mathcal{R} \simeq 7 \times 10^{-4}$, and $\mathcal{D} \simeq 6 \times 10^{-6}$ (See Eq. (4.1.2) and Eq. (4.1.3)).

If we consider however the entire duration (1 s) of the signal (See the insets in Fig. 4.18), it is clear that a one-mode expansion is not sufficient to accurately reproduce the waveform. The Fourier analysis of the waveform in two different time intervals, see the panels in the middle of Fig. 4.22, one for $t \lesssim 0.5$ s and one for $t \gtrsim 0.5$, reveals that in the second part of the signal the p_1-mode, which has longer damping time, clearly emerges and must be taken into account. The entire signal can be fitted with two modes, namely $N = 2$, with a global agreement of $\mathcal{R} \simeq 2 \times 10^{-6}$ and $\mathcal{D} \simeq 4 \times 10^{-5}$. The bottom panels of Fig. 4.22 highlights the accuracy of the fit also at a visual inspection. The results of the fit are reported in Tab. 4.7. The frequencies seem a little overestimated with respect to those computed via Fourier analysis and via the fit procedure restricted to only one mode on a shorter interval. They are, however, still consistent. Par-

Table 4.5: Frequencies ν of fluid modes (f and p) of some models of Andersson and Kokkotas [14], described by EOS A, computed from perturbative waveforms via Fourier analysis. The frequencies are expressed in Hz. For the sake of comparison, we report also the values of their Table A.1 with the "AK" superscript.

M	ν_f	ν_f^{AK}	Diff. [%]	ν_p	ν_p^{AK}	Diff. [%]
1.653	3080	3090	0.3	7825	7838	0.2
1.447	2580	2579	0.04	7843	7818	0.3
1.050	2183	2203	0.9	7555	7543	0.2

Table 4.6: Frequencies ν and damping times τ of fluid (f) and spacetime (w) modes of some models of Andersson and Kokkotas [14], described by EOS A, computed from perturbative waveforms via the fit analysis. The frequencies are expressed in Hz and the damping times in ms.

M	ν_f	τ_f	ν_w	τ_w
1.653	3046.26^{+2}_{-2}	112^{+2}_{-2}	9341.97^{+4}_{-4}	0.06251^{+9}_{-9}
1.447	2573.54^{+2}_{-2}	122^{+2}_{-2}	1108.3^{+4}_{-4}	0.15^{+4}_{-8}
1.050	2201.94^{+1}_{-1}	186^{+2}_{-2}	11266.9^{+2}_{-2}	0.059^{+4}_{-5}

ticularly significant is the capability to obtain, from the simulations and the analysis, quite accurate results for the damping times. They are $\tau_{02} = 0.268$ s and $\tau_{12} = 2.37$ s, with errors respectively of the order of 0.1% and 2%.

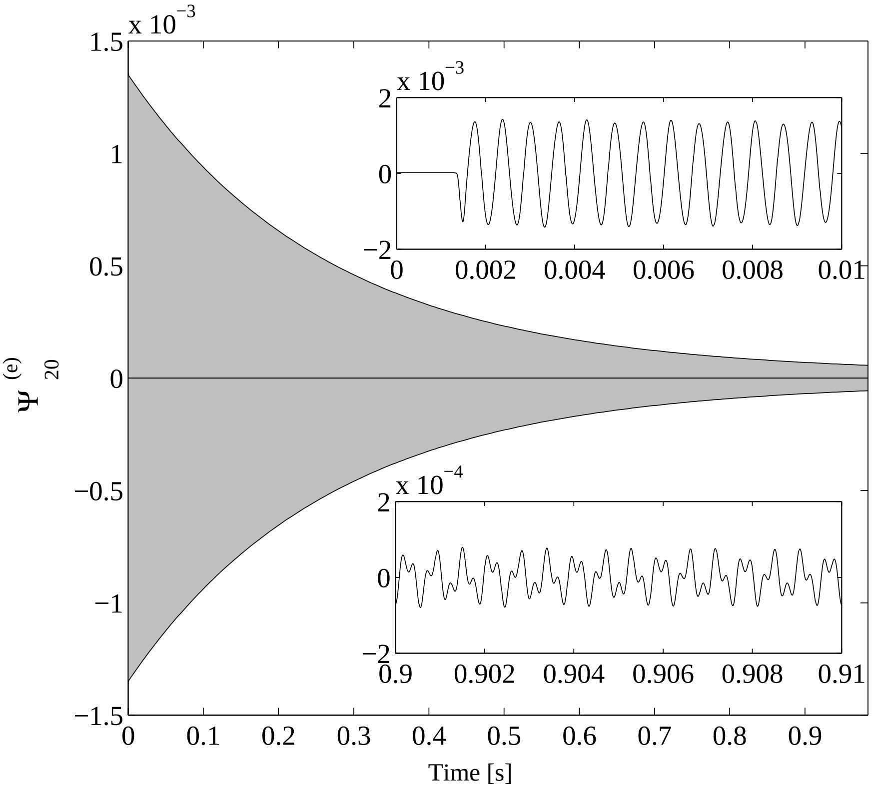

Figure 4.18: The Zerilli-Moncrief function, extracted at the isotropic radius $\bar{r} = 280$ (80M) versus the observer retarded time u expressed in seconds. The main panel shows only the envelope of the waveform, that is dominated by the damping time of the f-mode ($\tau_f \simeq 0.27$ s). The two insets represent the full waveform at early (top) and late (bottom) times. The presence of the overtone is evident in the oscillations at late times. This simulation is performed with the PerBaCCo evolving the same initial data used in 3D simulation and described in Sec. 6.3 with $\lambda = \lambda 1$.

Table 4.7: Results of the fit analysis on even-parity $\ell = 2$ perturbative waveforms for the model A0. Initial data are conformally flat initial data with $\lambda = \lambda 1$ described in Sec. 6.3. The waveforms is showed in Fig. 4.19. The fit is performed using a superposition of two fluid modes ($N = 2$ see Eq. (4.1.1)) over the interval $u \in [0, 200000]$, *i.e.* about 1 s. For this fit, $\mathcal{R} \simeq 1.6 \times 10^{-6}$ and $\mathcal{D} \simeq 3.6 \times 10^{-5}$ (See text for explanations).

$A_{n\ell}$ [a.u.]	$\nu_{n\ell}$ [Hz]	$\alpha_{n\ell}$ [s^{-1}]
A_{02}=$1.3145^{+2}_{-2} \times 10^{-3}$	ν_{02}=1583.7369^{+2}_{-1}	α_{02}=3.7358^{+9}_{-9}
A_{12}=$3.517^{+13}_{-12} \times 10^{-5}$	ν_{12}=3706.9413^{+11}_{-11}	α_{12}=0.421^{+8}_{-6}

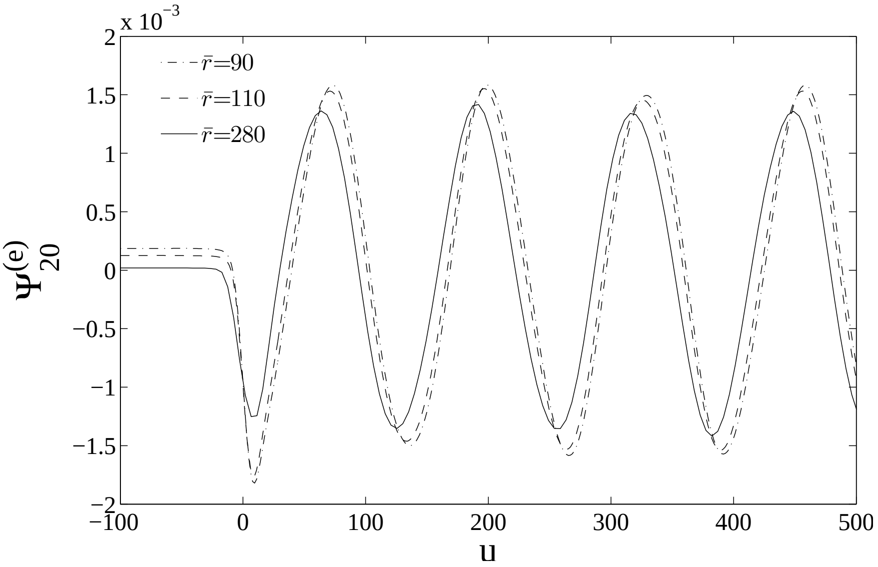

Figure 4.19: The Zerilli-Moncrief function, extracted at various isotropic radii $\bar{r}$, versus the observer retarded time u. This simulation is performed with the PerBaCCo evolving the same initial data used in 3D simulation and described in Sec. 6.3 with $\lambda = \lambda 1$. Note how the initial offset decreases with the extraction radius.

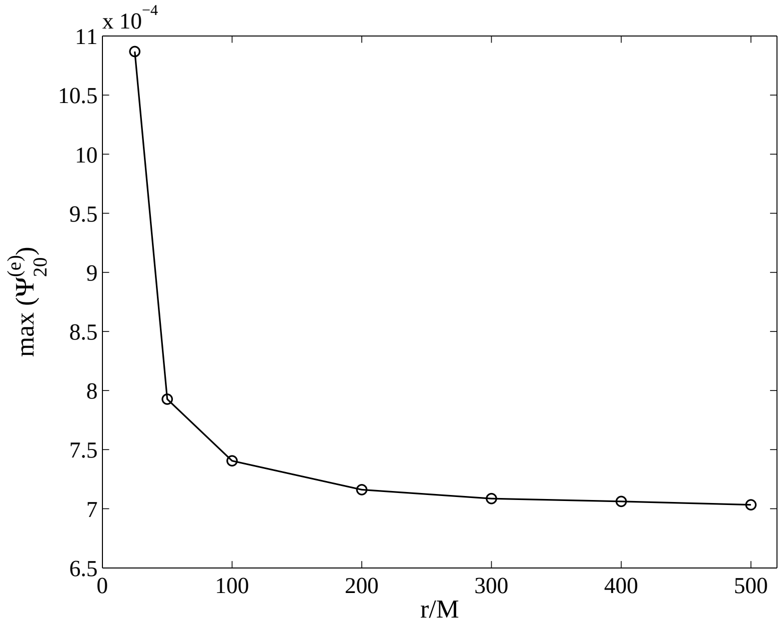

Figure 4.20: Finite extraction effects. The plot shows the maximum of the Zerilli-Moncrief function versus the extraction radii highlighting the convergence of the $\Psi^{(e)}_{20}$ for increasingly distant detectors.

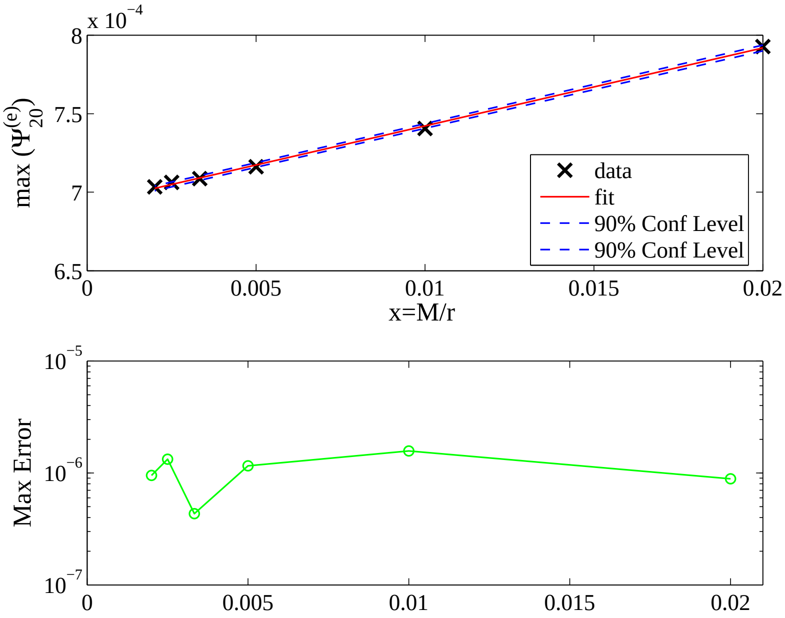

Figure 4.21: Finite extraction effects. The plot in the top panel shows the fit of the maximum of the Zerilli-Moncrief function of Fig. 4.20 with Eq. (4.3.1). The bottom panel the difference between the data and the fit.

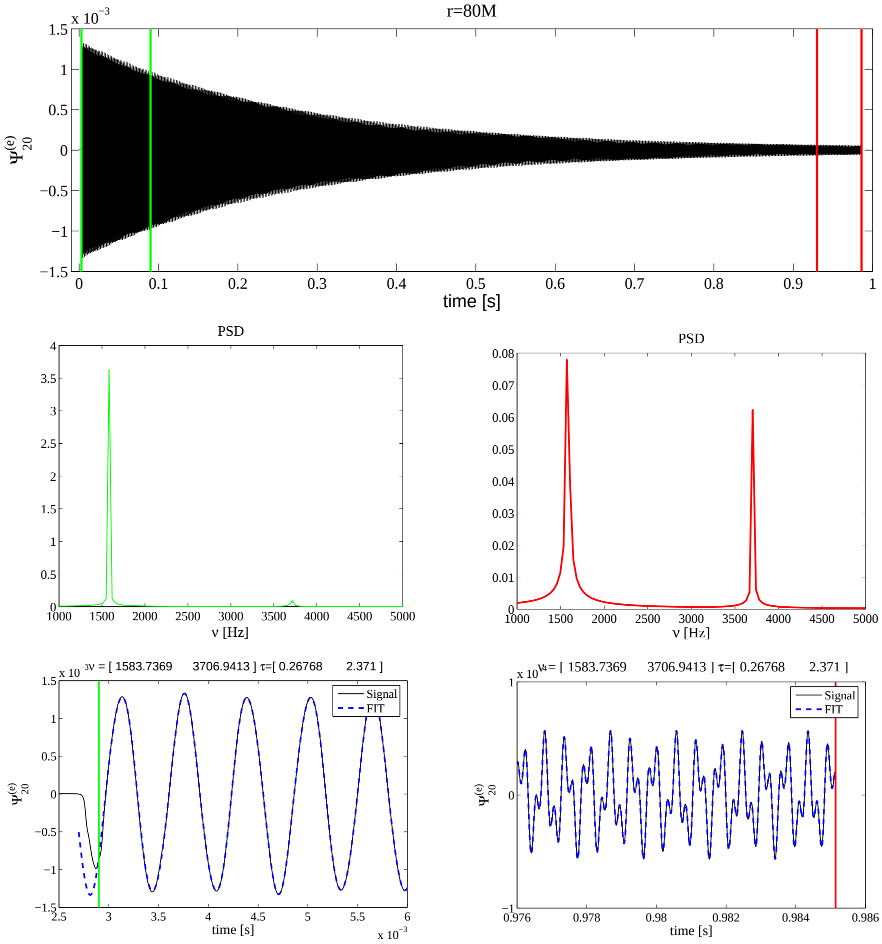

Figure 4.22: Complete analysis of the $(\ell, m) = (2, 0)$ Zerilli-Moncrief function, extracted at various isotropic radii $\bar{r} = 80M$. The top panel shows the complete waveform. The two panels in the middle show the Fourier analysis performed, respectively, in the first and the last part of the wave. The bottom panels show the result of the fit analysis with two modes ($N = 2$ in Eq. (4.1.1)) blowed up in two different part the wave. Numerical data are reported in Tab. 4.7.

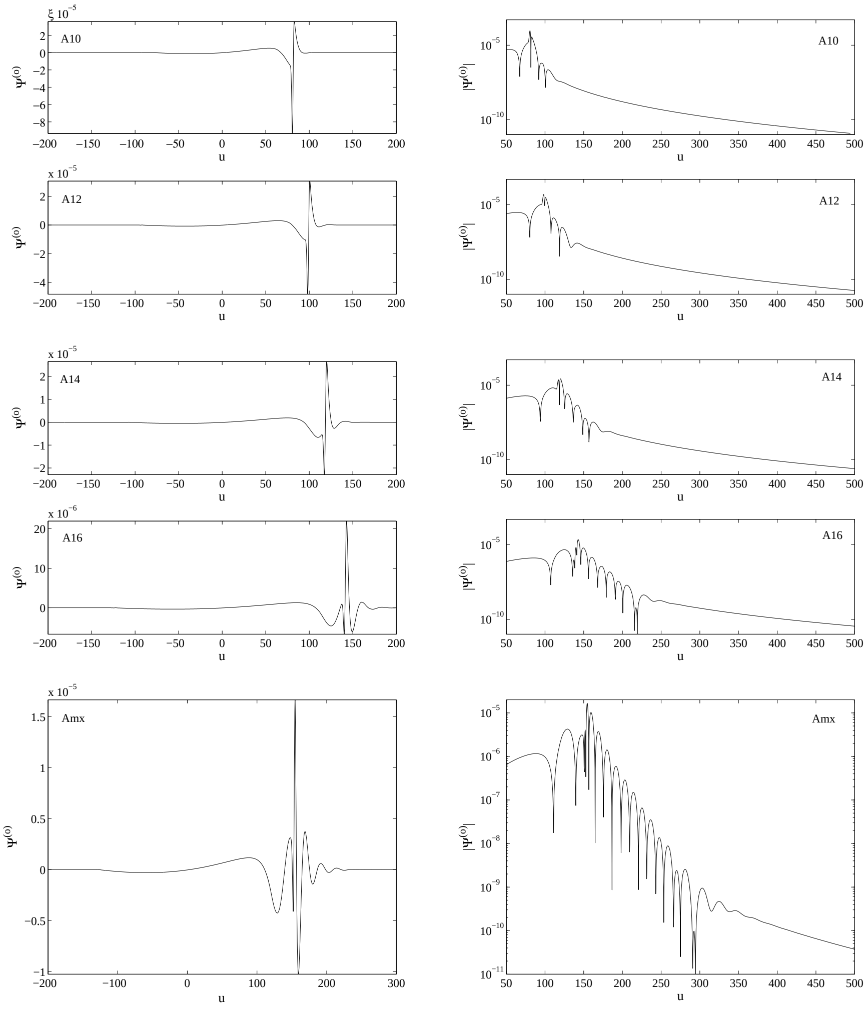

Figure 4.23: Excitation of w-modes in the odd-parity $\ell = 2$ waveforms, for different star models with EOS A, generated by the scattering of a Gaussian pulse of GWs with $b = M$. The mass and compactness of the star increases from top to bottom. The presence of w-modes is more evident for the more compact models. This qualitative behavior is common to all EOS.

Table 4.8: Frequencies of the fluid modes for the models listed in Tab. 2.3 . From left to right the columns report: the name of the model, the f-mode frequency and the first p-mode frequency obtained from the Fourier analysis, the f-mode frequency and damping time obtained from the fit analysis with one mode ($N = 1$) on a about 20 ms time-series.

Model	ν_f [Hz]	ν_p [Hz]	ν_f [Hz]	τ_f [s]
A10	2146	7444	2171.93 ± 0.01	0.187 ± 0.002
A12	2305	7816	2327.32 ± 0.01	0.145 ± 0.002
A14	2512	7873	2519.12 ± 0.01	0.114 ± 0.001
A16	2833	7823	2822.64 ± 0.01	0.107 ± 0.001
Amx	3107	7848	3121.59 ± 0.01	0.112 ± 0.001
B10	2705	7440	2697.69 ± 0.02	0.135 ± 0.003
B12	3044	8061	3020.79 ± 0.02	0.096 ± 0.001
B14	3577	8893	3562.72 ± 0.01	0.088 ± 0.001
Bmx	3732	9091	3755.12 ± 0.01	0.1000 ± 0.0004
C10	1617	5053	1631.25 ± 0.02	0.34 ± 0.01
C12	1802	5349	1780.32 ± 0.02	0.235 ± 0.006
C14	1933	5606	1936.74 ± 0.02	0.188 ± 0.003
C16	2114	5876	2116.35 ± 0.01	0.147 ± 0.002
Cmx	2627	6421	2643.94 ± 0.01	0.114 ± 0.001
FPS10	1884	6326	1877.76 ± 0.02	0.287 ± 0.008
FPS12	2028	6590	2009.99 ± 0.02	0.207 ± 0.004
FPS14	2174	6764	2155.66 ± 0.02	0.155 ± 0.002
FPS16	2325	6891	2339.33 ± 0.01	0.131 ± 0.001
FPSmx	2820	7031	2824.52 ± 0.01	0.122 ± 0.001
G10	2749	7510	2723.17 ± 0.03	0.132 ± 0.003
G12	3097	8164	3122.13 ± 0.02	0.098 ± 0.001
Gmx	3891	9080	3879.38 ± 0.01	0.097 ± 0.0007
L10	1217	4599	1243.920 ± 0.001	0.61 ± 0.03
L12	1297	4850	1297.188 ± 0.001	0.46 ± 0.01
L14	1353	5025	1347.946 ± 0.001	0.388 ± 0.008
L16	1395	5115	1401.608 ± 0.001	0.297 ± 0.005
Lmx	1871	5109	1860.619 ± 0.001	0.166 ± 0.001
N10	1415	5324	1388.618 ± 0.009	0.47 ± 0.01
N12	1466	5694	1440.541 ± 0.008	0.390 ± 0.007
N14	1497	5893	1489.246 ± 0.007	0.307 ± 0.004
N16	1522	5960	1538.080 ± 0.006	0.259 ± 0.003
Nmx	1952	5470	1964.355 ± 0.003	0.1789 ± 0.0006
O10	1481	5924	1505.787 ± 0.007	0.402 ± 0.007
O12	1578	6200	1577.605 ± 0.008	0.326 ± 0.005
O14	1643	6283	1652.329 ± 0.009	0.2401 ± 0.003
O16	1734	6217	1726.27 ± 0.01	0.204 ± 0.002
Omx	2217	5969	2208.255 ± 0.004	0.1675 ± 0.0007
SLy10	1691	5818	1713.57 ± 0.02	0.33 ± 0.01
SLy12	1804	6087	1822.60 ± 0.01	0.225 ± 0.004
SLy14	1932	6279	1930.74 ± 0.01	0.189 ± 0.003
SLy16	2029	6468	2048.66 ± 0.01	0.160 ± 0.002
SLymx	2607	6601	2593.290 ± 0.004	0.1452 ± 0.0005
WFF10	1889	6544	1868.95 ± 0.01	0.282 ± 0.007
WFF!2	1973	6766	1979.30 ± 0.01	0.204 ± 0.003
WFF14	2126	6909	2111.24 ± 0.01	0.155 ± 0.002
WFF16	2282	7016	2263.26 ± 0.01	0.129 ± 0.001
WFFmx	2718	7016	2723.90 ± 0.01	0.119 ± 0.001

Chapter 5

Gravitational - waves - extraction techniques

On a flat space-time, it is natural to express the waveform as a multipolar expansion in spin weighted spherical harmonics of spin weight $s = -2$ as

$$h_{+} - \mathrm{i}h_{\times} = \sum_{\ell=2}^{\infty} \sum_{m=-\ell}^{\ell} h^{\ell m} {}_{-2}Y^{\ell m}(\theta, \phi). \tag{5.0.1}$$

The problem of gravitational-wave extraction out of a space-time computed numerically amounts to computing, in a coordinate-independent way, the multipolar coefficients $h^{\ell m}$. Two routes are commonly followed in numerical relativity simulations of astrophysical systems which do not involve matter (like binary black hole coalescence). On one hand, one focuses on Weyl "curvature" waveforms [61], by extracting from the numerical space-time the Newman-Penrose scalar ψ_4, which is related to the second time-derivative of $(h_{+}, h_{\times})$ (See below). The metric waveform Eq. (5.0.1) is then obtained from the curvature waveform via time-integration. On the other hand, one can rely on the Regge-Wheeler [166] and Zerilli [213] theory of metric perturbations of Schwarzschild space-time, after recasting it in its gauge-invariant form according to Moncrief [137]. This allows to compute the metric waveform directly from the numerical space-time. See also Refs. [143, 173, 132] for reviews and generalizations. Moreover, if matter is involved, it is also possible to calculate the gravitational radiation emitted by the system by means of some (modified) Landau-Lifshitz quadrupole formula. In this chapter we review the main elements of the three wave-extraction procedures.

5.1 Abrahams-Price *metric* extraction

The wave-extraction formalism based on the perturbation theory of a Schwarzschild space-time was introduced by Abrahams and Price [2] and subsequently employed by many authors [1, 60, 7, 8].

The assumption underlying this extraction method is that, far from the strong-field regions, the numerical space-time can be well approximated as the sum of a spherically symmetric Schwarzschild "background" $\mathring{g}_{\mu\nu}$ and a non-spherical perturbation $\delta g_{\mu\nu}$. Even if based on the gauge-invariant formulation of perturbations due to Moncrief [137], The standard implementation [2] of this approach is done by fixing a coordinate system (Schwarzschild coordinates) for the background. As usual, the spherical symmetry [1] of $\mathring{g}_{\mu\nu}$ allows one to eliminate the dependence on the angles (θ, ϕ) by expanding $\delta g_{\mu\nu}$ in (tensor) spherical harmonics, *i.e.* seven even-parity and three odd-parity multipoles. The multipolar expansion explicitly reads

$$g_{\mu\nu}(t,r,\theta,\phi) = \mathring{g}_{\mu\nu} + \sum_{\ell=2}^{\infty}\sum_{m=-\ell}^{\ell}\left[\left(\delta g_{\mu\nu}^{\ell m}\right)^{(\mathrm{o})} + \left(\delta g_{\mu\nu}^{\ell m}\right)^{(\mathrm{e})}\right] . \tag{5.1.1}$$

The metric multipoles $\left(\delta g_{\mu\nu}^{\ell m}\right)^{(\mathrm{o/e})}$ (and their derivatives) can be combined together in two gauge-invariant master functions, the even-parity (Zerilli-Moncrief) $\Psi_{\ell m}^{(\mathrm{e})}$ (See Chap. 3) and the odd-parity (Regge-Wheeler) $\Psi_{\ell m}^{(\mathrm{o})}$. These two master functions satisfy two decoupled wave-like equations with a potential [2] . Finally, in a radiative coordinate system we have

$$h^{\ell m} = \frac{N_\ell}{r}\left(\Psi_{\ell m}^{(\mathrm{e})} + \mathrm{i}\Psi_{\ell m}^{(\mathrm{o})}\right), \tag{5.1.2}$$

where $N_\ell = \sqrt{(\ell+2)(\ell+1)\ell(\ell-1)}$.

Note that the use of Schwarzschild coordinates for the background metric is not at all necessary and more general wave-extraction frameworks exist. In particular, Sarbach and Tiglio [173] and Martel and Poisson [132] have shown that there exists a generalized formalism for perturbations that is not only gauge-invariant (*i.e.* invariant under infinitesimal coordinate transformation), but also *coordinate independent*, in the sense that it is invariant under *finite* coordinate transformations of the M^2 Lorentzian submanifold of the background. Since in a numerical-relativity simulation the gauge depends on time, one is a priori expecting that the gauge-fixing of the background may introduce systematic errors. For the odd-parity case, Ref. [157] has shown that this is indeed the case for the particular physical setting represented by the scattering of a Gaussian pulse of gravitational waves on a Schwarzschild black hole in Kerr-Schild coordinates (See also Ref. [120] for the even-parity case).

5.2 Newman-Penrose *curvature* extraction

The use of Weyl scalars for wave-extraction purposes has become very common in numerical relativity and it has been successfully applied in current binary–black-hole (See Ref. [162] and references therein), binary–neutron-star [25] and mixed binary [83] simulations.

Given a spatial hypersurface with time-like unit normal n^μ and given a spatial unit vector r^μ in the direction of the wave propagation, the standard definition of ψ_4 is the following component of the Weyl curvature tensor $C_{\alpha\mu\beta\nu}$

$$\psi_4 = -C_{\alpha\mu\beta\nu}\ell^\mu\ell^\nu\bar{m}^\alpha\bar{m}^\beta, \tag{5.2.1}$$

---

[1] That is, the background 4-manifold $\mathcal{M}$ can be written as $\mathcal{M} = M^2 \times S^2$, where M^2 is a 2-dimensional Lorentzian manifold and S^2 is the unit 2-sphere. See Sec. 3.1.

[2] The equations are just approximately satisfied on the extracted "background".

where $\ell^\mu \equiv 1/\sqrt{2}(n^\mu - r^\mu)$ and m^μ is a complex null vector (such that $m^\mu \bar{m}_\mu = 1$) that is orthogonal to r^μ and n^μ. This scalar can be identified with the gravitational radiation if a suitable frame is chosen at the extraction radius. On a curved space-time there is considerable freedom in the choice of the vectors r^μ and m^μ and different researchers have made different choices, which are all equivalent in the $r \to \infty$ limit (See for example [145] and references therein). In practice, when a 3D Cartesian grid is used to represent the three-space in numerical relativity, it is possible to define an orthonormal basis $(\hat{e}_r, \hat{e}_\theta, \hat{e_\phi})$, centered on the Cartesian origin and oriented with poles along the z-axis. The normal to the slice defines a time-like vector $\hat{e}_t$, from which we construct the null frame

$$l = \frac{1}{\sqrt{2}}(\hat{e}_t - \hat{e}_r) \ , \quad n = \frac{1}{\sqrt{2}}(\hat{e}_t + \hat{e}_r) \ , \quad m = \frac{1}{\sqrt{2}}(\hat{e}_\theta - \mathrm{i} e_\phi) \ . \tag{5.2.2}$$

Then ψ_4 is calculated via a reformulation of Eq. (5.2.1) in terms of ADM variables on the slice [102],

$$\psi_4 = C_{ij} \bar{m}^i \bar{m}^j , \tag{5.2.3}$$

where

$$C_{ij} \equiv R_{ij} - K K_{ij} + K_i^{\ k} K_{kj} - \mathrm{i} \epsilon_i^{\ kl} \nabla_l K_{jk} . \tag{5.2.4}$$

The gravitational-wave polarization amplitudes h_+ and $h_\times$ are related to ψ_4 by Ref. [192]

$$\ddot{h}_+ - \mathrm{i} \ddot{h}_\times = \psi_4 . \tag{5.2.5}$$

It is then convenient to expand ψ_4 in spin-weighted spherical harmonics of weight $s = -2$ as

$$\psi_4(t, r, \theta, \phi) = \sum_{\ell=2}^{\infty} \sum_{m=-\ell}^{\ell} \psi_4^{\ell m}(t, r)\,{}_{-2}Y^{\ell m}(\theta, \phi) , \tag{5.2.6}$$

so that the relation between $\psi_4^{\ell m}$ and the metric multipoles $h^{\ell m}$ becomes

$$\ddot{h}^{\ell m}(t, r) = \psi_4^{\ell m}(t, r) \ . \tag{5.2.7}$$

5.2.1 Recovering the GW polarization amplitudes

Since the output of a simulation is $\psi_4^{\ell m}(t, r)$, the problem that emerge at this point is to recover the gravitational wave multipoles from the numerically computed Weyl scalar. $h^{\ell m}(t, r)$ is the double indefinite integral of $\psi_4^{\ell m}(t, r)$, which can be (numerically) computed (after multiplying both sides by r) as

$$r\, \tilde{h}^{\ell m}(t, r) \equiv \int_0^t dt' \int_0^{t'} dt'' r\, \psi_4^{\ell m}(t'', r) \ , \tag{5.2.8}$$

which results in

$$r\, h^{\ell m}(t, r) = r \tilde{h}^{\ell m}(t, r) + Q_0 + t\, Q_1 \ , \tag{5.2.9}$$

where the integration constants Q_0 and Q_1 are explicitly written. They can be determined from the data themselves and their physical meanings are: $Q_0 = r h^{\ell m}(0, r)$ and $Q_1 = r \dot{h}^{\ell m}(0, r)$.

This is not the end of the story yet: the equations discussed so far refer to a signal extracted at a *finite* value of r, while one is interested in computing $\psi_4^{\ell m}$ at spatial infinity. It is imaginable that there may be an offset, dependent on the extraction radius, in the computed values of $\psi_4^{\ell m}(t,r)$; that is $\psi_4^{\ell m}$ at spatial infinity should be written as

$$r\psi_4^{\ell m}(t) := r\psi_4^{\ell m}(t,r) + 2Q_2(r) \; , \tag{5.2.10}$$

where $\psi_4^{\ell m}(t,r)$ is the scalar extracted at a finite radius r and $2Q_2(r)$ is an *offset* function, that takes into account (in an additive way) the effects of the extraction at a finite radius. The time integration of this offset generates an additional term that is quadratic in time, so that the final result for $rh^{\ell m}(t)$ is

$$r\,h^{\ell m}(t) = r\,\tilde{h}^{\ell m}(t,r) + Q_0 + Q_1 t + Q_2(r)t^2 \; . \tag{5.2.11}$$

The term $Q_2(r)$ should tend to zero when the extraction radius goes to infinity, as we checked on the results of our simulation (See Sec. 6.5).

Various ways of fixing the two integration constants Q_0 and Q_1 have been discussed in the literature about coalescing binary black-hole systems [46, 158, 30, 74]. In particular, in Appendix A of Ref. [74] the following procedure was proposed: (i) Integrate the curvature waveform twice forward in time (starting from $t = 0$ and including the initial burst of radiation due to the initial data setup); (ii) Subtract the linear-in-time offset present in there. This simple procedure led to an accurate metric waveform which exhibited the correct circular polarization behavior. A similar line was also followed in Ref. [46], where it was pointed out that in some situations (*e.g.* close extraction radius, higher multipoles) one needs to subtract a general polynomial in t, consistently with our Eq. (5.2.11).

5.3 Landau-Lifshitz quadrupole-type formulas

In the presence of matter, it is sometimes convenient to extract gravitational waves using also some kind of (improved) Landau-Lifshitz "quadrupole" formula. Although this formula is not gauge-invariant, this route has been followed by many authors with different degrees of sophistication [87, 77, 180, 182, 183] to give well approximated waveforms [180]. For the sake of completeness, let us review how this quadrupole formula came into being, as the first contribution in a multipolar expansion and let us express it in the convenient form of $h^{\ell m}$, as outlined above. The basic reference of the formalism is a review by Thorne [196]; most of the useful formulas of this review have been collected by Kidder [112], who condenses and summarizes the gravitational-wave–generation formalism developed in Refs. [48, 49].

Following Ref. [112], we recall that Eq. (5.1.2) can be derived in all generality by: (i) Decomposing the asymptotic waveform $h_{ij}^{\rm TT}$ into two sets of symmetric trace-free (STF) radiative multipole moments (to be related later to the matter multipole moment of the source in the near-zone) called $\mathcal{U}_L$ and $\mathcal{V}_L$, where a capital letter for an index denotes a multi-index (*i.e.* , $\mathcal{U}_L = \mathcal{U}_{i_1 i_2 \dots i_\ell}$); (ii) Projecting the STF-decomposed $h_{ij}^{\rm TT}$ along an orthonormal triad that corresponds to that of the spherical coordinate system. In the same notation of Ref. [112], Eq. (5.1.2) reads

$$h^{\ell m} = \frac{1}{\sqrt{2}r}\left(U^{\ell m} - {\rm i}V^{\ell m}\right) \; , \tag{5.3.1}$$

where the mass multipole moments $U^{\ell m}$ and current multipole moments $V^{\ell m}$ are related to their STF counterparts by

$$U^{\ell m} = \frac{16\pi}{(2\ell+1)!!}\sqrt{\frac{(\ell+1)(\ell+2)}{2\ell(\ell-1)}}\mathcal{U}_L\mathcal{Y}_L^{\ell m*} \ , \tag{5.3.2}$$

$$V^{\ell m} = -\frac{32\pi\ell}{(2\ell+1)!!}\sqrt{\frac{\ell+2}{2\ell(\ell+1)(\ell-1)}}\mathcal{V}_L\mathcal{Y}_L^{\ell m*} \ , \tag{5.3.3}$$

where $\mathcal{Y}_L^{\ell m}$ are the STF spherical harmonics. These functions form a basis of the of the $(2\ell+1)$-dimensional vector space of STF ℓ-tensors; they are related to the scalar spherical harmonics by

$$Y^{\ell m} = \mathcal{Y}_L^{\ell m} N_L \ , \tag{5.3.4}$$

where N_i is a component of the the unit radial vector. The expanded form of the STF $\mathcal{Y}_L^{\ell m}$ are given in Refs. [203, 196] (See also Eq. (A6a) of Ref. [48]). In the post-Newtonian (PN) wave-generation formalism of Refs. [48, 49], one can relate in a systematic manner the radiative multipole moments $(\mathcal{U}_L, \mathcal{V}_L)$ to a set of six STF source moments $(\mathcal{I}_L, \mathcal{J}_L, \mathcal{W}_L, \mathcal{X}_L, \mathcal{Y}_L, \mathcal{Z}_L)$, which can be computed from the stress energy pseudo-tensor of the matter and of the gravitational field of the source. A set of two canonical source moments $(\mathcal{M}_L, \mathcal{S}_L)$ can be computed as an intermediate step between the source moments and the radiative moment. Two of the source moments, the mass moments $\mathcal{I}_L$ and the current moment $\mathcal{J}_L$ are dominant, while the others only make a contribution starting at 2.5 PN order, and we neglect them here. In a first approximation (*i.e.* neglecting the nonlinear "tail-interactions" as well as higher-order nonlinear interactions), the L-th radiative moment is given by the ℓ-th time derivative of the canonical moments as

$$\mathcal{U}_L \equiv \mathcal{I}_L^{(\ell)} + O(\varepsilon^{5/2}), \tag{5.3.5}$$

$$\mathcal{V}_L \equiv \mathcal{J}_L^{(\ell)} + O(\varepsilon^{5/2}), \tag{5.3.6}$$

where $\varepsilon \sim (v/c)^2$ indicates some PN ordering parameter of the system. As a result, the computation of $U_{\ell m}$ and $V_{\ell m}$ is straightforward. As an example (that will be used in the following), let us focus on the $\ell = 2$ moments of a general astrophysical system with equatorial symmetry. In this case, the $(2,1)$ moment is purely odd-parity, while the $(2,0)$ and $(2,2)$ are purely even-parity. Straightforward application of what we have reviewed so far gives

$$h^{20} = \frac{1}{r}\sqrt{\frac{24\pi}{5}}\left(\ddot{\mathcal{I}}_{zz} - \frac{1}{3}\mathrm{Tr}(\ddot{\mathcal{I}})\right), \tag{5.3.7a}$$

$$h^{21} = -\frac{\mathrm{i}}{r}\sqrt{\frac{128\pi}{45}}\left(\ddot{\mathcal{J}}_{xz} - \mathrm{i}\ddot{\mathcal{J}}_{yz}\right), \tag{5.3.7b}$$

$$h^{22} = \frac{1}{r}\sqrt{\frac{4\pi}{5}}\left(\ddot{\mathcal{I}}_{xx} - 2\mathrm{i}\ddot{\mathcal{I}}_{xy} - \ddot{\mathcal{I}}_{yy}\right). \tag{5.3.7c}$$

In the harmonic gauge, in the case of small velocity and negligible internal stresses (*i.e.* in the Newtonian limit) one has $\mathcal{I}_{ij} = \int d^3x\rho x_i x_j$ and $\mathcal{J}_{ij} = \int d^3x\rho\varepsilon_{abi}x_j x_a v^b$. The 1 PN corrections to the mass quadrupole have been computed in Ref. [50]. Recently, Ref. [65] included 1 PN correction, using an effective 1 PN quadrupole momentum, in the gravitational-wave–extraction procedure from supernova core-collapse simulations. As a complementary approach, Ref. [180] proposed to "effectively" take into account possible general relativistic corrections by inserting in Eq. (5.3.7) the following effective "quadrupole moment" defined in terms of the "coordinate rest-mass density" $\rho_* \equiv \alpha\sqrt{\gamma}u^0\rho$,

$$\mathcal{I}_{ij} = \int d^3x \rho_* x_i x_j \, . \tag{5.3.8}$$

This presents some very useful properties: (i) It is of simple implementation; (ii) From the continuity equation $\partial_t\rho_* + \partial_i(\rho_* v^i) = 0$, one can analytically compute the first time-derivative of the quadrupole moment, so that only one numerical time-derivative needs to be evaluated. The last property is extremely important: in fact, on data computed via a second-order accurate numerical scheme it is not possible to calculate noise-free third derivatives, which are needed for the gravitational-wave luminosity. The accuracy of a scheme based on Eq. (5.3.8) has been tested in Ref. [180] in the case of neutron-star oscillations and was subsequently used by various authors to estimate the gravitational-wave emission in other physical scenarios. See for example Refs. [181, 182, 23, 78]. In order to get some more insight on the accuracy of possible "generalized" *standard quadrupole formulas* (SQFs formulas), a strategy was proposed in Ref. [142], namely to test some pragmatic modifications of the quadrupole formula and to check which one is closer to the actual gravitational waveform. The same strategy was used systematically in [22] where we proposed a sort of generalized "quadrupole moment" of the form

$$\mathcal{I}_{ij}[\varrho] \equiv \int d^3x \varrho x_i x_j \, , \tag{5.3.9a}$$

where now the "matter density" is substitute by the following generalized effective densities ϱ:

$$\text{SQF} \quad \varrho := \rho \tag{5.3.9b}$$
$$\text{SQF1} \quad \varrho := \alpha^2\sqrt{\gamma}T^{00} \tag{5.3.9c}$$
$$\text{SQF2} \quad \varrho := \sqrt{\gamma}W\rho \tag{5.3.9d}$$
$$\text{SQF3} \quad \varrho := u^0\rho = \frac{W}{\alpha}\rho \, . \tag{5.3.9e}$$

Any of the "quadrupole formulas" obtained using these generalized quadrupole moments should be considered better than the others. Note that none of them is gauge invariant and, indeed, the outcome will change if one is considering isotropic or Schwarzschild-like coordinates. These formulas were widely used in the literature and the main purpose of the comparison among Eq. (5.3.9) is to give an idea of the kind of information that can be safely assessed using them. A detailed analysis on the performance of these SQFs in the case of the GW emitted by a non-rotating stars will be discussed in Sec. 6.7.

Chapter 6

Gravitational waves from neutron star oscillations: non-linear simulations

In this Chapter we present and discuss the results of simulations of oscillating NS performed with a nonlinear and 3-dimensional code that solve the Einstein equations coupled to the equation of motion for the matter without approximations. The GW emission is computed in these simulations by the state-of-art methods described in Chap. 5. Because the initial data evolved are exactly the same as in the PERBACCO , the 3D nonlinear results are discussed comparing and contrasting with the 1D linear ones. On one hand this permits the analysis of the validity of the linear regime and of the emerging of nonlinear phenomena. On the other hand it represents a test-bed for the 3D nonlinear code, useful to check the physical consistency of the results and the performances of the wave extraction techniques. The 3D nonlinear code employed in these simulations is the `CACTUS-CARPET-CCATIE-Whisky` code [59, 64, 208] that currently represents the best tool for the investigation of both vacuum and matter spacetimes, see *e.g.* [27, 158, 167, 25].

6.1 "3+1" NOK-BSSN formulation of Einstein equations

To be numerically solved by the `CACTUS-CCATIE` code, the Einstein filed equations are casted in a conformal-traceless "3+1" formulation [144, 179, 36, 5], in which the space-time is decomposed into three-dimensional spacelike slices, described by a metric γ_{ij}, its embedding in the full space-time, specified by the extrinsic curvature K_{ij}, and the gauge functions α (lapse) and β^i (shift), that specify a coordinate frame (See Sec. 1.2.1 for a brief introduction to "3+1" formalism, Ref. [211] for a general description of the 3+1 split and see Sec. 6.1.1 for details on how the gauges can be treated). The particular system which the code evolves transforms the standard ADM variables as follows. The three-metric γ_{ij}

is conformally transformed via

$$\phi = \frac{1}{12}\ln\det\gamma_{ij}, \qquad \tilde{\gamma}_{ij} = e^{-4\phi}\gamma_{ij} \tag{6.1.1}$$

and the conformal factor ϕ is evolved as an independent variable, whereas $\tilde{\gamma}_{ij}$ is subject to the constraint $\det\tilde{\gamma}_{ij} = 1$. The extrinsic curvature is subjected to the same conformal transformation and its trace $\operatorname{tr} K_{ij}$ is evolved as an independent variable. That is, in place of K_{ij}, the variables considered are:

$$K \equiv \operatorname{tr} K_{ij} = g^{ij}K_{ij}, \qquad \tilde{A}_{ij} = e^{-4\phi}(K_{ij} - \frac{1}{3}\gamma_{ij}K), \tag{6.1.2}$$

with $\operatorname{tr}\tilde{A}_{ij} = 0$. Finally, new evolution variables

$$\tilde{\Gamma}^i = \tilde{\gamma}^{jk}\tilde{\Gamma}^i_{jk} \tag{6.1.3}$$

are introduced, defined in terms of the Christoffel symbols of the conformal three-metric.

The Einstein equations specify a well-known set of evolution equations for the listed variables and are given by

$$(\partial_t - \mathcal{L}_\beta)\,\tilde{\gamma}_{ij} = -2\alpha\tilde{A}_{ij}\,, \tag{6.1.4a}$$

$$(\partial_t - \mathcal{L}_\beta)\,\phi = -\frac{1}{6}\alpha K\,, \tag{6.1.4b}$$

$$\begin{aligned}(\partial_t - \mathcal{L}_\beta)\,\tilde{A}_{ij} = {}& e^{-4\phi}[-D_iD_j\alpha + \alpha(R_{ij} - 8\pi S_{ij})]^{TF} \\ &+ \alpha(K\tilde{A}_{ij} - 2\tilde{A}_{ik}\tilde{A}^k{}_j),\end{aligned} \tag{6.1.4c}$$

$$\begin{aligned}(\partial_t - \mathcal{L}_\beta)\,K = {}& -D^iD_i\alpha \\ &+ \alpha\Big[\tilde{A}_{ij}\tilde{A}^{ij} + \frac{1}{3}K^2 + 4\pi(E+S)\Big],\end{aligned} \tag{6.1.4d}$$

$$\begin{aligned}\partial_t\tilde{\Gamma}^i = {}& \tilde{\gamma}^{jk}\partial_j\partial_k\beta^i + \frac{1}{3}\tilde{\gamma}^{ij}\partial_j\partial_k\beta^k + \beta^j\partial_j\tilde{\Gamma}^i - \tilde{\Gamma}^j\partial_j\beta^i \\ &+ \frac{2}{3}\tilde{\Gamma}^i\partial_j\beta^j - 2\tilde{A}^{ij}\partial_j\alpha + 2\alpha(\tilde{\Gamma}^i{}_{jk}\tilde{A}^{jk} + 6\tilde{A}^{ij}\partial_j\phi \\ &- \frac{2}{3}\tilde{\gamma}^{ij}\partial_jK - 8\pi\tilde{\gamma}^{ij}S_j),\end{aligned} \tag{6.1.4e}$$

where R_{ij} is the three-dimensional Ricci tensor, D_i the covariant derivative associated with the three metric γ_{ij}, "TF" indicates the trace-free part of tensor objects and E, S_j and S_{ij} are the matter source terms measured by the Eulerian observer, *cf.* Eq. (1.2.7).

The Einstein equations also lead to a set of physical constraint equations that are satisfied within each spacelike slice,

$$\mathcal{H} \equiv R^{(3)} + K^2 - K_{ij}K^{ij} - 16\pi E = 0, \tag{6.1.5}$$

$$\mathcal{M}^i \equiv D_j(K^{ij} - \gamma^{ij}K) - 8\pi S^i = 0, \tag{6.1.6}$$

which are usually referred to as Hamiltonian and momentum constraints. Here $R^{(3)} = R_{ij}\gamma^{ij}$ is the Ricci scalar on a three-dimensional time-slice. The specific choice of evolution variables introduces five additional constraints,

$$\det\tilde{\gamma}_{ij} = 1, \tag{6.1.7a}$$

$$\operatorname{tr}\tilde{A}_{ij} = 0, \tag{6.1.7b}$$

$$\tilde{\Gamma}^i = \tilde{\gamma}^{jk}\tilde{\Gamma}^i_{jk}. \tag{6.1.7c}$$

The numerical procedure coded actively enforces the algebraic constraints Eq. (6.1.7a) and Eq. (6.1.7b). The remaining constraints, $\mathcal{H}$, $\mathcal{M}^i$, and Eq. (6.1.7c), are not actively enforced and can be used as monitors of the accuracy of our numerical solution. See Ref. [4] for a more comprehensive discussion of the the above formalism.

All the equations discussed above (See also those in Sec. 6.1.1) are solved using the `CCATIE` code, a three-dimensional finite-differencing code based on the Cactus Computational Toolkit [96]. A detailed presentation of the code and of its convergence properties have been recently presented in Ref. [158].

Mesh refinement is achieved through the Carpet code [174], that implements a refinement scheme based on nested ("box-in-box") grids. The fixed refinement factor for two successive grid level is 2 : 1.

Coupled to the system in Eq. (6.1.4) the general-relativistic hydrodynamics equations in the flux-conservative formulation described in Sec. 1.2.1 are solved with the `Whisky` code [25, 23, 28, 27, 24, 26]. In the algorithm used by this code all variables $\vec{q}$ (See Eq. (1.2.8)) are represented on the numerical grid by cell-integral averages. The functions that $\vec{q}$ represent are then *reconstructed* within each cell, usually by piecewise polynomials, in a way that preserves conservation of the variables $\vec{q}$ [202]. This operation produces two values at each cell boundary, which are then used as initial data for the local Riemann problems, whose (approximate) solution gives the fluxes through the cell boundaries. A Method-of-Lines approach [202], which reduces the partial differential equations Eq. (1.2.9) to a set of ordinary differential equations that can be evolved using standard numerical methods, such as Runge-Kutta or the Iterative Cranck-Nicholson schemes [193, 127], is used to update the equations in time (See Ref. [26] for further details). The `Whisky` code implements several reconstruction methods, such as Total-Variation-Diminishing (TVD) methods, Essentially-Non-Oscillatory (ENO) methods [107] and the Piecewise Parabolic Method (PPM) [70]. Also, a variety of approximate Riemann solvers can be used, starting from the Harten-Lax-van Leer-Einfeldt (HLLE) solver [108], over to the Roe solver [168] and the Marquina flux formula [9] (See Ref. [26, 24] for a more detailed discussion).

The results we are going to present are computed using the PPM method for the reconstruction and the Marquina formula for the approximate fluxes. The employed finite differencing for the spacetime evolution with the `CCATIE` code is 4th-order accurate and the Iterative Cranck-Nicholson scheme with three substeps is used for the time evolution, with a Courant-Friedrichs-Lewy factor equal to 0.25.

6.1.1 Gauges

A common choice in numerical relativity is to specify the gauge using the "$1 + \log$" slicing for the lapse [69], and the hyperbolic $\tilde{\Gamma}$-driver condition for the shift [4]. With this method the lapse obeys the condition [52]:

$$\partial_t \alpha - \beta^i \partial_i \alpha = -2\alpha(K - K_0) \,, \tag{6.1.8}$$

where K_0 is the initial value of the trace of the extrinsic curvature and equals zero for the maximally sliced initial data we consider here. The shift instead is

Table 6.1: Equilibrium properties of model A0. From left to right the columns report: central rest-mass density, central total energy density, gravitational mass, radius, compactness.

Name	ρ_c	ε_c	M	R	M/R
A0	1.28×10^{-3}	1.44×10^{-3}	1.40	9.57	0.15

evolved using the hyperbolic equation:

$$\partial_t \beta^i - \beta^j \partial_j \beta^i = \frac{3}{4} \alpha B^i \tag{6.1.9a}$$

$$\partial_t B^i - \beta^j \partial_j B^i = \partial_t \tilde{\Gamma}^i - \beta^j \partial_j \tilde{\Gamma}^i - \eta B^i \ , \tag{6.1.9b}$$

where η is a parameter which acts as a damping coefficient. The advection terms on the right-hand sides of these equations have been suggested in Refs. [29, 204, 119].

6.1.2 Treatment of the atmosphere

At least mathematically, the region outside our initial stellar models is assumed to be perfect vacuum. Independently of whether this represents a physically realistic description of a compact star, the vacuum represents a singular limit of Eq. (1.2.7a) and Eq. (1.2.7c), and must be treated artificially. We have here followed a standard approach in computational fluid-dynamics and added a tenuous "atmosphere" filling the computational domain outside the star.

We treat the atmosphere as a perfect fluid governed by the same EOS used for the bulk matter, but having a zero coordinate velocity. Furthermore, its rest-mass density is set to be several (6 in the present case) orders of magnitude smaller than the initial central rest-mass density.

The evolution of the hydro-dynamical equations in grid-zones where the atmosphere is present is the same as the one used in the bulk of the flow. Furthermore, when the rest mass in a grid-zone falls below the threshold set by the atmosphere, that grid-zone is simply not updated in time and the value of its rest-mass density and velocity are set to those of the atmosphere.

6.2 Equilibrium model and radial oscillations

As a representative model for a NS, we choose a model described by a polytropic EOS (Eq. (1.3.25)) with $\Gamma = 2$, $K = 100$ and central rest-mass density $\rho_c = 1.28 \times 10^{-3}$. This choice gives a rest mass of $M \simeq 1.4$ and a radius of $R \simeq 9.57$, other equilibrium properties are listed in Tab. 6.1. This model has been widely used in the literature and it is known as model A0, see Ref. [188], or AU0, see Tab. 2.2.

The unperturbed configuration A0 has been stably evolved for about 20 ms. The numerical 3D grid used for this simulation is composed of two concentric cubic boxes with limits $[-32, 32]$ and $[-16, 16]$ in all the three Cartesian directions. The boxes have resolutions $\Delta_{xyz} = 0.5$ and 0.25 respectively; bitant symmetry, *i.e.* the $z < 0$ domain is copied from the $z > 0$ domain instead

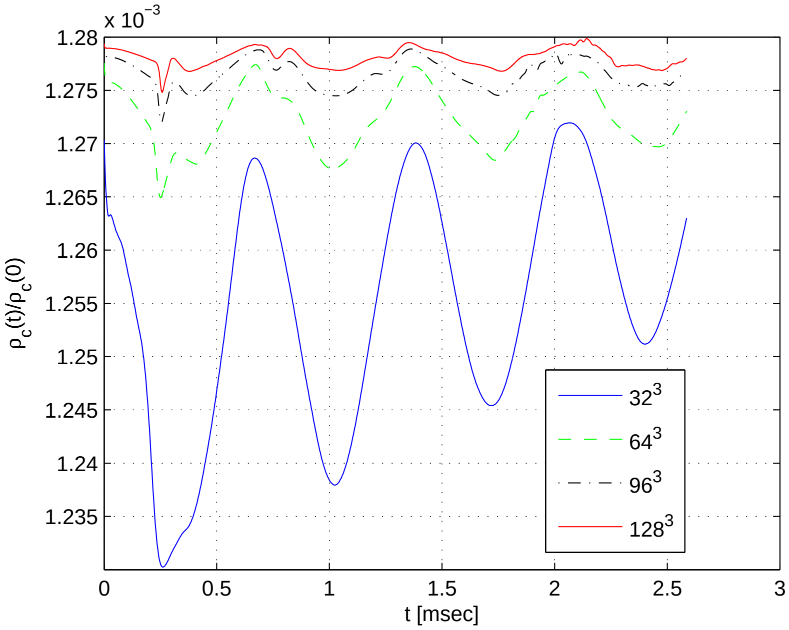

Figure 6.1: Convergence of the radial oscillations triggered by truncation errors. The central mass density is showed versus time for different resolutions: the oscillations, due to the truncation errors of the numerical scheme, correspond to the physical frequency of the F mode are significantly reduced for higher resolutions. This tests is done using a one-refinement 3D Cartesian grid with limits $[-32, 32]$ for each direction, and increasing number of grid points: $N_{\rm gp} = \{32^3, 64^3, 96^3, 128^3\}$.

of being evolved, was imposed as a boundary condition in order to save computational time. We performed also simulations with a single box with limits $[-32, 32]$ all the three Cartesian directions and different resolutions and without symmetries.

It is well known that the truncation errors of the numerical scheme trigger physical radial oscillations of (mainly) the fundamental mode F and the first overtones (See the tests runs in Fig. 6.1). We have checked that these frequencies agree with those computed evolving the radial pulsation equation with the perturbative code: this comparison is shown in Tab. 6.2. We note in passing that our numbers are in perfect agreement with those of Table I of Ref. [90].

As a further check, the entire sequence of uniformly rotating models with mass $M = 1.4$ and non-rotating limit A0 has been evolved. Simulations were done with a cubic grid with limits $[-32, 32]$ in each direction, and uniformly spaced with grid spacing $\Delta_{xyz} = 0.5$. As before, we have imposed bitant symmetry. The sequence of initial models has been computed by means of the version of the `RNS` code [189] implemented in `Whisky`. For the equilibrium properties of the models, see Ref. [79] and Tab. 2.2.

The fluid modes of this sequence were previously investigated in different works, using various approaches [89, 188, 79]. With our general-relativistic 3D

Table 6.2: Frequencies of the radial modes of model A0. The fundamental mode frequency and two overtones computed from the 1D linear evolution and from the 3D nonlinear evolution of the A0 model are showed. They agree within 1%.

n	1D [Hz]	3D [Hz]	Diff. [%]
0	1462	1466	0.3
1	3938	3935	0.1
2	5928	5978	0.8

Table 6.3: Frequencies of the fundamental radial mode of models in the sequence AU of uniformly rotating polytropic. The equilibrium models were described in Sec. 2.4.2 (See also Refs. [188] and [79]). The frequency of model AU0 (A0) has also been computed in Ref. [90] (1450 Hz) and in this work using Fourier analysis (1462 Hz), where a finer grid was used (See Tab. 6.2). The data in the column marked as "CF" refer to Table III of Ref. [79]. The data in the column marked as "Cowling" refer to Table II of Ref. [188].

MODEL	F [Hz]	F(CF) [Hz]	F(Cowling) [Hz]
AU0	1444	1458	2706
AU1	1369	1398	2526
AU2	1329	1345	2403
AU3	1265	1283	2277
AU4	1166	1196	2141
AU5	1093	1107	1960

simulations we are able to study the effect of rotation on the radial mode and compare the results with those obtained via approximated approaches. Our results are summarized in Tab. 6.3. We have found that the frequencies computed by Dimmelmeier et al. [79] in the conformally flat approximation are consistent with ours (the difference is of the order of few percents); on the other hand, the results of Stergioulas et al. [188], obtained in the Cowling approximations, differ of about a factor two, consistently with the estimates of Ref. [212]. In all cases, the frequencies decrease if the rotation increases and the trend is linear in the rotational parameter $\beta \equiv T/|W|$, the ratio between the kinetic rotational energy and the gravitational potential energy.

6.3 Initial data: adding a perturbation

In both the linear and nonlinear codes, setting up the initial data describing a perturbed star amounts to: (i) Solving the Tolman-Oppenheimer-Volkov (TOV) equations to construct the equilibrium configuration; (ii) Fixing an axisymmetric pressure perturbation; (iii) Solving the linearized constraints for the metric perturbations. Here we describe the setup of conformally flat initial data used in the PerBaCCo for the simulations described in Sec. 4.3.3 and evolved also with the nonlinear 3D code.

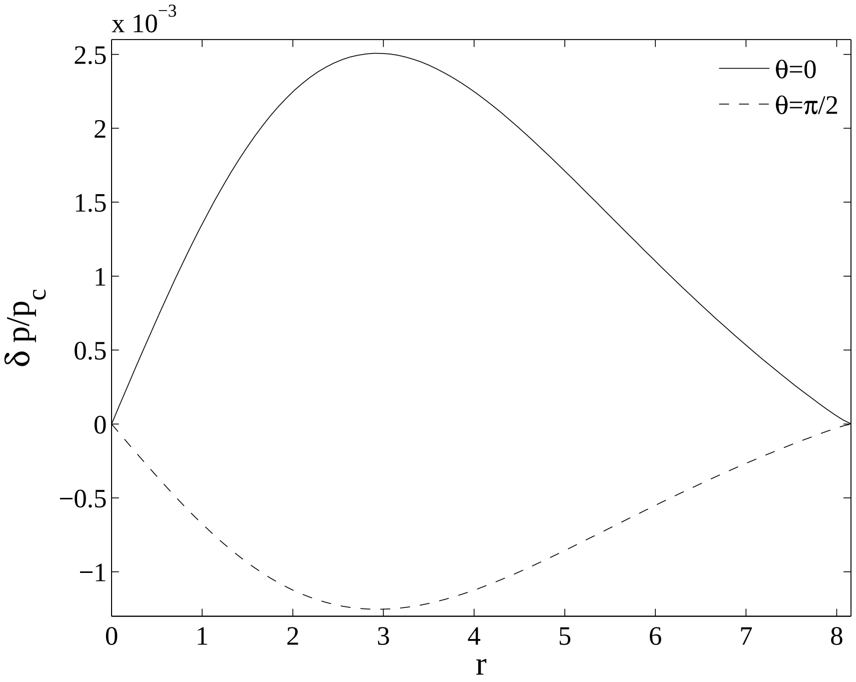

Figure 6.2: Profile of the relative initial pressure perturbation $\delta p/p_c$ [computed on the z-axis ($\theta = 0$) and on the xy-plane ($\theta = \pi/2$)] obtained from Eq. (6.3.1) and Eq. (6.3.2) with $n = 0$ and $\lambda = \lambda 0$.

Since the perturbative equations are more conveniently written in terms of enthalpy perturbations, the pressure perturbation is re-written in terms of this quantity. The initial pressure perturbation is chosen with an axisymmetric angular pattern like

$$\delta p(r, \theta) \equiv (p + \varepsilon) H_{\ell 0}(r) Y_{\ell 0}(\theta) \ , \tag{6.3.1}$$

where the radial profile is instead specified trough the relativistic enthalpy perturbation $H_{\ell 0}(r)$. Since, to the aim of comparing waveforms, the best system is represented by a star oscillating at only one frequency, we set a profile of $H_{\ell 0}(r)$ that excites, mostly, the f-mode of the star (with a small contribution from the first overtone). As suggested in Ref. [140], an "approximate eigenfunction" for a given fluid mode can be given by setting

$$H_{\ell 0} = \lambda \sin \left[\frac{(n+1)\pi r}{2R} \right] \tag{6.3.2}$$

where n is an integer controlling the number of nodes of $H_{\ell 0}(r)$, λ is the amplitude of the perturbation and R is the radius of the star in Schwarzschild coordinates. The case $n = 0$ has no nodes (*i.e.* no zeros) for $0 < r \leq R$; as a result, the f-mode is predominantly triggered and the p-mode contribution is negligible. If $n = 1$, the f-mode is still dominant, but a non-negligible contribution of the p_1-mode is present. If $n = 2$, in addition to the fundamental and

Table 6.4: Minimum and maximum value of the initial pressure perturbation for different values of the amplitude of the enthalpy perturbation (λ, see Eq. (6.3.2) with $n = 0$ and $\ell = 2$). The minimum pressure perturbation occurs at some value of r on the xy-plane ($\theta = \pi/2$), while the maximum pressure perturbation is found at some value of r on the z-axis ($\theta = 0$). (See Fig. 6.2)

Name	λ	$\min(\delta p/p_c)$	$\max(\delta p/p_c)$
$\lambda 0$	0.001	-0.00125	0.00251
$\lambda 1$	0.01	-0.01253	0.02506
$\lambda 2$	0.05	-0.06266	0.12533
$\lambda 3$	0.1	-0.12533	0.25067

the first pressure modes also the p_2 mode is clearly present in the signal. For higher values of n more and more overtones are excited.

We stress again that the same setup, Eq. (6.3.2), is used to provide initial data in both the linear and nonlinear codes. Correspondingly, the computation of δp is needed to get a handle on the magnitude of the deviation from sphericity. The best indicator is given by the ratio $\delta p/p_c$, where p_c is the central pressure of the star. Fig. 6.2 displays the profile of $\delta p/p_c$, at the pole and at the equator, as a function of the Schwarzschild radial coordinate r for $\lambda = \lambda 0 = 0.001$. For simplicity, we consider only $n = 0$ perturbations, with four values for the amplitude, namely $\lambda = \{0.001, 0.01, 0.05, 0.1\}$, in order to see, in the 3D code, how the transition from linear to nonlinear regime occurs. Maxima and minima of the initial pressure perturbation for the different values of the initial perturbation amplitude λ can be found in Tab. 6.4.

The metric perturbations are set in the PERBACCO imposing the condition $S(r) = 0$ and $\dot{k}_{20} = \dot{\chi}_{20} = 0$, exactly as described in Sec. 3.3.1 for initial data of type 1. The initial data described in this section differ from type 1 initial data of Sec. 3.3.1 only for a slightly different prescription of $H_{\ell m}$, see Eq. (6.3.2). We stress that the condition $\dot{k}_{20} = \dot{\chi}_{20} = 0$ is imposed for simplicity, but we are aware that this is inconsistent with the condition that, initially, $H_{20} \neq 0$ and thus the momentum constraints should also be solved. However, since the effect is a small initial transient in the waveforms that quickly washes out before the quasi-harmonic oscillation triggered by the perturbation H_{20} sets in, we have decided to maintain the initial data setup simple. Fig. 6.3 synthesizes the information about the initial data: it exhibits (as a solid line) the profile of k_{20} (versus Schwarzschild radius) corresponding to the perturbation $\lambda = \lambda 0$ of Tab. 6.4 that results from the solution of the Hamiltonian constraint. The corresponding initial Zerilli-Moncrief function, $\Psi^{(\mathrm{e})}_{20}$, outside the star is plotted in Fig. 6.3.

The initial data setup in the 3D code is done by a specific *thorn* called `Whisky_PerturbTOV`. In this case the procedure is more complicated as one needs to reconstruct the full 3D metric on the Cartesian grid. In addition, the main difference with respect to the 1D case is that the perturbative constraints are expressed using a radial *isotropic* coordinate $\bar{r}$ instead of the Schwarzschild-like radial coordinate r. This is done because $\bar{r}$ is naturally connected to the

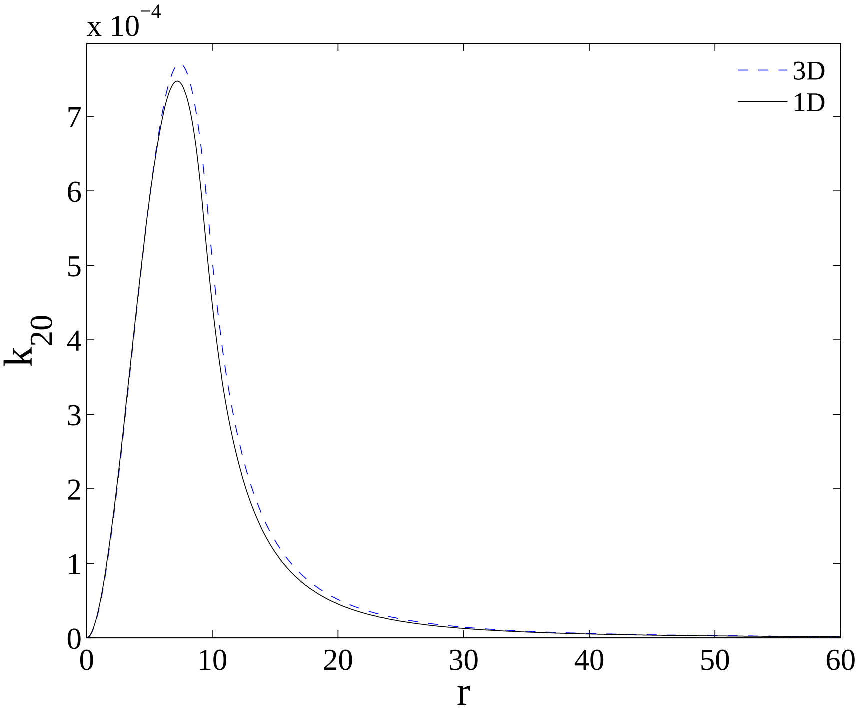

Figure 6.3: Initial-data setup in the 1D and 3D codes. Profiles of the k_{20} multipole at $t = 0$ versus the Schwarzschild radial coordinate r, obtained from the solution of the perturbative Hamiltonian constraint with $\lambda = \lambda 0$ and $n = 0$.

Cartesian coordinates in which the code is expressed, *i.e.* $\bar{r} = \sqrt{x^2 + y^2 + z^2}$. The initialization of the metric in the 3D case has to follow four main steps: (i) The perturbative constraints are solved, (ii) The multipolar metric components are added to the unperturbed background TOV metric; (iii) The resulting metric is written in Cartesian coordinates; (iv) It is interpolated on the Cartesian grid.

In terms of the isotropic radius (See Eq. (2.4.5)), the perturbative Hamiltonian constraint explicitly reads

$$k^{\ell m}_{,\bar{r}\bar{r}} + \frac{k^{\ell m}_{,\bar{r}}}{\bar{r}}\left[1 + \left(1 - \frac{2m(r)}{r}\right)^{1/2}\right] + e^{2b}\left(8\pi e - \frac{\Lambda}{r^2}\right)k^{\ell m} - \frac{1}{\bar{r}}\left(1 - \frac{2m(r)}{r}\right)^{1/2}\chi^{\ell m}_{,\bar{r}}$$
$$- e^{2b}\left(\frac{\Lambda + 2}{2r^2} - 8\pi e\right)\chi^{\ell m} = -\frac{8\pi(p+e)H^{\ell m}}{C_s^2}\ , \qquad (6.3.3)$$

where $r \equiv r(\bar{r})$ according to Eq. (2.4.5a) and Eq. (2.4.5c). Eq. (6.3.3) is solved for $k_{\ell m}$ imposing the conformal-flatness condition $\chi_{\ell m} = 0$.

As discussed in Sec. 3.2 the multipole $\psi_{\ell m}$ is obtained from $k_{\ell m}$ and $\chi_{\ell m}$. In the absence of azimuthal and tangential velocity perturbations, in Schwarzschild coordinates and in the Regge-Wheeler gauge, from the momentum-constraint

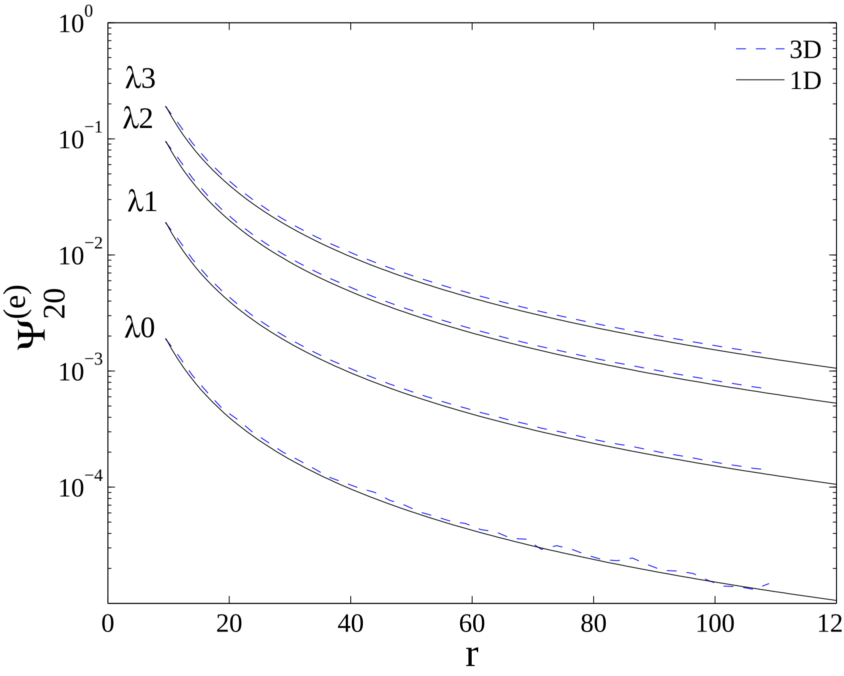

Figure 6.4: Initial-data setup in the 1D and 3D codes. Profiles of $\Psi^{(e)}_{20}$ at $t = 0$ versus the Schwarzschild radial coordinate r, for different values of the initial perturbation λ.

equation, namely Eq. (95) of Ref. [101], the relation is

$$\psi_{\ell m,r} = -\frac{2\left[m(r) + 4\pi r^3 p(r)\right]}{r - 2m(r)}\psi \ , \tag{6.3.4}$$

which, once solved, gives

$$\psi_{\ell m}(r) = \tilde{C}\exp\left[-\int_0^r dx \frac{2\left(m(x) + 4\pi x^3 p(x)\right)}{x - 2m(x)}\right] . \tag{6.3.5}$$

The requirement $\psi_{\ell m} \to 0$ for large r, like for $k_{\ell m}$, implies $\tilde{C} = 0$. Therefore, the metric perturbation is (See Eq. (3.2.1), Eq. (2.4.4) and Eq. (2.4.5))

$$\begin{aligned} \delta s^2_{\ell m} =& \big\{(\chi_{\ell m} + k_{\ell m})e^{2a}dt^2 - 2\psi_{\ell m}e^{a+b}dtd\bar{r} \\ &+ e^{2b}\left[(\chi_{\ell m} + k_{\ell m})d\bar{r}^2 + \bar{r}^2 k_{\ell m}d\Omega\right]\big\}Y_{\ell m} \ . \end{aligned} \tag{6.3.6}$$

with $\psi_{\ell m} = \chi_{\ell m} = 0$. The full metric in isotropic coordinates is obtained as $ds^2 = d\mathring{s}^2 + \delta s^2_{\ell m}$. This metric is transformed to Cartesian coordinates and then it is linearly interpolated onto the Cartesian grid used to solve the coupled Einstein-matter equations numerically. To ensure a correct implementation of the boundary conditions (*i.e.* $k_{\ell m} \to 0$ when $\bar{r} \to \infty$), the isotropic radial grid used to solve Eq. (6.3.3) is much larger ($\bar{r} \sim 3000$) than the corresponding Cartesian grid ($\bar{r} \sim 208$) and the spacing is much smaller.

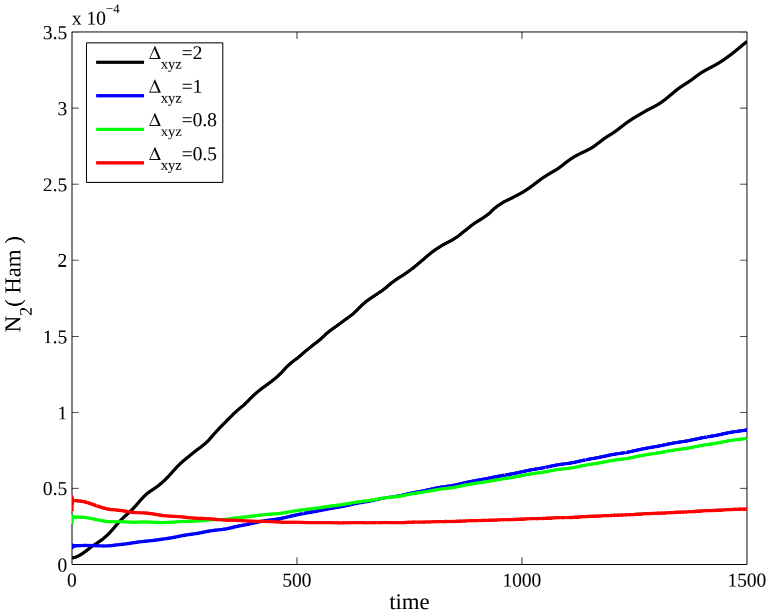

Figure 6.5: Convergence test of the 3D simulations. The l^2 norm of the Hamiltonian constraint is showed versus time for different grid resolutions. The plot show the correct convergence in time and that, at the best resolution, the Hamiltonian constraint is preserved.

One proceeds similarly also for the matter perturbation: from a given profile $H_{\ell m}(r)$ the pressure perturbation $\delta p(r,\theta)$ is computed and from this the total pressure is given by $p+\delta p$. This is interpolated on the Cartesian grid to finally obtain the vector of the conserved hydrodynamics variables $\vec{q}$.

The consistency of the initial-data setup procedure in both the PERBACCO 1D linear code and in the `CACTUS-CARPET-CCATIE-Whisky` 3D nonlinear code is highlighted in Fig. 6.3 and Fig. 6.4. Fig. 6.3 shows the profiles of k_{20} in the 1D case (solid line) and in the 3D case (dashed line) for $\lambda = \lambda 0$ and $n = 0$. The small differences are related to a slightly different location of the star surface in the two setups and to the different resolution of the grids. Fig. 6.4 contrasts the Zerilli-Moncrief functions $\Psi^{(e)}_{20}$ from the 1D code (solid lines) with those extracted (at $t = 0$) from the numerical 3D metric (dashed lines). For all initial conditions, the curves show good consistency.

The 3D simulations we are going to discuss are performed over grids with three refinement levels and cubic boxes with limits $[-120, 120]$, $[-24, 24]$ and $[-12, 12]$ in each direction. The resolutions of each box are respectively $\Delta_{xyz} =$ 0.5, 0.25 and 0.125. Equations are evolved only on the first octant of the grid and symmetry conditions are applied. The outermost detector is located at isotropic-coordinate radius $\bar{r} = 110$ ($\sim 80M$). We performed also simulations with the (coarsest) grid spacing set at $\Delta_{xyz} = 0.8$, $\Delta_{xyz} = 1$ and $\Delta_{xyz} = 2$ in order to check the proper convergence of the 3D results. In Fig. 6.5 it is plotted the l^2 norm, *i.e.*

$$\mathcal{N}_2(f) \equiv \frac{1}{J}\sqrt{\sum_{j=1}^{J} f_j^2} \tag{6.3.7}$$

where f is the time series, of the Hamiltonian constraint for different grid resolutions. Simulations are second order convergent in time and, for the best resolution, the violation of the Hamiltonian constraint remains almost constant at its initial value.

In Sec. 4.3.3 we had clearly assessed the characteristic and the accuracy of the waveforms computed via the PerBaCCo . In the following we shall consider these waveforms (extracted at the farthest observer) as “exact” for all practical purposes an we compare them with the waveforms extracted from the 3D nonlinear simulations. Actually we limit our study to $\ell = 2$ (quadrupole) perturbations and we explore a range of values for the initial perturbation λ in order to capture the transition from the linear to the nonlinear the regime.

6.4 Abrahams-Price extraction: results

In this section we discuss the metric waveforms extracted from the 3D code with the technique outlined in Sec. 5.1 and we compare them to the exact, perturbative results for different values of the initial perturbation amplitude λ.

Fig. 6.6 is obtained with initial perturbation amplitude $\lambda = \lambda 1$. It displays the Zerilli-Moncrief normalized metric waveforms, extracted on coordinate spheres of radii $\bar{r} \in \{30,\ 60,\ 90,\ 110\}$ and plotted versus the (approximate) retarded time $u = t - r_*$. Here, r is the areal radius of the spheres of coordinate radius $\bar{r}$ and M is the Schwarzschild mass enclosed in $\bar{r}$ [2, 8, 157]. This figure is the 3D analogous of Fig. 4.19. The 1D and 3D waveforms look qualitatively very similar apart from the presence of a highly-damped, high-frequency oscillation at early times. In Sec. 6.6 we will argue that this oscillation is essentially unphysical because its amplitude grows linearly with the extraction radius $\bar{r}$, instead of approaching an approximately constant value (as it happens instead for the subsequent fluid-mode oscillations). Sec. 6.6 is devoted to a throughout discussion of these issues; for the moment, we simply ignore this problem and focus our attention only on the part of the waveform dominated by fluid modes.

Each panel of Fig. 6.7 compares the 1D, exact, $\Psi^{(\mathrm{e})}_{20}$ (dashed lines) with that computed via the 3D code (solid lines) for the four values of the initial perturbation amplitude λ. The extraction radius is (in both codes) $\bar{r} = 110$ and this implies that a non-zero, constant offset for $u \lesssim 0$ is present. Note, in this respect, the good consistency between 3D and 1D results for $u \lesssim 0$, confirming here the information enclosed in the bottom panel of Fig. 6.4. After the initial high-frequency (unphysical) oscillations, the top-left panel of Fig. 6.7 shows that an excellent agreement between waveforms is found when the perturbation is “small”. Then, for larger values of λ (until it assumes values that cannot be considered a perturbation anymore) the amplitude of the oscillation in the 3D simulations becomes smaller with respect to the linear case, suggesting that nonlinear couplings (specifically, couplings with overtones as well as couplings with the radial modes, see Sec. 6.8) are redistributing the energy of the $\ell = 2$, $m = 0$ oscillations triggered by the initial perturbation. In Sec. 6.8, we will

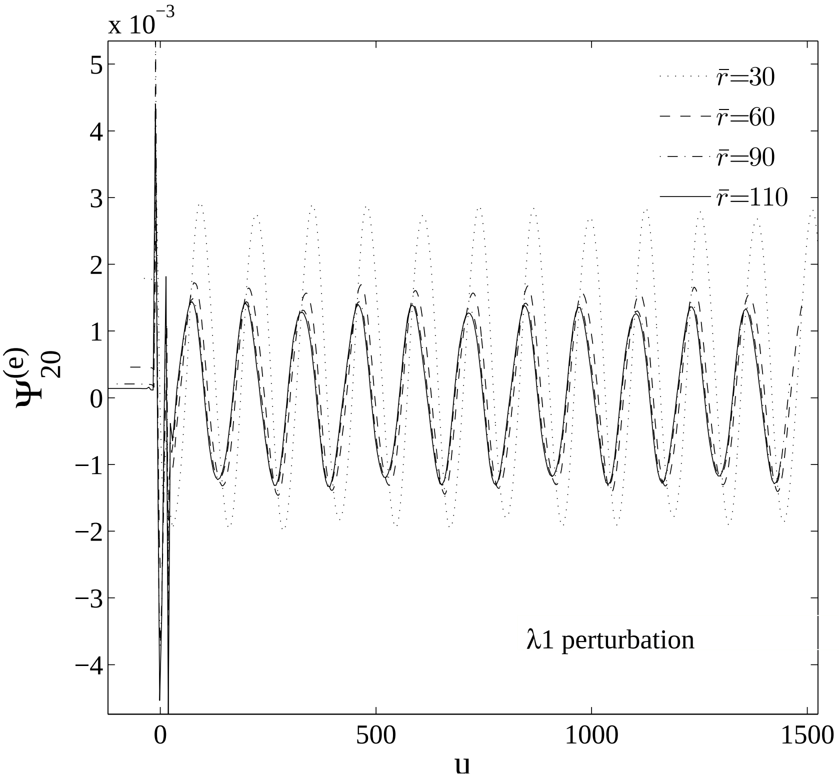

Figure 6.6: The Zerilli-Moncrief *metric* waveforms versus the observer retarded time u at different extraction radii ($\bar{r} = 30$ to $\bar{r} = 110$). These data refer to a 3D simulation with initial perturbation $\lambda = \lambda 1$. The initial part of the waveform is dominated by a pulse of "junk" radiation.

argue that couplings between modes become more and more relevant when the perturbation increases, giving a quantitative explanation to the phenomenology that we observe. This effect is summarized in Fig. 6.8, which displays the amplitude A_{20} obtained by fitting the waveform with the template Eq. (4.1.1) versus the magnitude of the perturbation for 1D (linear) and 3D (nonlinear) simulations. It is evident from the figure that there is a consistent deviation from linearity already when the perturbation is relatively small ($\lambda \lesssim 0.02$). As a measure of the global agreement between 1D and 3D waveforms (as a function of the initial perturbation λ) we list in Tab. 6.5 the l^2 residuals $\mathcal{R}(\Psi^{1\mathrm{D}}, \Psi^{3\mathrm{D}})$ and the l^∞ distances $\mathcal{D}(\Psi^{1\mathrm{D}}, \Psi^{3\mathrm{D}})$. The indexes confirm that the waves become progressively different for increasing λ.

The 3D waveforms for $\lambda 0$ and $\lambda 1$ turn out to be damped on a time scale of about 20 ms: this damping time is much shorter than the one of the f-mode or p_1-mode, as computed via the 1D approach. This "effective-viscosity" damping time τ^{visc} (that is related to the inverse of the viscosity) can be extracted by means of the fit analysis. We have found that τ^{visc} depends on the initial perturbation, being $\tau^{\mathrm{visc}} \simeq 0.022, 0.132, 0.203, 0.129$ s respectively for $\lambda = \lambda 0, \lambda 1, \lambda 2, \lambda 3$. The best agreement with the expected physical value of

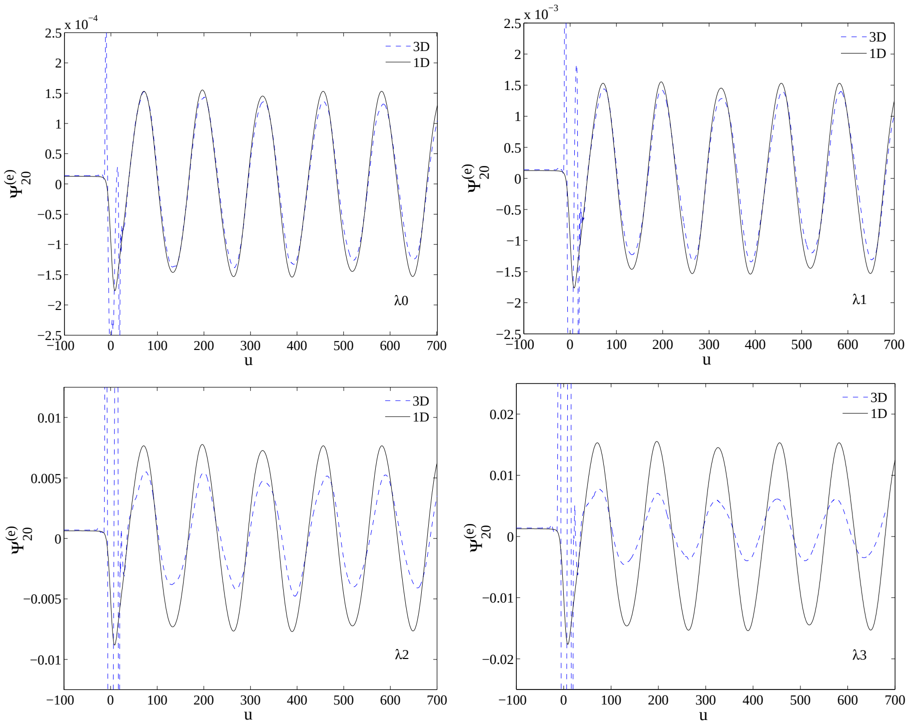

Figure 6.7: Metric waveforms extracted at $\bar{r} = 110$ computed from 3D simulations (dashed lines) and 1D linear simulations (solid lines) for different values of the initial perturbation amplitude λ. If λ is sufficiently small (*e.g.* , $\lambda \lesssim 0.01$) the outcomes of the two codes show good agreement. If the "perturbation" is large ($\lambda \sim 0.1$), nonlinear effects become dominating.

$\tau_{20} = 0.268$ s is obtained for $\lambda = \lambda 2$; both for larger and smaller perturbations the 3D results show even shorter damping times. The errors on these quantities are of the order of 0.5%. The interpretation of these results may include two different effects. The smaller damping time of the wave for the $\lambda = \lambda 3$ perturbation with respect to the $\lambda = \lambda 2$ one may be interpreted as due to the nonlinear couplings that allow the disexcitation of the fundamental mode in other channels; as it can be seen from Fig. 6.8 and Fig. 6.23, nonlinear effects are more and more important in the case of the $\lambda = \lambda 3$ perturbation. However, for perturbations smaller than $\lambda = \lambda 2$ the "effective viscosity" is not found to decrease towards the expected perturbative value, as it could have been expected from the above argument. This discrepancy might be due to the numerical viscosity proper of the evolution scheme. Such numerical viscosity would have a bigger influence in low-perturbation simulations, where the energy lost from the fundamental mode into other modes is smaller (while in higher-perturbation simulation the coupling of modes is the dominant effect).

Although the detailed analysis of the numerical viscosity of the 3D code is beyond the scope of the present work, we checked that, as expected, it depends on the grid resolution. During convergence test, in fact, we observed that, in

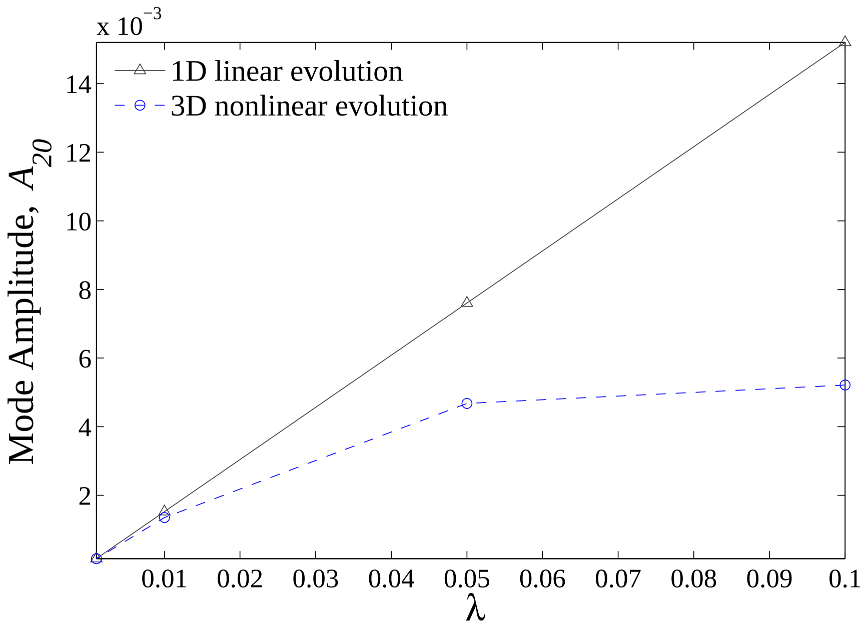

Figure 6.8: Comparison between the oscillation amplitude A_{20} (from fits) in the 1D (linear) and 3D (nonlinear) simulations versus the initial perturbation λ. Deviations from linearity are occurring already for very small values of λ.

the case of the coarsest grid ($\Delta_{xyz} = 2$), there was an initial "explosion" in the amplitude, then followed by a strong damping during the first five gravitational-wave cycles, as can be seen in Fig. 6.9. This shows that this resolution is not even sufficient to extract the qualitative behavior of the waveform. On the other hand, the other two resolutions did not show any qualitative difference in addition to the different value of the "effective viscosity", that decreases for higher resolutions.

The anomalous value of the damping times could be due also to the artificial atmosphere. Focusing only on the $\lambda 0$ perturbation, and varying the value of the rest-mass density of the atmosphere in the range $\rho_{\rm atm} = 10^{\{-5,-6,-7\}}\rho_{\max}$, we found any significant influence on the values of $\tau^{\rm visc}$.

Finally, we have also Fourier-transformed the 3D waveforms to extract the fluid-mode frequencies and we have compared them with the linear ones. This comparison is shown in Tab. 6.6. Apparently, the frequency of the f-mode (that dominates the signal) is less sensitive to nonlinear effects than its amplitude, as it can be seen from the fact that only the $\lambda 3$ initial data are such to force the star to oscillate at a frequency slightly different from that of the linear approximation. On the other hand, the first overtone (the p_1-mode) seems more sensitive. It is in any case remarkable that for $\lambda = \lambda 0$ and $\lambda = \lambda 1$ the frequencies from 3D and 1D simulations coincide at better than 1%, suggesting that the main gravitational-wave frequencies are only mildly affected by nonlinearities.

Table 6.5: Global-agreement measures computed on the interval $\Delta u = [50, 3000]$ (after the "junk" burst) at the outermost detector. Here, $\mathcal{R}(\Psi^{1\mathrm{D}}, \Psi^{3\mathrm{D}})$ and $\mathcal{D}(\Psi^{1\mathrm{D}}, \Psi^{3\mathrm{D}})$ are defined in Eq. (4.1.2) and in Eq. (4.1.3).

λ	$\mathcal{R}$	$\mathcal{D}$
$\lambda 0$	3.07×10^{-2}	7.93×10^{-5}
$\lambda 1$	4.88×10^{-2}	7.79×10^{-4}
$\lambda 2$	1.63×10^{-1}	2.78×10^{-3}
$\lambda 3$	9.96×10^{-1}	2.04×10^{-2}

Table 6.6: Fourier analysis of the 3D waveforms (See Fig. 6.7) over the interval $u \in [50,\ 3000]$. The frequencies from 1D simulations are $\nu_f^{1\mathrm{D}} = 1581$ Hz and $\nu_{p_1}^{1\mathrm{D}} = 3724$ Hz. From left to right the columns report the type of perturbation, the f-mode frequency, its relative difference with the 1D value, the p_1-mode frequency and its relative difference with the 1D value.

λ	$\nu_f^{3\mathrm{D}}$ [Hz]	Diff.[%]	$\nu_{p_1}^{3\mathrm{D}}$ [Hz]	Diff.[%]
$\lambda 0$	1578	0.2	3705	0.5
$\lambda 1$	1576	0.3	3705	0.5
$\lambda 2$	1573	0.5	3635	2.4
$\lambda 3$	1623	2.7	3565	4.3

6.5 Newman-Penrose extraction: results

This section is devoted to the comparison between 1D and 3D *curvature* waveforms.

In the PerBaCCo one can use the relation

$$r\psi_4^{\ell m} = r\ddot{h}^{\ell m} = N_\ell \left(\ddot{\Psi}^{(\mathrm{e})}_{\ell m} + \mathrm{i}\ddot{\Psi}^{(\mathrm{o})}_{\ell m} \right) \tag{6.5.1}$$

to obtain the Newman-Penrose scalar (multiplied by the extraction radius) $r\psi_4^{\ell m}$ from the gauge-invariant metric master functions. Due to our choice of initial conditions, we shall consider only $\Psi^{(\mathrm{e})}_{20}$ in the following [1]. The second time-derivative of $\Psi^{(\mathrm{e})}_{20}$ can be computed via finite differencing, by applying twice a first-order derivative operator of 2nd or 4th-order accuracy.

By contrast, in the 3D code ψ_4^{20} is extracted independently of the metric waveform. Then, one computes $r\psi_4^{20}$ where r is an approximated radius [2] Schwarzschild-like radial coordinate obtained from Eq. (2.4.5a) with $M = 1.4$.

Fig. 6.10 displays the $r\psi_4^{20}$ waveforms from 1D (solid line) and 3D (dashed line) evolutions of initial perturbation amplitude $\lambda = \lambda 0$. The extraction radius is $\bar{r} = 110$ in both codes. Visual inspection of the figure immediately suggests that: (i) The initial transient in the 1D metric waveform preceding the setting

---

[1] Note that in principle one could compute ψ_4 independently, solving the Bardeen-Press-Teukolsky equation [159].

[2] This is an approximate relation as $\bar{r}$ is a coordinate radius and the mass inside the sphere of radius $\bar{r}$ is time dependent. We neglect all this higher order effects here as this approximation is sufficiently accurate for our purposes.

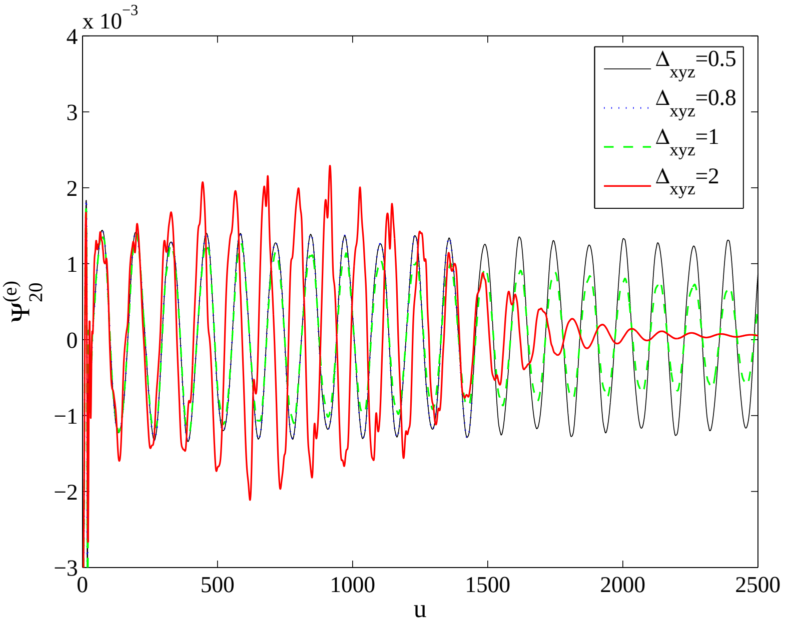

Figure 6.9: Metric waveform extracted at $\bar{r} = 110$ computed from 3D nonlinear simulations using different grid resolutions. The grid spacing Δ_{xyz} refers to the coarsest refinement level. The initial perturbation amplitude in these simulations is $\lambda = \lambda 1$.

in of the quasi-harmonic f-mode oscillation results in a highly damped, high-frequency oscillation; (ii) The initial transient radiation has the same qualitative shape in both the 1D and 3D waveforms, although the amplitude of the oscillation is larger in the latter case. At this point one should note that: (i) In the 1D case, although the conformally flat condition is imposed at $t = 0$, the constraint is solved numerically and thus a small violation of this condition occurs; (ii) The violation is expected to be larger in the 3D case, because of the larger truncation errors. It is in any case remarkable that, as the figure shows, these errors (*e.g.* the slightly different shape of k_{20}, the linear interpolation from spherical to Cartesian coordinates, etc.) are sufficiently under control to produce the same qualitative behavior besides small quantitative differences in the initial part of the 1D and 3D waveforms.

The question that occurs at this point is whether the violation of the conformally flat condition introduces some amount of physical w-mode excitation in the waveforms. To answer this question we show in Fig. 6.11 the Fourier Power Spectral Density (PSD) of the $r\psi_4^{20}$ waveforms of Fig. 6.10. The PSD is computed all over the waveform and not only during the ring-down, due to the difficulty of separating reliably this part from the precursor [44]. We are aware, see Chap. 4, of the problems related to the precise determination the w-modes frequencies and their location in the waveform (See also Refs. [44, 147]), and in particular of the fact that the Fourier analysis can not provide accurate and definitive answers, essentially because, in the presence of damped signals with frequency comparable to the damping time, the Fourier spectrum results

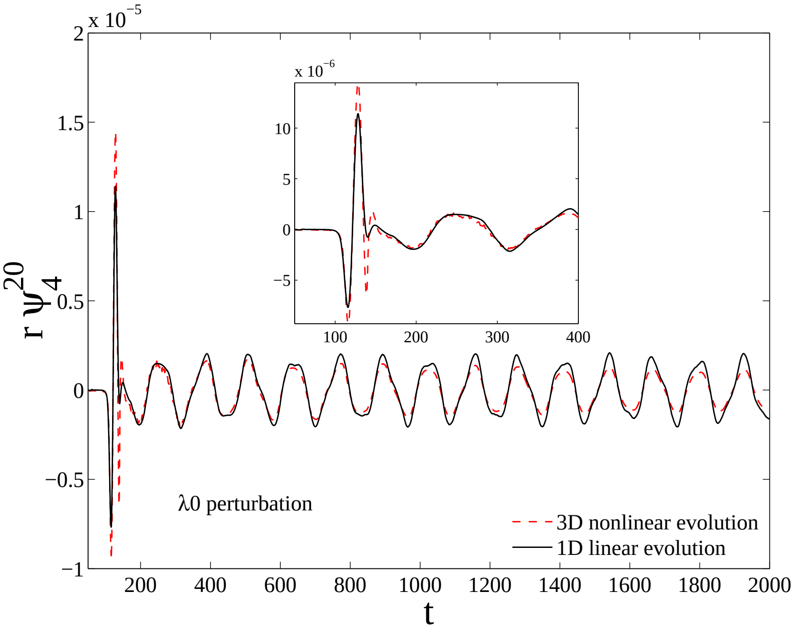

Figure 6.10: Curvature waveforms extracted at $\bar{r} = 110$ computed from 3D simulations (dashed lines) and 1D linear simulations (solid line) for the initial perturbation amplitude $\lambda = \lambda 0$. The initial transient is consistent between the two evolutions. The inset concentrates on the initial part of the waveform.

in a broad peak. However it represents a fundamental part of the analysis and, in the present case, is preferable to a fitting procedure because of the already mentioned problem of separating the precursor from the ring-down part.

The dashed-dotted vertical lines of Fig. 6.11 locate the first two w-mode frequencies of this model, $\nu_{w_1} = 10.09$ kHz and $\nu_{w_2} = 17.84$ kHz [3] Two of the maxima of the PSD of the 3D $r\psi_4^{20}$ waveform can be associated to the frequencies ν_{w_1} and ν_{w_2}, even if they are in a region very close to the noise. The frequency ν_{w_1} is probably slightly excited also in the 1D case (See inset), while only noise is present around ν_{w_2}. In Fig. 6.11 we exhibit also the PSD of the 1D $\Psi_{20}^{(e)}$ (dashed dark line) and the one of the 3D $\Psi_{20}^{(e)}$ (dashed light line) obtained from the double time-integration of ψ_4^{20}. In both cases, it is not possible to disentangle ν_{w_1} and ν_{w_2} from the background noise.

The fact that a signal characterized by highly damped modes is much less evident in the PSD of the metric waveform than in the corresponding curvature one is simply due to the second derivative that relates the two gauge-invariant functions. When spacetime modes are excited, the metric waveform is (approximately) composed by a pure ring-down part plus a tail contribution [164], that is $\Psi_{20}^{(e)} \approx e^{-\sigma t} + \beta t^{-7}$, where $\sigma = \alpha + i\omega$ (α is the inverse of the damping time

---

[3] These frequencies have been kindly computed by K. Kokkotas and N. Stergioulas via an independent frequency domain code for this specific comparison.

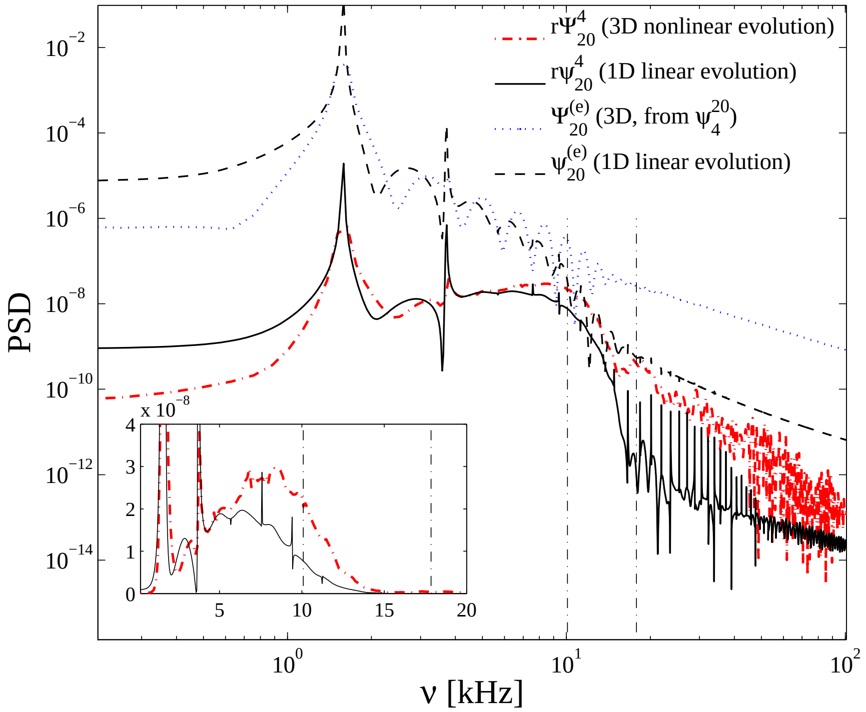

Figure 6.11: Comparison of the PSD of various waveforms. The PSD of the $r\psi_4^{20}$ and $\Psi^{(e)}_{20}$ from the 1D code are compared with those from the 3D code, obtained after integration. The initial perturbation is $\lambda = \lambda 0$. The w-modes frequencies w_1 and w_2 are superposed to the spectra as vertical dot-dashed lines. See text for discussions.

and ω the w-mode frequency) and β is a numerical coefficient. When one takes two time derivatives to compute $r\psi_4^{20}$ from $\Psi^{(e)}_{20}$, the tail contribution is suppressed by a factor t^{-2} and the oscillatory part of the waveform emerges more sharply.

This comparison suggests that the best way to extract information about w-modes (especially when their contribution is small) is, in general, to look at $r\psi_4^{\ell m}$. In addition, it also highlights that, while it is not possible to exclude the presence of w-modes in the $r\psi_4^{\ell m}$ signal due to the small violation of the conformally flat condition at $t = 0$, at the same time we can not definitely demonstrate that those high frequencies present near the noise are attributable to w-modes. In the next section we are going to show similar analyses on the spectra computed from $\Psi^{(e)}_{20}$ waveforms extracted á la Abrahams-Price from the 3D simulation.

Finally, the global-agreement measures on the ψ_4 extraction are $\mathcal{R} \simeq 1.42 \times 10^{-2}$ and $\mathcal{D} \simeq 9.09 \times 10^{-7}$, which highlight some differences between the linear and the nonlinear approach.

The analysis discussed so far indicates that, in the present framework, the wave-extraction procedure based on the Newman-Penrose scalar ψ_4 seems to produce

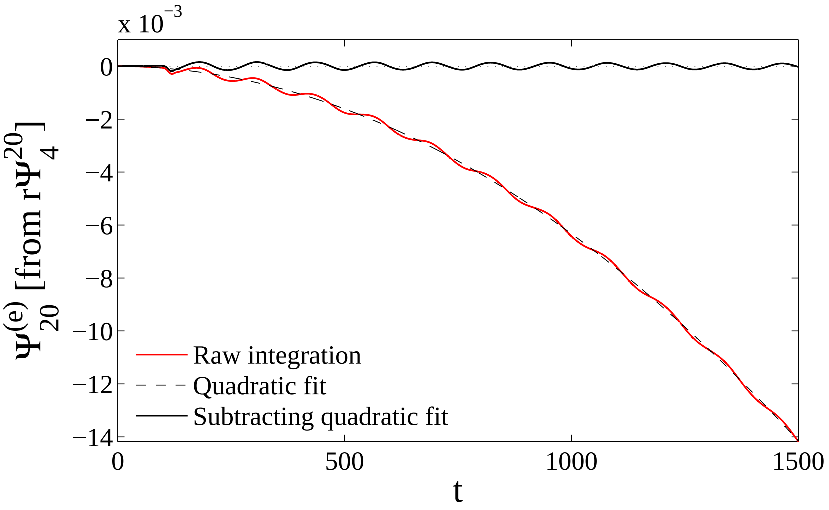

Figure 6.12: Recovery of $\Psi^{(\mathrm{e})}_{20}$ from two successive time integrations of $r\psi^{20}_4$ extracted from the 3D simulation with initial perturbation $\lambda = \lambda 0$. After the subtraction of a quadratic "floor" the waveform correctly oscillates around zero.

waveforms that, especially at early times, are more accurate than the corresponding ones extracted via the Abrahams-Price metric-perturbation approach. However, one of the big advantages of the latter method is that the waveforms h_+ and $h_\times$ are directly available at the end of the computation, and thus ready to be injected in some gravitational-wave–data-analysis procedure. By contrast, if one prefers to use Newman-Penrose wave-extraction procedures (which are the most common tools employed in numerical-relativity simulations nowadays), a consistent give prescription to obtain $\Psi^{(\mathrm{e/o})}_{\ell m}$ from $\psi_4^{\ell m}$ must be given. To do so, one needs to perform a double (numerical) time integration, with at least two free integration constants to be determined to correctly represent the physics of the system.

Inverting Eq. (6.5.1) following the considerations of Sec. 5.2.1, we obtain the following result (See Eq. (5.2.11))

$$
\begin{aligned}
rh^{\ell m} &= N_\ell \left(\Psi^{(\mathrm{e})}_{\ell m} + \mathrm{i}\Psi^{(\mathrm{o})}_{\ell m}\right) \\
&= \int_0^t dt' \int_0^{t'} dt'' r\psi^4_{\ell m}(t'') + Q_0 + Q_1 t + Q_2 t^2 \ , \\
&= r\tilde{h}_{\ell m}(t) + Q_0 + Q_1 t + Q_2 t^2 \ ,
\end{aligned} \tag{6.5.2}
$$

where Q_0, Q_1 and Q_2 are (still) undetermined integration constants, which are complex if $m \neq 0$. Note that this relation does not involve the Q_2 integration constant only if finite-radius extraction effects can be considered negligible (See below). Our aim is to recover the metric waveform that corresponds to the 3D $r\psi_4^{20}$ waveform that we have characterized above.

To do this let's consider the waveform of Fig. 6.10 up to $t = 1500$, where the reduction in amplitude due to numerical viscosity is already of the order of 30%

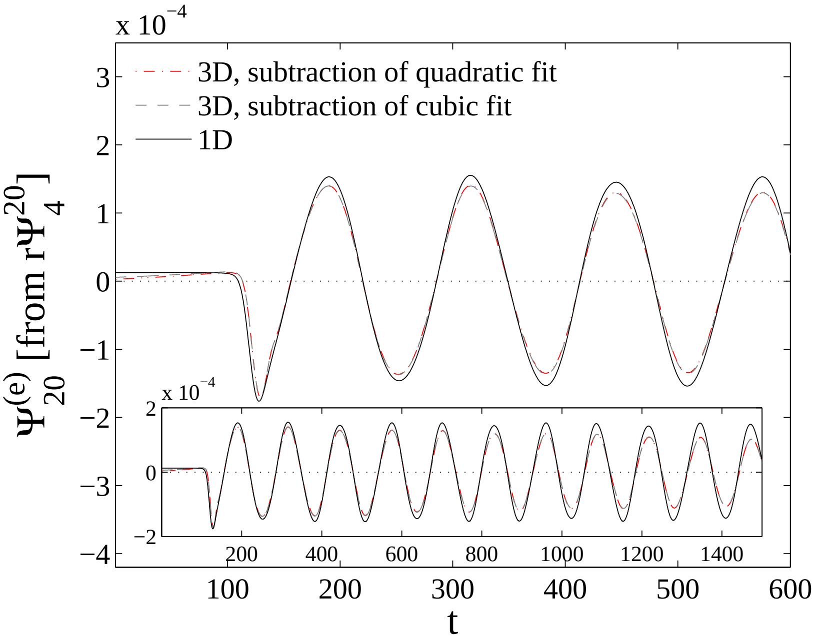

Figure 6.13: Selecting the best fitting function for the 3D integrated-and-subtracted metric waveform. The dash-dotted line refers to the curve obtained with the subtraction of a cubic fit and the dashed line to the curve obtained with the subtraction of a quadratic fit. They very similar to each other and to the 1D waveform (solid line). Contrary to the case of the extracted metric waveform, no initial burst of radiation is present in the 3D integrated-and-subtracted waveform.

with respect to the "exact" linear waveform. This sampled curvature waveform can be integrated twice in time, from $t = 0$ without fixing any integration constant to obtain $r\tilde{h}_{\ell m}(t)$. The raw result of this double integration is shown in Fig. 6.12. The "average" of the oscillation does not lay on a straight line, as it does instead in the case of the waveforms of binary black-hole coalescence discussed in Ref. [74], but it rather shows also a quadratic correction due to the finite extraction radius (See discussion in Sec. 5.2.1).

Indeed, when a "floor" of the form $P(t) = Q_0 + Q_1 t + Q_2 t^2$ is subtracted, the resulting metric waveform is found to oscillate around zero, as it can be seen in Fig. 6.12 and Fig. 6.13, which focuses on the beginning of the oscillation. The values of the coefficients of $P(t)$ obtained from the fit are $Q_0 = -4.338 \times 10^{-7}$, $Q_1 = -1.2462 \times 10^{-7}$ and $Q_2 = -6.2046 \times 10^{-9}$. The fact that $Q_0 < 0$ is connected to the choice of initial data we made (*i.e.* $k_{20} \neq 0$ at $t = 0$). Then, $Q_1 \neq 0$ indicates that the system is (slightly) out of equilibrium already at $t = 0$ and it is thus emitting gravitational waves since $\dot{\Psi}^{(e)}_{20}(0) \neq 0$. This is consistent with the choice of initial data we made, that is a perturbation that appears instantaneously at $t = 0$ without any radiative field obtained from the solution of the momentum constraint (since we use time-symmetric initial perturbations, for which $\dot{k}_{20} = \dot{\chi}_{20} = 0$).

The robustness of the quadratic fit can be tested by adding a cubic term $Q_3 t^3$ to $P(t)$ and then fitting again. In Fig. 6.13, a comparison of the 3D $\Psi^{(\mathrm{e})}_{20}$ waveform corrected with a cubic fit (dashed line) and the one corrected with a quadratic fit (dash-dotted line) with the "exact" 1D metric waveform (solid line) output by the PERBACCO is presented. Note that the 1D waveform has been suitably time-shifted in order to be visually in phase with the others at the beginning of the simulation. The figure suggests that the effect of the cubic correction is almost negligible (one only finds slight changes in the very early part of the waveform). The values of the fitting coefficients Q_i are: $Q_0 = -1.0096\times10^{-5}$, $Q_1 = -6.3331\times10^{-9}$, $Q_2 = -4.747\times10^{-8}$, $Q_3 = 6.7114\times10^{-14}$. The fact that Q_3 is many orders of magnitude smaller than the other coefficients is a good indication that the quadratic behavior is indeed the best choice here. Consistently with the curvature waveform of Fig. 6.10, we note the excellent agreement between 1D and 3D (integrated) metric waveforms also in the initial part of the waveform, *i.e.* up to $t \simeq 200$ (corresponding to the high-frequency oscillation in $r\psi_4^{20}$). Evidently, this is in contrast with the Abrahams-Price metric waveform in the top-left panel of Fig. 6.7. Finally, we point out that the coefficient $Q_2(r)$ shows, as expected, a clear trend towards zero for increasing values of the extraction radius.

6.6 Comparison between metric and curvature extraction

The analysis carried out so far suggests that both the Regge-Wheeler-Zerilli metric-based and the Newman-Penrose ψ_4-curvature-based wave-extraction techniques can be employed to extract reliable gravitational waveforms generated by compact self-gravitating system. For the particular case of an oscillating neutron star as considered here, both extraction methods allow to obtain waveforms that are in very good agreement with the linear results. Despite this success, the two approaches are not free from drawbacks.

Let us first focus on $r\psi_4^{\ell m}$ curvature waveforms. The comparison between 1D and 3D $r\psi_4^{20}$ waveforms in Fig. 6.10 (as well as between integrated metric waveforms in Fig. 6.13) shows good consistency between the two (as long as the effects of numerical viscosity on the evolution of the system remain negligible). As we mentioned above, an important information enclosed in Fig. 6.10 is that the differences between the high-frequency oscillations in the initial part of the waveforms (where w-modes are probably present in the 3D case) are "small". This fact makes us confident that the violation of the 3D Hamiltonian constraint at $t = 0$ (due to its approximate solution [4]) as well as the violation of the conformally flat condition are sufficiently negligible to avoid pathological behavior during evolution. A further confirmation of the accuracy of the evolution and of the curvature extraction is given by Fig. 6.14: the quantities $r\psi_4^{20}$ extracted at various radii ($\bar{r} \in \{30, 60, 90, 110\}$) and plotted versus retarded time are all superposed. This confirms the theoretical expectations of the peeling theorem [190] and indicates (once more) that the quantity $r\psi_4^{20}$ is accurately

---

[4] We recall that the 3D Hamiltonian constraint is solved at the linearized level on an isotropic grid and then the resulting metric perturbation is interpolated on the Cartesian grid. Typically, this procedure leads to larger errors than if solving the constraints directly on the Cartesian grid.

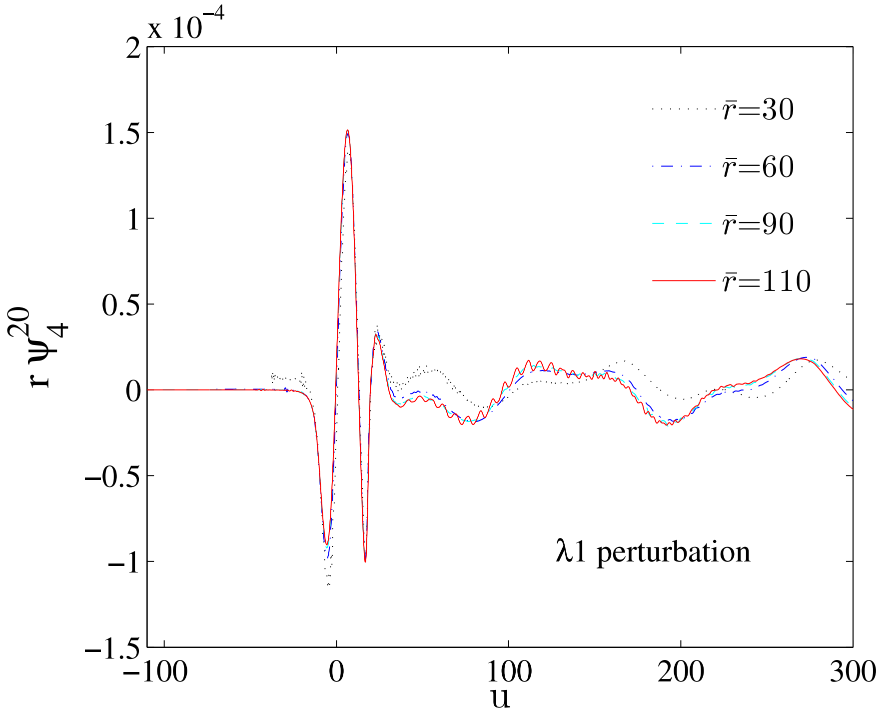

Figure 6.14: The waveforms $r\psi_4^{20}$ extracted at different radii are superposable (as expected from the "peeling" theorem). See text for further explanation.

computed. In Fig. 6.14, r is obtained from $\bar{r}$ via Eq. (2.4.5a). The retarded time is approximated with the standard r_*, where the constant mass $M = 1.4$ has been used.

The only subtle issue about $r\psi_4^{\ell m}$ seems to be the computation of the corresponding metric waveform via a double time integration. Although we were able to obtain a quite accurate metric waveform, the time-integration procedure (including the evaluation of the integration constants) may not be likewise straightforward in other physical settings.

The Abrahams-Price wave-extraction procedure, by contrast, directly produces the metric waveform and no time-integrations are needed. For this reason, it looks a priori more appealing than ψ_4 extraction. Unfortunately, the results presented so far (notably Fig. 6.7) indicate that this computation can be very delicate and can give unphysical results even in a very simple system like an oscillating polytropic star: we have found that $\Psi_{20}^{(\mathrm{e})}$ extracted in this way is unreliable at early times, because of the presence of high-frequency, highly damped oscillations, that are instead absent in both the 1D linear metric waveforms and the 3D metric waveforms time-integrated from $r\psi_4^{20}$. The unphysicalness of this initial "burst" of radiation is evident from Fig. 6.15, where the extractions at various radii $\bar{r} \in \{30, 60, 90, 110\}$ of the quantity $\Psi_{20}^{(\mathrm{e})}$ are compared: the amplitude grows with $\bar{r}$, instead of decreasing progressively to approach a constant value (as it is the case for the f-mode–dominated subsequent part of the waveform).

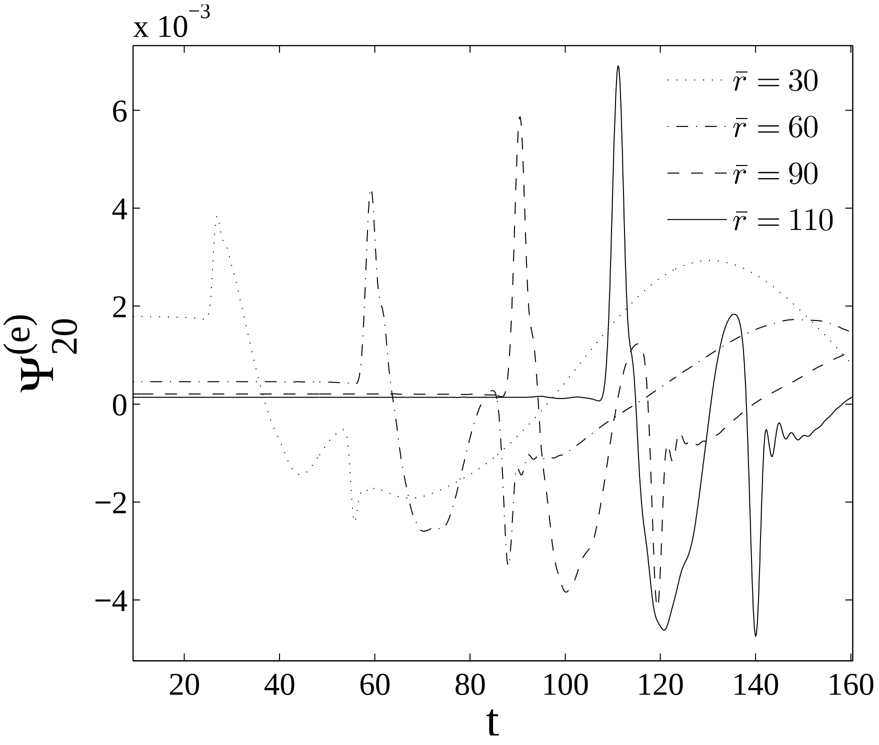

Figure 6.15: Metric waveforms computed via the Abrahams-Price procedure and extracted at different radii, for a 3D evolution with perturbation $\lambda = \lambda 0$. Note how the amplitude of the initial burst grows linearly with $\bar{r}$.

The weird behavior at early times of the extracted $\Psi^{(e)}_{20}$ indicates that this function does not satisfy the Zerilli equation in vacuum. Consistently, the perturbative Hamiltonian constraint in vacuum, Eq. (6.3.3) with $H_{20} = 0$, constructed from the 3D metric multipoles (χ_{20}, k_{20}), must be violated of some amount in correspondence of the "junk" [5]. This reasoning suggests that the "junk" may be the macroscopic manifestation of the inaccuracy in the initial-data setup at $t = 0$ (*i.e.* of solving the linearized Hamiltonian constraint first and then interpolating), possibly further amplified by the wave extraction procedure. This statement in itself looks confusing, because we have learned, from the analysis of ψ_4, that the Einstein (and matter) equations are accurately solved and that the errors made around $t = 0$ due to the violation of Hamiltonian constraint are relatively negligible. The relevant question is then: Is it possible that small numerical errors, almost negligible in $r\psi_4^{20}$, may be amplified in $\Psi^{(e)}_{20}$ at such a big level to produce totally nonsensical results? The following discussion proposes some heuristic explanation.

---

[5] The Zerilli equation, and thus the Zerilli-Moncrief master function, is obtained by combining together the perturbative Einstein equations, one of which is precisely the perturbative Hamiltonian constraint in vacuum. The Zerilli equation is satisfied if and only if the perturbative Hamiltonian constraint is satisfied too. See for example Ref. [135] for details.

To clarify the setup of our reasoning, let us first remind the reader of the basic elements of the Abrahams-Price metric wave-extraction procedure and, in particular, the role of Eq. (3.2.9). At a certain evolution time t, the numerical metric $g_{\mu\nu}(t)$ is known at a certain finite accuracy on the Cartesian grid. One selects coordinate extraction spheres of coordinate radius $\bar{r} = \sqrt{x^2 + y^2 + z^2}$ on which the metric is interpolated. Isotropic coordinate systems $(\bar{r}, \theta, \phi)$ naturally live on these spheres and thus one defines spherical harmonics. Then, the metric $g_{\mu\nu}$ is formally decomposed in a Schwarzschild "background " $\mathring{g}_{\mu\nu}$ plus a "perturbation" $\delta g_{\mu\nu}$. The next step is to choose a coordinate system in which the background metric is expressed. The standard approach is to use Schwarzschild coordinates, although this choice actually introduces systematic errors that may relevantly affect the waveforms. This has been recently demonstrated in Ref. [157]. Although we are aware of this fact, we prefer to neglect this source of error, on which we will further comment below. Choosing Schwarzschild coordinates means that one needs to compute a Schwarzschild radius r. This is given by the areal radius of the extraction 2-spheres. Proceeding further, $\delta g_{\mu\nu}$ is decomposed into seven (gauge-dependent) even-parity $(H_0, H_1, H_2, h_0^{(\mathrm{e})}, h_1^{(\mathrm{e})}, G, K)$ and three (gauge-dependent) odd-parity multipoles (that we don't consider here). From combinations of the seven even-parity multipoles and of their radial derivatives, see Eqs. (41) and (42) of Ref. [143], one obtains the gauge-invariant functions $k_{\ell m}$ and $\chi_{\ell m}$, as well as the derivative $\partial_r k_{\ell m}$. The last step is the computation of the Zerilli-Moncrief function via Eq. (3.2.9).

Various sources of errors are present. In particular, we mention the errors originating from: (i) The discretization of $g_{\mu\nu}$ (and its derivatives), from the numerical solution of Einstein's equations; (ii) The interpolation from the Cartesian grid to the isotropic grid; (iii) The computation of the metric multipoles via numerical integration over coordinate (gauge-dependent) 2-spheres. Our aim is to investigate how these inaccuracies on $(\chi_{\ell m}, k_{\ell m}, \partial_r k_{\ell m})$ can show up in $\Psi^{(\mathrm{e})}_{\ell m}$ at large extraction radii. In the limit $r \gg M$, Eq. (3.2.9) reads

$$\Psi^{(\mathrm{e})}_{\ell m} = \frac{2r}{\Lambda(\Lambda-2)}\left(\chi_{\ell m} - r\partial_r k_{\ell m} + \frac{\Lambda}{2}k_{\ell m}\right) , \tag{6.6.1}$$

that is

$$\Psi^{(\mathrm{e})}_{\ell m} \propto r Z_{\ell m} , \tag{6.6.2}$$

where $Z_{\ell m} = \chi_{\ell m} - r\partial_r k_{\ell m} + \Lambda/2 k_{\ell m}$ and r is the *areal* radius of the coordinate 2-spheres. The Abrahams-Price wave-extraction procedure introduces then errors both on r and $Z_{\ell m}$. In particular, the errors on the (gauge-invariant) multipoles $(\chi_{\ell m}, k_{\ell m}, \partial_r k_{\ell m})$ conspire in a global error on $Z_{\ell m}$. In a numerical simulation one has $Z_{\ell m} = Z^{\mathrm{Exact}}_{\ell m} + \delta Z_{\ell m}$ and $r = r^{\mathrm{Schw}} + \delta r$. Here $Z^{\mathrm{Exact}}_{\ell m}$ is computed from $(\chi^{\mathrm{Exact}}_{\ell m}, k^{\mathrm{Exact}}_{\ell m})$, that are solutions of the perturbation equation on a Schwarzschild background, and r^{Schw} is the radial Schwarzschild coordinates; $\delta Z_{\ell m}$ encompasses all possible errors due to the multipolar decomposition procedure, and δr various inaccuracies related to the determination of the areal radius (*e.g.* , those related to gauge effects). As a result, for the "extracted" Zerilli-Moncrief function we can write

$$\Psi^{(\mathrm{e})}_{\ell m} \approx \Psi^{\mathrm{Exact}}_{\ell m} + r^{\mathrm{Schw}}\delta Z_{\ell m} + \delta r Z^{\mathrm{Exact}}_{\ell m} . \tag{6.6.3}$$

This equation shows that, if $\delta Z_{\ell m}$ is not zero at a certain time (and does not decrease in time like $1/r^{\rm Schw}$) there is a contribution to the global error on $\Psi^{(\rm e)}_{\ell m}$ that grows with the extraction radius. This qualitative picture is consistent with what we observe in the 3D waveforms: A small error on δZ_{20} introduced at $t = 0$, because of the approximate solution of the constraints (as indicated by the analysis of $r\psi_4^{20}$ curvature waveforms), can show up as a burst of radiation whose amplitude increases linearly with the observer location. Note that what really counts here is the error budget at the level of $(\chi_{20}, k_{20}, \partial_r k_{20})$ and the related violation of the perturbative Hamiltonian constraint, Eq. (6.3.3). Indeed, it might occur that, even if the 3-metric γ_{ij} is very accurate and the constraints are well satisfied at this level, the extraction procedures adds other errors (for example due to the multipolar decomposition, computation of derivatives etc.) that may be eventually dominating in δZ_{20}. This observation may partially justify why $r\psi_4^{20}$ is well behaved, while $\Psi^{(\rm e)}_{20}$ is not. We finally note that in our simulation δr is typically very small, so that we have $r^{\rm Schw} \approx r$ with good accuracy.

Due to the complexity of the 3D wave-extraction algorithm, neither we were able to push forward our level of understanding, nor to precisely diagnose the cause of the aforementioned errors. By contrast, we can exploit the simpler computational framework offered by the 1D PERBACCO code to "tune" the error $\delta Z_{\ell m}$ in order to produce some initial "spurious" burst of radiation, and then possibly observe that its amplitude grows linearly with $\bar{r}$. In the 1D code δr is zero by construction, so that all errors are concentrated on $\delta Z_{\ell m}$. The constrained scheme adopted in the perturbative code allows to accurately compute the multipoles $(\chi_{\ell m}, k_{\ell m})$ at every time step, and the Hamiltonian constraint is satisfied by construction. Then, $\partial_r k_{\ell m}$ is obtained via direct numerical differentiation of $k_{\ell m}$. Consequently, the error δZ_{lm} depends on the resolution Δr as well as on the order of the finite-differencing representation of $\partial_r k_{\ell m}$.

In the following we shall analyze separately the effect of resolution and of the approximation scheme adopted for the numerical derivatives. First, we approximate $\partial_r k_{\ell m}$ with its standard first-order finite-differencing representation, *i.e.* $\partial_r k_{\ell m} \approx (k^{\ell m}_{j+1} - k^{\ell m}_{j})/\Delta r$ and we study the behavior of the "extracted" $\Psi^{(\rm e)}_{\ell m}$, computed using Eq. (3.2.9), versus extraction radius and resolution. Second, we use a fixed Δr, but we vary the accuracy of the finite differencing representation of $\partial_r k_{\ell m}$, contrasting first-order, second-order and fourth-order stencils. The results of these two analyses, for $\ell = 2$, $m = 0$, are exhibited in Fig. 6.16 and Fig. 6.17 respectively.

In the right panel of Fig. Fig. 6.16 $\partial_r k_{20}$ is approximated at first-order, with a resolution of $J_i = 10$ points inside the star ($\Delta r \sim 0.9$). This resolution approximately corresponds to the resolution of the coarsest refinement level used in the 3D code. The "extracted" waveform $\Psi^{(\rm e)}_{20}$ is shown at different observers, $\bar{r} \in \{30, 60, 90, 110\}$: an initial burst of "junk" radiation develops at early times and its amplitude grows linearly with the extraction radius (and it keeps growing for $\bar{r} > 110$). This behavior looks identical to that found in the 3D simulations. In the left panel of Fig. 6.16 we focus on $\bar{r} = 110$ only, but vary the number of radial points J_i inside the star, namely $J_i \in \{10, 20, 30, 40, 50, 100\}$. The figure shows that the initial "junk" is not present at higher resolutions ($J_i \geq 20$) and

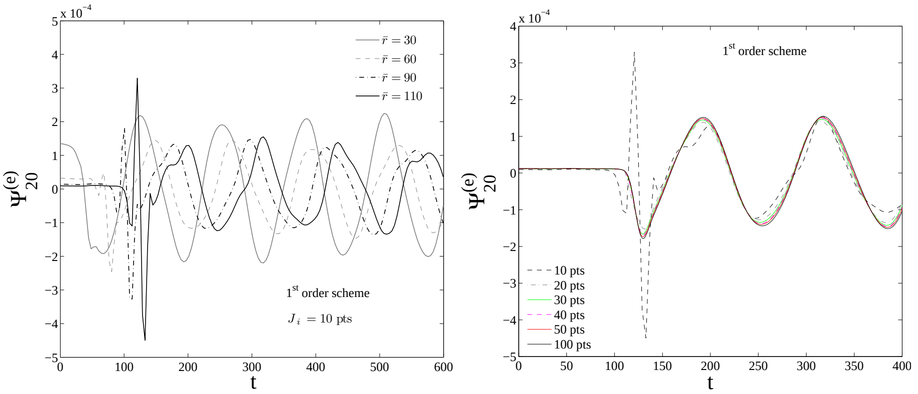

Figure 6.16: Metric waveforms from linear 1D evolutions. Right panel: Low resolution simulation. A burst of "junk" radiation at early times is present and its amplitude grows linearly with the extraction radius. Left panel: By increasing the resolution, the initial "junk" disappears.

that the waveform converges to the "exact" profile [6]. Let's note that varying the resolution shifts the occurrence of the burst at farther radii: observers at $\bar{r} \gg 110$ still see this burst appear and grow linearly with $\bar{r}$ if the resolution is not enough. To correctly extract waves it is so necessary to find the right balance between the extraction radius and the resolution.

A complementary analysis is shown in Fig. 6.17, where we fix the resolution at $J_i = 10$ (for $\bar{r} = 110$), but we change the accuracy of the numerical derivative $\partial_r k_{20}$. As expected, the initial "junk" disappears when the accuracy of the numerical differential operator is increased: a second-order operator produces only a small amplitude bump, that is not present when the fourth-order operator is employed. At this stage, the conclusion is clear: the convergence of the Zerilli-Moncrief function computed from the separate knowledge of the multipoles $k_{\ell m}$ and $\chi_{\ell m}$ is a delicate issue that must be analyzed with care according to the physical problem under consideration. The violation of the perturbative Hamiltonian constraint and, in particular, the accuracy of the numerical derivative $\partial_r k_{\ell m}$ (note that we refer to the induced violation at the level of the wave extraction and not at that of the solution of the perturbation equations) seems to play an important role in the convergence properties of the waveforms. The main conclusions of the aforementioned numerical tests are: (i) The errors in $\Psi^{(\mathrm{e})}_{20}$ seem to behave like suggested in Eq. (6.6.3); (ii) The phenomenon occurs in the same way in both the 1D and 3D code, although the fine details of the oscillation are different.

Focusing on the 1D PerBaCCo , an accurate $\Psi^{(\mathrm{e})}_{\ell m}$ is obtained using sufficiently high resolution ($J_i = 300$) as well as a fourth-order representation for $\partial_r k_{\ell m}$. These prescriptions are accurate enough for the problem addressed in this paper, although they may not be sufficient for other stellar models or other initial perturbations. For example, using the PerBaCCo , with the same initial

---

[6] As discussed in Ref. [44] we cross-checked things also by matching the Zerilli-Moncrief function at the surface and evolving it with the Zerilli equation outwards. We found good agreement between the "matched" and the "computed" waveforms.

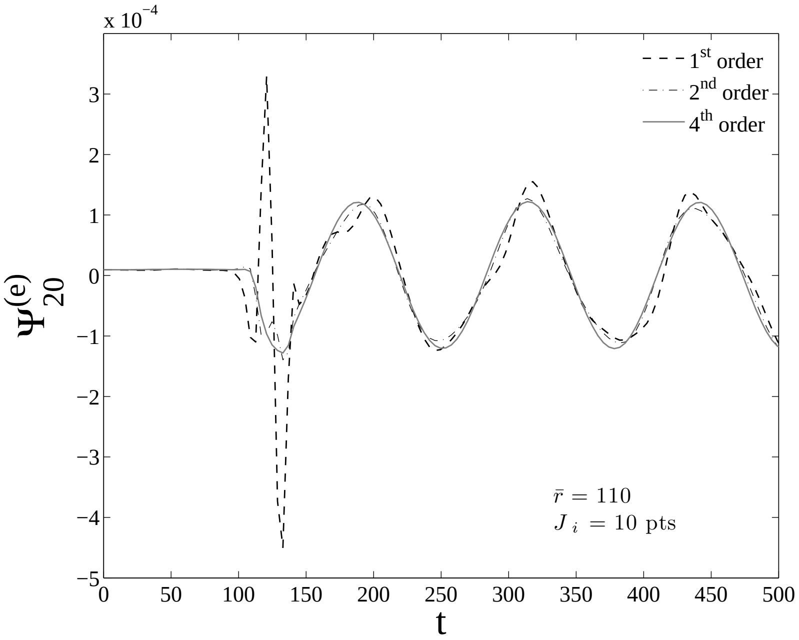

Figure 6.17: The amount of "junk" radiation present in the waveforms extracted in the 1D code is smaller when higher-order differential operators are used in Eq. (3.2.9) to compute the the Zerilli-Moncrief function.

data setup discussed here, in order to study the time-evolution of perturbations of stars with realistic EOS proved that higher resolutions are typically needed to produce convergent waveforms of comparable accuracy, see Chap. 4 and [43]. Likewise, for a polytropic EOS and initial data given by a Gaussian pulse in $\Psi^{(e)}_{20}$, we explain in Sec. 3.3.1 (See also Ref. [43]) how, at least, fourth-order accuracy in $\partial_r k_{20}$ is needed in order to have a consistent extraction of $\Psi^{(e)}_{20}$ already at $t = 0$. This suggests that the presence of linearly growing "junk" radiation in the computation of $\Psi^{(e)}_{\ell m}$ from the multipoles $(k_{\ell m}, \chi_{\ell m})$ can appear ubiquitously in the time evolutions of the perturbation equations with the PERBACCO . The presence of this "junk" in $\Psi^{(e)}_{\ell m}$ is the macroscopic manifestation of the violation of the perturbative Hamiltonian constraint due to errors (notably, in the discretization of the derivatives) introduced in the wave-extraction procedure. These (typically small) numerical errors are eventually magnified by the presence of an overall r factor in Eq. (6.6.1). Note that this phenomenon occurs even if the computation of the multipoles $(k_{\ell m}, \chi_{\ell m})$ is very accurate and the Hamiltonian constraint is satisfied by construction in the evolution algorithm. The analysis that we have presented here suggests that either increasing the resolution or, more reasonably, implementing higher-order differential operators in the perturbative "extraction" procedure are viable proposals to compute convergent waveforms.

In the 3D case the situation is more involved and we have not succeeded in

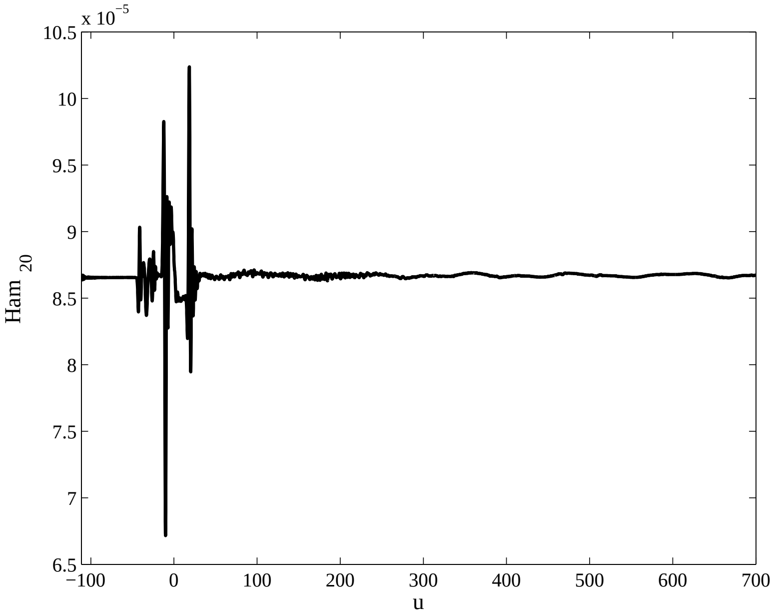

Figure 6.18: Hamiltonian constraint multipole reconstructed from the 3D extracted Zerilli-Moncrief function: a clear violation of the constraint is present at early (retarded) time related to the initial burst of junk radiation.

making statements as solid as in the 1D case. We can only rely on analogies: (i) The appearance the "junk" occurs in a way similar to the 1D case when the accuracy of the 1D Zerilli function is low; (ii) The two time-evolutions look qualitatively very similar. Yet, it is not technically possible to use in the 3D code resolutions equivalent to those of the 1D code. By analogy with our perturbative results, we can only conclude that it is not unreasonable that the "junk" in the 3D waveforms is the macroscopic manifestation of inaccuracies hidden in the implementation of the Abrahams-Price wave-extraction procedure and that lead to Fig. 6.18 shows the Hamiltonian constraint multipole reconstructed, via Eq. (3.2.5), from the output of a 3D simulation. While it is almost constant during the evolution, there is a clear violation related to the burst in the Zerilli-Moncrief function. The analysis presented here points out that such metric wave-extraction procedures require typically more subtle care than expected and these subtleties must be kept in mind in developing more modern wave-extraction routines.

The PSD of $\Psi^{(e)}_{20}$ in both the 1D case (solid line) and 3D case (dashed line) is displayed in Fig. 6.19. The initial perturbation amplitude is $\lambda = \lambda 0$ and the extraction radius is $\bar{r} = 110$. The spectrum of the 3D Zerilli waveform is consistent with what we observed in $r\psi_4^{20}$ below 10 kHz, but it looks different at higher frequencies (compare it with that of the "integrated" $\Psi^{(e)}_{20}$ in Fig. 6.11): here the PSD shows broad peaks attributable to the initial part of the waveform. Recovering the reasoning started in the previous section about the presence of

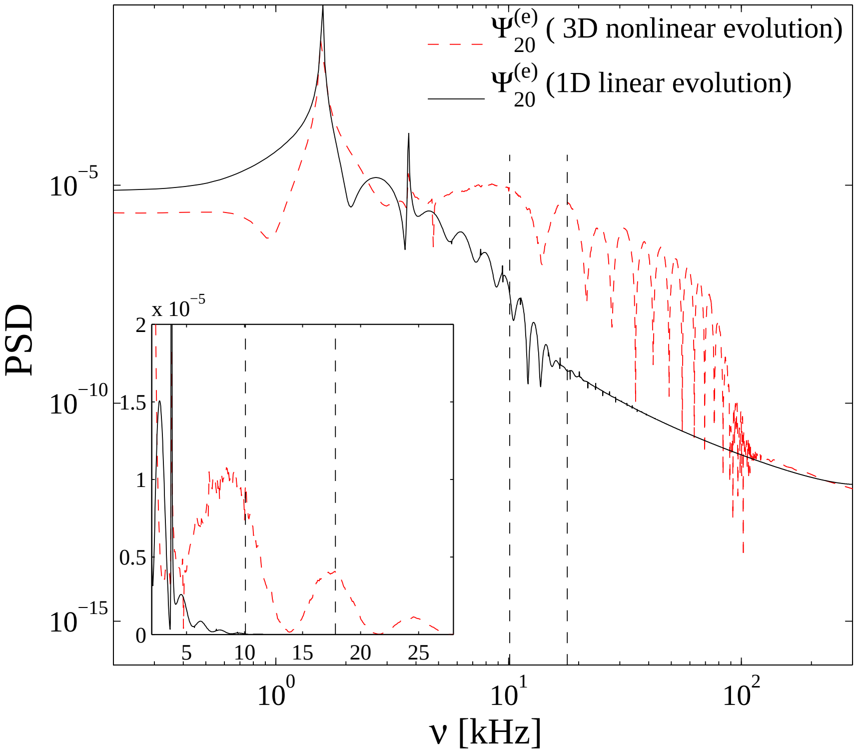

Figure 6.19: PSD of the 3D metric waveforms (dashed line) extracted á la Abrahams-Price (at $\bar{r} = 110$) and the corresponding 1D waveform (solid line) for an evolution with initial perturbation amplitude $\lambda = \lambda 0$. The Fourier spectrum of the "junk" radiation is compatible with some w-mode frequencies.

the w-modes, we can observe that the frequencies contained in the "junk" are compatible with the w-modes w_1 and w_2. However, since such frequencies belong to an unphysical part of the waveform, we prefer to consider them unphysical as well.

We conclude by mentioning, in passing, that the initial "junk" radiation is essentially not related to the systematic error introduced by fixing Schwarzschild coordinates for the "background" metric $\mathring{g}_{\mu\nu}$. This fact is suggested by Fig. 6.20, where we contrast the standard Zerilli-Moncrief function $\Psi^{(e)}_{20}$ (which assumes Schwarzschild coordinates for the background) with the *generalized* $\Psi^{\rm STMP}_{20}$ one based on the Sarbach-Tiglio [173] and Martel-Poisson [132] perturbation formalism, which does not require any gauge-fixing condition for the background submanifold M^2. This particular simulation was performed over a grid with three refinement levels and cubic boxes with limits [-120, 120], [-24,24] and [-12,12]. The resolution of each box is coarser than in the previous simulations, namely $\Delta_{xyz} = 1.875$, 0.9375 and 0.46875 respectively. Evidently, with this resolution the waveforms are less accurate, but we do not mind at this stage, since we are interested in an intrinsic comparison between extraction procedures at

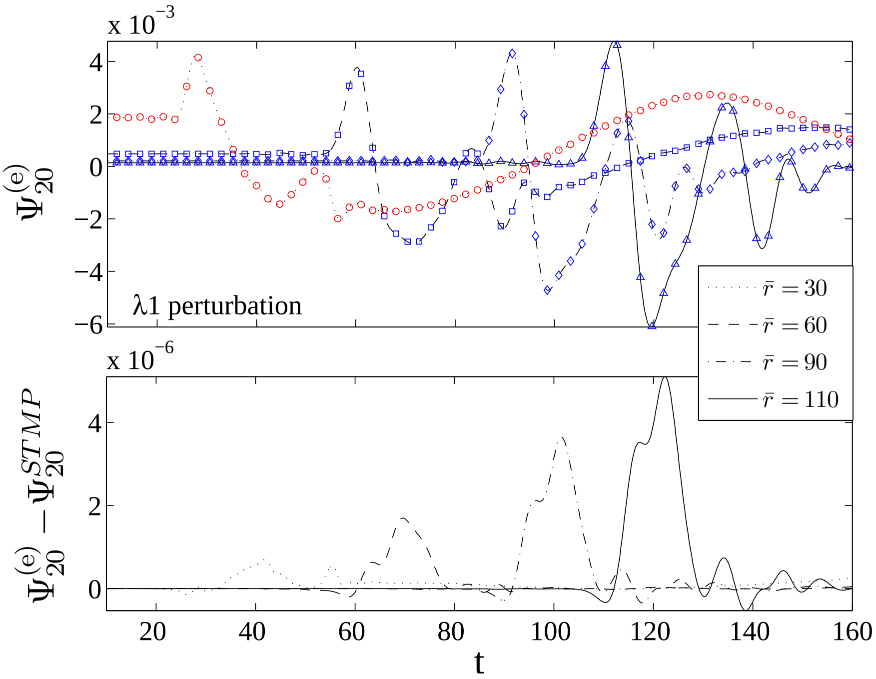

Figure 6.20: Generalized STMP metric extraction. The top panel compares the standard Zerilli-Moncrief $\Psi^{(e)}_{20}$ (depicted with lines) and the generalized $\Psi^{\rm STMP}_{20}$ (depicted with point markers) for the first part of the gravitational wave signal in an evolution with perturbation $\lambda = \lambda 1$. The waves extracted at four radii $\bar{r} \in \{30, 60, 90, 110\}$ are shown. The bottom panel shows that the present "junk" radiation negligibly depends on the choice of the coordinates of the background metric.

fixed resolution. The function $\Psi^{\rm STMP}_{\ell m}$ that we use is given by the straightforward [7] implementation of Eq. (4.23) of Ref. [132]. Note that this expression is equivalent to the combination of Eqs. (20), (25), (26) and (27) of Ref. [173]. The top panel of Fig. 6.20 displays $\Psi^{(e)}_{20}$ (lines) and $\Psi^{\rm STMP}_{20}$ (point markers) for observers at $\bar{r} \in \{30, 60, 90, 110\}$. It highlights that the differences the early-time part of the waveforms are very small. By contrast, the bottom panel of the figure, showing the difference $\Psi^{(e)}_{20} - \Psi^{\rm STMP}_{20}$, indicates that removing (part of) the systematic errors generates some improvement, but these are too small to be of any relevance. This analysis suggests that the inaccuracies in the early-time part of the waveform are essentially not related to the specific computation of the (generalized) Zerilli function, but rather connected to the underlying multipolar extraction infrastructure (grid setup, approximate solution of the constraints, interpolation procedures, computation of the derivatives of the metric *etc.*), on which we have relatively little control. We remark, however, that systematic effects that are very small in our physical system, as emphasized by Fig. 6.20, may be not small in other situations, as found in Ref. [157]. For this reason,

---

[7] With this we mean that we don't take into account any time dependence of the background metric due to coordinate effects. This possibility can be anyway easily taken into account by the formalism.

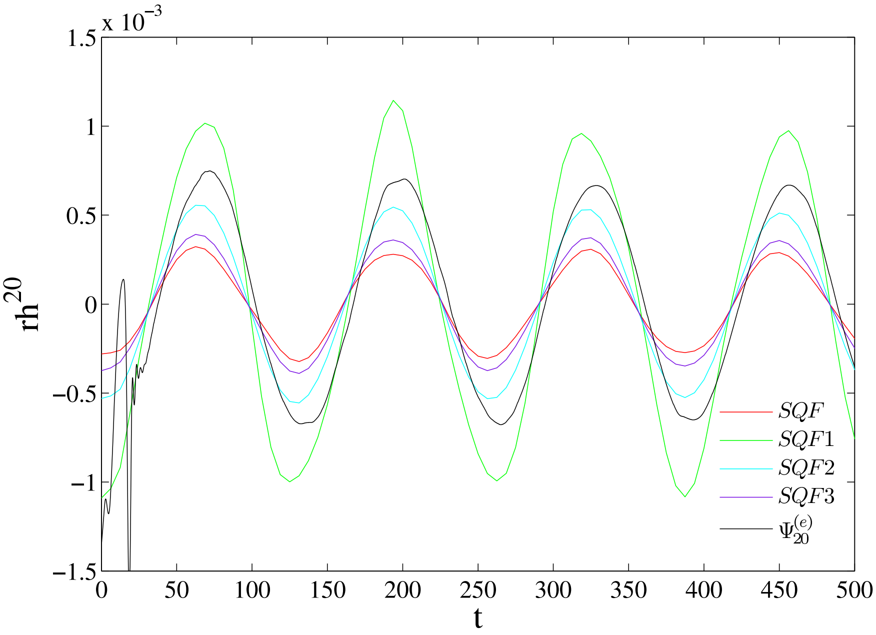

Figure 6.21: Comparison the SQFs and the Abrahams-Price wave-extraction procedure. The figure shows the rh^{20} waveforms. The frequencies almost coincide, while the amplitudes are strongly underestimated in all cases except SQF1, where the amplitude is strongly overestimated.

we underline that the formalism of Refs. [173, 132] is the actual correct metric formalism to extract waveforms out of a numerical space-time that can be considered a small deformation of the Schwarzschild one. As such, it must be taken into account properly in numerical codes.

6.7 Generalized quadrupole-type formulas

Let's finally analyze the performances of the various "generalized" quadrupole-type formulas that we have introduced in Sec. 5.3.

The results of our analysis are shown in Fig. 6.21 and Fig. 6.22. Fig. 6.21 displays rh^{20} waveforms obtained via the SQF1, SQF2, SQF3 and SQF4 (See Eq. (5.3.9)) for perturbation $\lambda = \lambda 0$. Fig. 6.22 complements this information by showing (for several perturbation magnitudes λ) the relative difference in amplitude between the various SQFs and the corresponding gauge-invariant Zerilli-Moncrief function $\Psi^{(\mathrm{e})}_{20}$. This analysis highlights that the quadrupole formula gives an excellent approximation to the phasing of the actual signals. By contrast, there is a systematic over or under-estimation of the amplitude depending on the choice of SQF.

A related observation is that the discrepancy between the quadrupole formula and the gauge-invariant waveform is not due to the fact that waveforms are extracted at a finite radius. Our results are consistent with those of Shibata and Sekiguchi [180], who performed an analysis similar to ours (and also consid-

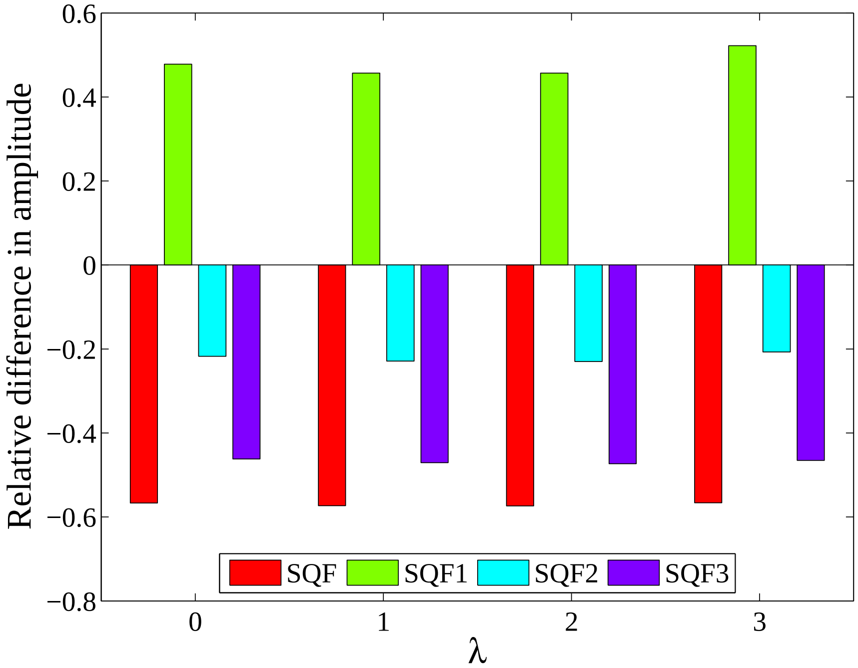

Figure 6.22: Comparison between the SQFs and the Abrahams-Price wave-extraction procedure. The figure shows the relative difference between the amplitudes of the various SQFs and the Abrahams-Price wave-extraction. These amplitudes are estimated with the fit procedure.

ered uniformly rotating stars), but without the possibility of contrasting their results with linear evolutions. In this respect, the main conclusion of Ref. [180] was that, although the amplitude of the waveform is systematically underestimated by the quadrupole formula Eq. (5.3.9e) (or Eq. (5.3.8)), it is however sufficiently accurate to capture both the frequency and the phasing (that are the most important quantities for detection) of the waveforms in a proper way. These results are fully confirmed here using totally different codes.

6.8 Nonlinear effects

In this section we comment on the onset of nonlinear effects for high values of the initial perturbation amplitude λ, showing, for the first time using full GR simulations, evidences for mode couplings and for the appearance of nonlinear harmonics.

In the linear regime ($\lambda = \lambda 0$) the star is oscillating at, essentially, the frequency of the fundamental quadrupolar proper fluid (quasi-normal) mode of pulsation. The principal linear modes excited are thus the $(\ell, m) = (2, 0)$ one and its overtones. For growing values of the initial perturbation, we observe that in 3D simulations, differently from the linear ones, the amplitude of the multipole $\Psi^{(e)}_{20}$ does not increases proportionally to λ but, instead, is progres-

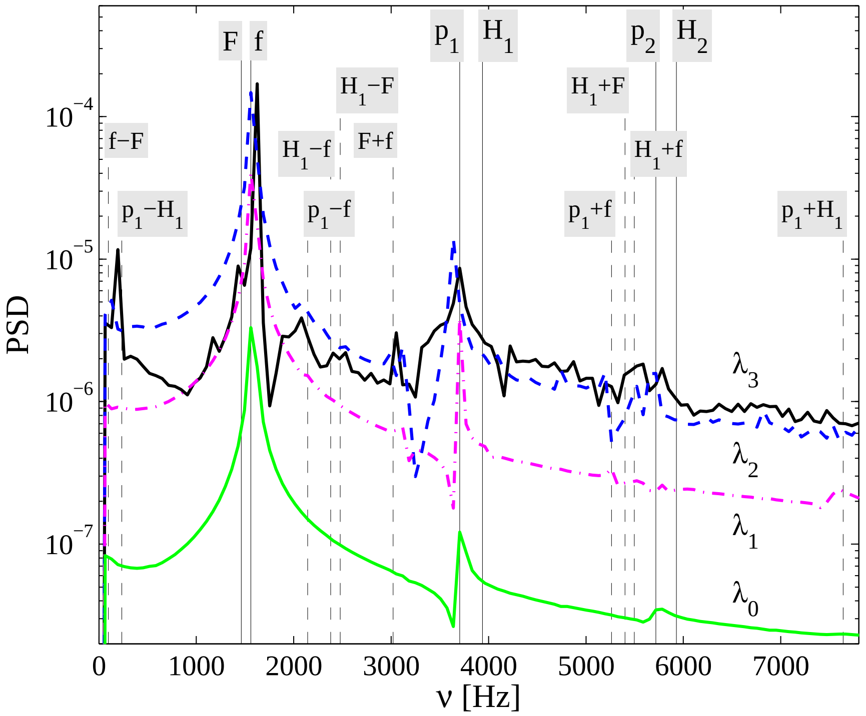

Figure 6.23: PSD of the quantity $\langle\rho(t)\rangle_{20}$ (See Eq. (6.8.1)) for different values of the initial perturbation amplitude λ. The spectra of the ($\ell = 2$, $m = 0$)-mode obtained in simulations with larger perturbations contain more frequencies, which originate from the nonlinear couplings with the overtones and with the radial modes.

sively reduced (See Fig. 6.8). This fact could be interpreted as the results of a typical phenomenon in nonlinear systems in which linear modes *couple* generating nonlinear harmonics. Naively, one could think that the "energy" associated to the $\ell = 2$ mode is re-distributed to the others while the system departs from the linear regime [8]. As we saw in Sec. 6.2, radial modes of oscillation are already present in the evolution of the equilibrium models. As a consequence, we expect to reveal couplings between non-radial and radial modes (F and its overtones $H_1, H_2, ...$) as a result of the onset of some nonlinear effect. In addition, we detect signals in multipoles of $\Psi^{(e)}_{\ell m}$ with $\ell = 4, 6$ and $m = 0, 4$, that are even-parity axisymmetric modes and non-axisymmetric modes triggered by the Cartesian grid. The amplitudes are very weak compared to those of the f mode for any value of λ, typically two orders of magnitude smaller for $\ell = 4, m = 0$ and three orders of magnitude for the others, but in principle they are present and must be considered. As far as the odd-parity modes with $m = 1, 2, 3$ and $\ell = 3, 5$ are concerned, they are all forbidden by the symmetry imposed on the

---

[8] We would like to stress that this picture is not so simple and rigorous, in particular there is no proof of the completeness of the star quasi-normal modes (even in the non-rotating case) and the definition of an energy per mode is definitely not straightforward. See the discussion in Ref. [147].

computational domain (octant).

As a strategy to study nonlinearities, we consider the rest-mass–density projections:

$$\langle \rho(t) \rangle_{\ell m} \equiv \int d^3x \rho(t, \mathbf{x}) Y^*_{\ell m} \tag{6.8.1}$$

and we apply to them the Fourier analysis. Like all the global variables, ρ contains all the frequencies of the system. Its projections in Eq. (6.8.1) allow to separate the contribution of each mode (ℓ, m). Fig. 6.23 shows the power spectrum of $\langle \rho \rangle_{20}$ for the four different values of λ. The signal for $\lambda = \lambda 0$ contains the 3 frequencies of the linear modes f, p_1 and p_2. The same happens for $\lambda = \lambda 1$ and $\lambda = \lambda 2$: The amplitudes of the linear modes grow linearly with λ and some new frequencies are present with small power for $\lambda = \lambda 2$. In the case of $\lambda = \lambda 3$, which corresponds to a pressure perturbation of 10% of the central TOV value, the spectra is rich of nonlinear harmonics. Most of them can be recognized as due to *weak couplings*, *i.e.* sums and differences of linear mode frequencies $\nu_1 \pm \nu_2$, also called *combination tones*. In particular we identify the nonlinear harmonics of the f-mode and its overtone $f \pm p_1$ and many frequencies $f \pm F$, $f \pm H_1$ and $p_1 \pm H_1$ due to the radial and non-radial mode couplings. Such couplings have been previously and extensively studied in Refs. [89, 188, 79] using Cowling approximation as well as the conformally flat approximation to GR. In addition, the couplings between radial and non-radial modes have been studied in detail in Ref. [155] by means of a second-order perturbative approach. Note how our fully general-relativistic results are consistent with all these studies.

The projection $\langle \rho \rangle_{00}$ describes essentially the radial mode of pulsations; analyzing this quantity instead of $\langle \rho \rangle_{20}$ gives analogous results in term of couplings. From the analysis of higher multipoles we compute the frequencies of the linear modes, finding $\nu = 2404$ Hz for $\ell = 4$ and $\nu = 2988$ Hz for $\ell = 6$. No couplings can be clearly recognized in these data. We stress that frequencies of the non-axisymmetric modes ($m = 4$) are the same of the axisymmetric ones because the star is non-rotating and modes are degenerate in m.

Conclusions

In this thesis we investigated the gravitational radiation emitted from neutron star oscillations. The problem has been handled with two complementary approach for the solution of the General Relativity equations, namely: the solution of the linear perturbations of spherically symmetric spacetime and the solution of full nonlinear Einstein equations within the Numerical Relativity framework.

The first approach has been, historically, widely used to study oscillations of non-rotating neutron stars but also gravitational collapse and black hole oscillations and point-particle motion around black holes. We presented in Chap. 3 a review of the equations together with a new code, the PerBaCCo , specifically designed to investigate the problem of wave extraction from non-spherical (matter and gravitational) linear perturbations of non-rotating neutron stars. This code solves, in the time domain, the Einstein equations linearized around a TOV background. It is 1+1 dimensional (*i.e.* one temporal and one spatial dimension) and adopts a constrained evolution scheme for even-parity sector system of equation. The latter choice allows for the computation of very long and very accurate time series and similarly accurate waveforms. In Chap. 4 we discussed these perturbative simulations. The results presented confirm and extend the previous works of Allen et al. [6] and Ruoff [169] (obtained with different codes) by considering time-domain simulations that take into account different kind of initial data and considering for the first time a very large sample of NS models and realistic EOS. Moreover we performed a detailed analysis of the waveforms by means of Fourier analysis (*i.e.* wave's energy spectrum) and fit analysis based on QNMs template. Such kind of analysis can be also applied to numerically computed waveforms from other scenarios, such as gravitational collapse or binary object simulations, and are the essential step to understand the link between the dynamics properties of the system to the observed ones, *i.e.* the waves.

For both odd and even-parity perturbations, our investigations addressed many points. In particular, for what concern the polar (even-parity) sector, if the initial configuration involves a fluid excitation, (type 1 and 2 initial data), the Zerilli-Moncrief function presents oscillations with fundamental frequency around 2-3 kHz due to the excitation of the fluid QNMs of the star. Thanks to the long-term and accurate simulations by the PerBaCCo we extracted the fluid mode frequencies from the wave's energy spectrum with an accuracy comparable to that of frequency domain codes. We computed also, for the first time, the damping time of the fundamental fluid frequency with an accuracy below 1% using data from a simulation of about 1 s and the fit analysis method.

The waveforms from NS models of different EOS show the same qualitative behavior characterized by the modes signature. Frequencies and damping times, in a first approximation, can be related with the star parameters, mass and radius, by quite general functional formulas [14, 42] but they differ, even significantly, in their values from EOS to EOS. When these frequencies will be revealed in a gravitational wave signal, they will hopefully provide useful information on the internal structure of neutron stars.

The effect of wave extraction at finite radii have also been investigated finding that observers should be placed at extraction radius $r > 200M$ in order to have amplitude errors below 1.6%.

If the non-conformally flat condition is imposed on the initial data setup (type 2 initial data), high frequencies and strongly damped w-mode oscillations are always present in the waveforms. The w-mode excitation is generally weak but it is less weak the more compact the star model is. For scattering-like initial data in both the odd and even-parity case the presence of w-modes is, again, more striking the higher is the compactness of the star and fluid modes are typically very weakly excited in this case (clearly they are totally absent in the odd-parity case).

Focusing to the axial (odd-parity) sector we compared the the scattering of odd-parity Gaussian pulses of gravitational radiation off relativistic stars with that of black holes. We have found that the excitation of w-modes and black hole QNMs occurs basically in the same way for both objects: pulses of small width (high frequencies) can trigger the w-modes, while for large width (low frequencies) one can only find curvature backscattering effects and non-oscillatory tails. When w-modes are present, we have shown that both Fourier and fit analysis are useful to understand the mode content of the waveforms but a clear identification of the modes is in general difficult. Specifically, pretty good estimates (with accuracy of few percents) of frequencies and damping times of spacetime modes, can be obtained only when damping times are not too short; *i.e.* , for the more compact models.

Neutron stars are expected to be highly rotating and magnetized object that, after their formation as the result of a gravitational collapse or a binary system merger, are characterized by nonlinear oscillations. Despite all the approximations that the linear approach presented here introduces (linearity, no rotation and no magnetic fields), it can provide, thank to the accuracy of the data, the flexibility and the low computational cost of the 1D code, robust informations on a wide sample of physical and technical aspects: NS models and EOS and waveforms analysis. In particular, it can also be used to provide useful test-beds for 3D nonlinear codes and must be seen as a first fundamental step trough the study of nonlinear effect.

Motivated by these considerations we decided to follow, as a second approach to the problem, the evolution of the very controlled system, represented by a non-rotating neutron star described by a polytropic EOS, that is oscillating non-radially due to an initial pressure perturbation, by means of 3D nonlinear Numerical-Relativity simulations. The initial pressure perturbation δp is given as an “approximate” eigenfunction of the star, whose maximum is a fraction of the central TOV pressure p_c. Initial data are of conformally flat type, and thus only fluid modes are expected in the GW signal. We focused only on $\ell = 2$, $m = 0$, quadrupolar, deformations but we analyzed four values of the initial perturbation amplitude in order to cover the transition from the linear to the nonlinear oscillatory regimes.

We have compared various gravitational-wave–extraction methods (See Chap. 5) that are nowadays the state-of-art in Numerical Relativity simulations: (i) The Abrahams-Price technique based on the gauge-invariant Regge-Wheeler-Zerilli-Moncrief perturbation theory of a Schwarzschild spacetime; (ii) The extraction method based on Weyl curvature scalars, notably the ψ_4 function; (iii) Some (variations of) quadrupole-type formulas.

The simulations presented in Chap. 6 have been performed via the `CACTUS--CARPET-CCATIE-Whisky` general-relativistic nonlinear code. This code solves the full set of Einstein equations in full generality in the three spatial dimensions. The accuracy of the waveforms extracted from the simulations, using the three methods recalled above, has been assessed (for small perturbations) via a comparison with waveforms, assumed to be "exact", computed by means of the PerBaCCo perturbative code (specifically the waveforms presented in Sec. 4.3.3, produced by the same initial data).

In doing 3D simulations in the perturbative regime, ($10^{-3} \lesssim \max(\delta p/p_c) \lesssim 10^{-2}$), we have found that both metric and curvature wave-extraction techniques generate waveforms that are consistent, both in amplitude and phasing, with the perturbative results. Each method, however, was found to have drawbacks. On one hand, the Zerilli-Moncrief function presents an unphysical burst in the early part of the waveform; on the other hand, the ψ_4 scalar requires a polynomial correction to obtain the corresponding metric multipole. Our conclusion is that, in our setup, one needs both extraction methods to end up with accurate waveforms.

For larger values of the initial perturbation amplitude, nonlinear effects in the 3D general relativistic simulations are clearly present. The effective relative amplitude of the main modes of the extracted gravitational wave is smaller for larger amplitudes of the initial perturbation, because of mode couplings. The analysis of the Fourier spectra of the rest-mass–density projections onto spherical harmonics highlights that couplings between radial and quadrupolar fluid modes are present. Our study represents the first confirmation, in fully general-relativistic simulations, of the results of Ref. [155], obtained via a perturbative approach.

In addition, we have shown that the (non-gauge-invariant) generalizations of the standard Newtonian quadrupole formula that we have considered can be useful tools to obtain accurate estimates of the frequency of oscillation. By contrast, amplitudes are always significantly under/overestimated, consistently with precedent observations of Refs. [180, 142].

Finally, we discussed in detail some systematic errors that occur in the early part of the waveform extracted á la Abrahams-Price. These errors show up, in the early part of the Zerilli-Moncrief function, in the form of a burst of "junk" radiation whose amplitude grows linearly with the extraction radius. We have proposed some heuristic explanation of this fact and reproduced a similar behavior in low-accuracy perturbative simulations. Globally, our conclusion is that the extraction of the Zerilli-Moncrief function from a numerical relativity simulation can be a delicate issue: small errors can conspire to give totally nonsensical results. Typically, these errors will show up as parts of the waveform whose amplitude grows with the observational radius. We have also implemented the generalized wave-extraction approach based on the formalism of Refs. [173, 132, 157, 120], without any evident benefit. Note, however, that these kind of problems encountered with the Abrahams-Price wave-extraction procedure as well as with its generalized version seem to appear specifically in the presence of matter (Note that is also the case where, generically, the simulations resolution is lower). In binary black-hole coalescence simulations curvature and metric waveforms seem to be fully consistent [158]. This last remark leads us to suggest that the Abrahams-Price wave-extraction technique, a "standardized" and very basic procedure and infrastructure that has been developed long ago (and tested at the time) for specific applications to black-hole physics, should be re-thought and re-analyzed when the Einstein equations are coupled to matter. For this reason, in the presence of matter, since systematic errors could be hard to detect and are present already in the simplest cases, we strongly encourage the community to make use of both wave-extraction techniques (curvature as well as metric perturbations) and to be always prepared to expect inaccuracies in the metric waveforms. In addition, concerning the many advantages related to extracting the metric waveforms directly from the space-time, we believe that it is also urgent and important for the community to have reliable implementations of the Abrahams-Price technique based on the Sarbach-Tiglio-Martel-Poisson [173, 132, 157, 120] formalism.

Acknowledgments

During the last three years I traveled a lot, I have been in many places and I learned a lot from many people. In each place I met someone who helped me, who gave me a good advice or simply a smile in front of a beer. Now it is difficult to remember everyone, all the discussions, all the good times, and I am also sure that a page of acknowledgments at the end of a thesis is not the place to thank people. However . . .

I thank Roberto De Pietri for many discussions, for encouragement during each experience I have undertaken and for having suggested always the crucial detail that I always missed.

I spent three beautiful and unforgettable months in Paris during autumn 2006. . . I am grateful to all the participants and organizers of the GRIHP Trimester. Sperando di riuscire a ri-trovarci da qualche parte: un saluto di cuore va a Brynmor "braian" Haskell e ad Umberto "amberto" Cannella.

I thank Luciano Rezzolla for many comments, discussions, suggestions and for the hospitality at AEI during spring 2007. I am grateful to Luca Baiotti and Bruno Giacomazzo for being always there when I need an advice (much more than one usually). I thank Marcus Ansorg who introduced me to spectral methods. My greetings to the AEI people, in particular Filippo Galeazzi, Christian Reisswig ("*...eine citrooonen*") and Jennifer Seiler.

Since my diploma thesis the works of Nick Stergioulas were a fundamental reference for my work, so it has been a great pleasure to have his comments and suggestions about [22, 43]. I am grateful also to Valeria Ferrari, Kostas Kokkotas, Pavel Haensel, Brynmor Haskell and Alexander Potekhin for comments and suggestions during the drafting of [43]. I thank Leonardo Gualtieri and Valeria Ferrari for computing the frequency domain data used in [44]. The radial perturbations in the PerBaCCo work thank to the help of Andrea Passamonti.

I am grateful to Tibault Damour for the hospitality at IHES during February 2008, a really quiet place for hard-working.

My greetings to Harry Dimmelmeier, which I met in Pisa in front of a huge pizza and a "tower" of beer, and Isabel Cordero-Carrión: it's a pleasure to find her periodically from time-2-time during meetings and conferences.

Un saluto speciale all'ufficio dottorandi HARD `@fis.unipr` (ma non mi scusero' mai per i poster -una volta tolti sará una valle di lacrime!- e per la musica. . .): Franco Neri, Sara Pasquetti, Gian Mario Manca and Giovanni "the debaggher" Corvino. Sempre a Parma saluto (con sternuto) Francesco "Shon" Coneri, Gabriele "Ramon" Davino, Carlo "killer"Meneghelli e Daniele Marmiroli. Non ringrazio la mia schiena.

I want to thank Bernd Bruegmann and my new colleagues in Jena: David Hilditch (absolutely the most friendly officemate...), Pablo "mano negra" Galaviz,

Andrea Nerozzi, Norbert Langes, Roman Gold and all the others. They made my recent months really good.

Finally, this thesis would not be the same (or simply would not be) without Alessandro Nagar, he showed me the way and taught me that it is not always straight... Grazie !

... "*dai diamanti non nasce niente*" ...

Sebastiano
December 2008
Gästehaus Am "Hell" Herrenberge 11, Jena

Appendix A

Quasi-Normal Modes

Quasi-Normal Modes (QNMs) are, roughly speaking, those damped-oscillating solutions of a certain class of mathematical problems describing physically "open systems". They are usually hyperbolic or parabolic Cauchy problems that involve not self-adjoint operators whose spectrum is purely continuous. Examples of such systems are waves on an infinite string, resonances in a particles scattering experiment or gravitational emission from vibrating black holes.

In this appendix we introduce the concept of QNMs using the most natural approach, *i.e.* the Laplace transform, and we discuss some properties of these solutions.

A.1 Laplace transform approach to solve the Cauchy IVP

Let's consider the Cauchy problem for the *wave* equation with a potential $V(x)$:

$$Q_{,tt}(t,x) - Q_{,xx}(t,x) + V(x)Q(t,x) = 0 \qquad \text{(A.1.1)}$$

with "initial data" ($x \in \mathbb{R}$):

$$\begin{aligned} Q(0,x) &= \psi(0,x) && \text{(A.1.2)} \\ Q_{,t}(0,x) &= \psi_{,t}(0,x) && \text{(A.1.3)} \end{aligned}$$

If the initial data has compact support or are sufficiently localized, then the solution ψ is bounded and admits a Laplace transform. The Laplace transform of the solution is:

$$\phi(s,x) \equiv \int_0^\infty e^{-st}\psi(t,x)dt \qquad \text{(A.1.4)}$$

and it is analytic for $\Re(s) > 0$. The function $\phi(s,x)$ satisfies the equation:

$$\phi_{,xx}(s,x) - \left(s^2 + V(x)\right)\phi(s,x) = F(s,x) \qquad \text{(A.1.5)}$$

where the source term $F(s,x)$ is:

$$F(s,x) \equiv -s\psi(0,x) - \psi_{,t}(0,x) \qquad \text{(A.1.6)}$$

Given two independent solutions, $f^-(s,x)$ and $f^+(s,x)$, of the homogeneous equation ($F=0$), the solution of Eq. A.1.5 is:

$$\phi(s,x) = \int_{-\infty}^{\infty} G(s,x,x')F(s,x)dx' \tag{A.1.7}$$

where the Green function generated from the homogeneous independent solutions is defined as:

$$G(s,x,x') \equiv \frac{f^-(s,x_<)f^+(s,x_>)}{W(s)} \tag{A.1.8}$$

$x_{<[>]} \equiv \min[\max](x,x')$, the Wronkskian is:

$$W(s) \equiv f^-(s,x_<)f^+_{,x}(s,x) - f^-_{,x}(s,x)f^+(s,x) \tag{A.1.9}$$

and it does not depend on x. The solution of the Cauchy problem can be obtained from the inverse Laplace transform of the ϕ solution:

$$\psi(t,x) = \frac{1}{2\pi i}\int_{\epsilon-i\infty}^{\epsilon+i\infty} e^{st}\phi(s,x)ds \tag{A.1.10}$$

If it is possible to solve (in a close form or approximately) for $\phi(s,x)$ then the integral in Eq. (A.1.10) can be evaluated in the standard way considering a close path which runs parallel and on the right of the imaginary s-axis and excludes essential singularities.

The solution of the Cauchy problem through its Laplace transform (Eq. (A.1.10) and Eq. (A.1.7)) contains already the initial data and also the requirement to be bounded at spatial infinity: this condition is fulfilled just choosing the two independent functions $f^-(s,x)$, $f^+(s,x)$ bounded.

A.2 QNMs in the Laplace picture

In this section we will see how QNMs emerge in the solution of the Cauchy problem (Eq. (A.1.10) and Eq. (A.1.7)) obtained with the Laplace method.

We assume to compute the integral in Eq. (A.1.10) considering a contour made of a segment $[\epsilon - iR, \epsilon + iR]$ parallel and on the right of the imaginary s-axis and close with a half circle Γ_R, passing then to the limit $R \to \infty$. To do this we adopt the following hypothesis:

1. There are no essential singularities;
2. $f^-(s,x)$, $f^+(s,x)$ are analytic;
3. the integral on Γ_R vanish for $R \to \infty$.

The following equation

$$\oint ds\ e^{st}\phi(s,x) = \int_{\Gamma_R}(\dots) + \int_{\epsilon-iR}^{\epsilon+iR}(\dots) = \int_{\epsilon-iR}^{\epsilon+iR}(\dots) \tag{A.2.1}$$

$$= \sum_k \text{res}\,(\dots, s_k) \tag{A.2.2}$$

leads to the solution:

$$\begin{aligned}
\psi(t,x) &= \frac{1}{2\pi i}\int_{\epsilon-i\infty}^{\epsilon+i\infty} ds\ e^{st}\phi(s,x) \qquad \text{(A.2.3)}\\
&= \frac{1}{2\pi i}\int_{\epsilon-i\infty}^{\epsilon+i\infty} ds\ e^{st}\int_{-\infty}^{\infty} dx'\ \frac{f^-(s,x_<)f^+(s,x_>)}{W(s)}F(s,x) \qquad \text{(A.2.4)}\\
&= \frac{1}{2\pi i}\int_{\epsilon-i\infty}^{\epsilon+i\infty} ds\ \frac{e^{st}}{W(s)}\int_{-\infty}^{\infty} dx'\ f^-(s,x_<)f^+(s,x_>)F(s,x) \qquad \text{(A.2.5)}\\
&= \sum_k \mathrm{res}\left(\frac{1}{W(s)},s_k\right)\ e^{s_k t}\int_{-\infty}^{\infty} dx'\ f^-(s_k,x_<)f^+(s_k,x_>)F(s_k,x) \qquad \text{(A.2.6)}
\end{aligned}$$

The poles s_k have all $\Re(s) < 0$ and correspond to the zeros of the Wrongskian. If in addition the initial data has compact support $[x_L, x_R]$, the solution for $x > x_R$ reads:

$$\psi(t,x) = \sum_k \underbrace{\mathrm{res}\left(\frac{1}{W(s)},s_k\right)\int_{-\infty}^{\infty} dx'\ f^-(s_k,x_<)F(s_k,x)}_{c_k}\ \underbrace{f^+(s_k,x_>)\ e^{s_k t}}_{u_k(t,x)} \tag{A.2.7}$$

and can be view as a a sum of *modes* $u_k(t,x)$. The asymptotic behavior of the spatial part of the modes (in the bounded solution) is:

$$f^{\mp}(x) \sim e^{\pm sx}\left(1+\mathcal{O}\left(\frac{1}{x}\right)\right) \quad \text{as } x \to \mp\infty \tag{A.2.8}$$

and holds for $\Re(s) > 0$. In the left plane $\Re(s) < 0$ the solution are continued analytically.

Under the assumptions we made, the analogies between normal modes of a closed system (*e.g.* a finite string or a system of springs) and QNMs solution are now quite evident. In particular, in the specific case presented, Eq. (A.2.7) suggest that every solution of the initial value problem can be represented by a superposition of QNMs $u_k(t,x)$. This happens in some cases when the potential fall off faster than exponentially (or has compact support) and it, or some derivatives, has a discontinuity. In the general case however QNMs do not form a complete set in the space of solutions. A related fact is that it is not possible to associate a well defined "energy" to each quasi-normal mode. Moreover Eq. (A.2.8) highlights their connection with the normal modes defined, as usual, via the Fourier transform of Eq. (A.1.1).

A.3 QNMs of black holes and neutron stars

In the case of BHs and NSs the equations of the perturbations from spherical symmetry are described by wave equations of type Eq. (A.1.1). In the case of BHs the potential $V(x)$ decay exponentially for $x \to -\infty$, it reach a maximum and then decay as x^{-2} for $x \to +\infty$. In the case of stars the situation is a little different. The potential of the odd perturbations, for example, is an infinity barrier in $x = 0$ (the star center) and decay as the BHs one for $x \to +\infty$.

Focusing on the more studied BHs case, it has been proved that:

1. $f^-(s,x)$ is analytic
2. $f^+(s,x)$ has an essential singularity in $s=0$, a brunch cut in the negative real axis, $\Re(s)<0$ and $\Im(s)=0$, and poles in the plane $\Re(s)<0$

The contour in this case can be chosen made of a segment $[\epsilon - iR, \epsilon + iR]$ parallel and on the right of the imaginary s-axis, a small circle γ_r around the origin and two segment $\delta^{\pm}_{R,r}$ up and down the negative real axis. It is close with two quarter of circle $\Gamma^{\pm}_R$ in the IV and III quadrants. The contributes to the solution are:

$$\int_{\epsilon-iR}^{\epsilon+iR}(...) = \underbrace{\int_{\Gamma_R^+}(...) + \int_{\Gamma_R^-}(...)}_{\text{early times}} \tag{A.3.1}$$

$$+ \underbrace{\int_{\delta^+_{R,r}}(...) + \int_{\delta^-_{R,r}}(...) + \int_{\gamma_r}(...)}_{\text{late times}} \tag{A.3.2}$$

$$- \underbrace{\sum_k \mathrm{res}\,(..., s_k)}_{\text{QNMs part}} \tag{A.3.3}$$

The "late time" contributes are responsible for the power tail described in Chap. 4 and their are essentially due to the "slow" behavior of the BH potential at large radii. For example in the case of Poschl-Teller potential, which mimic the peak of the Regge-Wheeler one but has exponential decay for $x \to +\infty$ the tail are absent in the signal. No tails are clearly present in the case of a potential with compact support. Finally, QNMs of BH do not form a complete set of modes as can be understood looking at the term that contribute at "early times": due to this term even an initial pulse of gravitation radiation cannot be described only by a superposition of QNMs, and in fact, as demonstrated in Chap. 4 the first part of the waves are characterized by the precursor and the burst.

Bibliography

[1] A. M. Abrahams et al. Gravitational wave extraction and outer boundary conditions by perturbative matching. *Phys. Rev. Lett.*, 80:1812–1815, 1998.

[2] A. M. Abrahams and R. H. Price. Applying black hole perturbation theory to numerically generated space-times. *Phys. Rev.*, D53:1963–1971, 1996.

[3] A. Akmal, V. R. Pandharipande, and D. G. Ravenhall. The equation of state for nucleon matter and neutron star structure. *Phys. Rev.*, C58:1804–1828, 1998.

[4] M. Alcubierre, B. Brügmann, P. Diener, M. Koppitz, D. Pollney, E. Seidel, and R. Takahashi. Gauge conditions for long-term numerical black hole evolutions without excision. *Phys. Rev. D*, 67:084023, 2003.

[5] M. Alcubierre, B. Brügmann, T. Dramlitsch, J. A. Font, P. Papadopoulos, E. Seidel, N. Stergioulas, and R. Takahashi. Towards a stable numerical evolution of strongly gravitating systems in general relativity: The conformal treatments. *Phys. Rev. D*, 62:044034, 2000.

[6] G. Allen, N. Andersson, K. D. Kokkotas, and B. F. Schutz. Gravitational waves from pulsating stars: Evolving the perturbation equations for a relativistic star. *Phys. Rev.*, D58:124012, 1998.

[7] G. Allen, K. Camarda, and E. Seidel. Black hole spectroscopy: Determining waveforms from 3D excited black holes. 1998.

[8] G. Allen, K. Camarda, and E. Seidel. Evolution of distorted black holes: A perturbative approach. 1998.

[9] M. A. Aloy, J. M. Ibáñez, J. M. Mart´i, and E. Müller. *Astrophys. J. Supp.*, 122:151, 1999.

[10] N. Andersson. Excitation of Schwarzschild black hole quasinormal modes. *Phys. Rev.*, D51:353–363, 1995.

[11] N. Andersson. Scattering of massless scalar waves by a Schwarzschild black hole: A Phase integral study. *Phys. Rev.*, D52:1808–1820, 1995.

[12] N. Andersson. Evolving test-fields in a black-hole geometry. *Phys. Rev.*, D55:468–479, 1997.

[13] N. Andersson and K. D. Kokkotas. Gravitational waves and pulsating stars: What can we learn from future observations? *Phys. Rev. Lett.*, 77:4134–4137, 1996.

[14] N. Andersson and K. D. Kokkotas. Towards gravitational-wave asteroseismology. *Mon. Not. Roy. Astron. Soc.*, 299:1059–1068, 1998.

[15] N. Andersson and K. D. Kokkotas. Gravitational-wave astronomy: The high-frequency window. *Lect. Notes Phys.*, 653:255–276, 2004.

[16] Z. Andrade. Trapped and excited w modes of stars with a phase transition and R¿=5M. *Phys. Rev.*, D63:124002, 2001.

[17] M. Ansorg, A. Kleinwachter, and R. Meinel. Highly accurate calculation of rotating neutron stars. *Astron. Astrophys.*, 381:L49, 2002.

[18] M. Ansorg, A. Kleinwachter, and R. Meinel. Highly accurate calculation of rotating neutron stars: Detailed description of the numerical methods. *Astron.Astrophys.*, 405:711, 2003.

[19] L. Anton et al. Numerical 3+1 general relativistic magnetohydrodynamics: a local characteristic approach. *Astrophys. J.*, 637:296, 2006.

[20] W. D. Arnett and R. L. Bowers. A microscopic interpretation of neutron star structure. *Astrophys. J. Suppl. Series*, 33:415–436, 1977.

[21] R. Arnotwitt, S. Deser, and C. Misner. Canonical variables for general relativity. *Physical Review*, 117(6):1595–1602, March 1960.

[22] L. Baiotti, S. Bernuzzi, G. Corvino, R. De Pietri, and A. Nagar. Gravitational-wave extraction from neutron star oscillations: comparing linear and nonlinear techniques. *Phys. Rev.*, D79:024002, 2009.

[23] L. Baiotti, R. De Pietri, G. M. Manca, and L. Rezzolla. Accurate simulations of the dynamical bar-mode instability in full General Relativity. *Phys. Rev.*, D75:044023, 2007.

[24] L. Baiotti et al. Three-dimensional relativistic simulations of rotating neutron star collapse to a Kerr black hole. *Phys. Rev.*, D71:024035, 2005.

[25] L. Baiotti, B. Giacomazzo, and L. Rezzolla. Accurate evolutions of inspiralling neutron-star binaries: prompt and delayed collapse to black hole. *Phys. Rev.*, D78:084033, 2008.

[26] L. Baiotti, I. Hawke, P. Montero, and L. Rezzolla. A new three-dimensional general-relativistic hydrodynamics code. In R. Capuzzo-Dolcetta, editor, *Computational Astrophysics in Italy: Methods and Tools*, volume 1, page 210, Trieste, 2003. Mem. Soc. Astron. It. Suppl.

[27] L. Baiotti, I. Hawke, L. Rezzolla, and E. Schnetter. Gravitational-wave emission from rotating gravitational collapse in three dimensions. *Phys. Rev. Lett.*, 94:131101, 2005.

[28] L. Baiotti and L. Rezzolla. Challenging the paradigm of singularity excision in gravitational collapse. *Phys. Rev. Lett.*, 97:141101, 2006.

[29] J. G. Baker, J. Centrella, D.-I. Choi, M. Koppitz, and J. van Meter. Gravitational wave extraction from an inspiraling configuration of merging black holes. *Phys. Rev. Lett.*, 96:111102, 2006.

[30] J. G. Baker et al. Mergers of non-spinning black-hole binaries: Gravitational radiation characteristics. 2008.

[31] F. Banyuls, J. A. Font, J. M. Ibáñez, J. M. Mart´i, and J. A. Miralles. Numerical 3+1 general-relativistic hydrodynamics: A local characteristic approach. *Astrophys. J.*, 476:221, 1997.

[32] J. M. Bardeen. Stability of Circular Orbits in Stationary, Axisymmetric Space-Times. *Astrophys. J.*, 161:103–+, July 1970.

[33] J. M. Bardeen, W. H. Press, and S. A. Teukolsky. Rotating black holes: Locally nonrotating frames, energy extraction, and scalar synchrotron radiation. *Astrophys. J.*, 178:347, 1972.

[34] J. M. Bardeen, K. S. Thorne, and D. W. Meltzer. A Catalogue of Methods for Studying the Normal Modes of Radial Pulsation of General-Relativistic Stellar Models. *Astrophys. J.*, 145:505, Aug. 1966.

[35] J. M. Bardeen and R. V. Wagoner. Relativistic Disks. I. Uniform Rotation. *Astrophys. J.*, 167:359–+, Aug. 1971.

[36] T. W. Baumgarte and S. L. Shapiro. On the numerical integration of einstein's field equations. *Phys. Rev.*, D59:024007, 1999.

[37] T. W. Baumgarte and S. L. Shapiro. Numerical relativity and compact binaries. *Phys. Rept.*, 376:41–131, 2003.

[38] T. W. Baumgarte, S. L. Shapiro, and M. Shibata. On the Maximum Mass of Differentially Rotating Neutron Stars. *Astrophys. J.*, 528:L29, 2000.

[39] G. Baym, H. A. Bethe, and C. J. Pethick. Neutron star matter. *Nuclear Physics A*, 175:225–271, 1971.

[40] G. Baym, C. Pethick, and P. Sutherland. The Ground State of Matter at High Densities: Equation of State and Stellar Models. *Astrophys. J.*, 170:299–+, Dec. 1971.

[41] O. Benhar, E. Berti, and V. Ferrari. The imprint of the equation of state on the axial w-modes of oscillating neutron stars. *Mon. Not. Roy. Astron. Soc.*, 310:797–803, 1999.

[42] O. Benhar, V. Ferrari, and L. Gualtieri. Gravitational wave asteroseismology revisited. *Phys. Rev.*, D70:124015, 2004.

[43] S. Bernuzzi and A. Nagar. Gravitational waves from pulsations of neutron stars described by realistic Equations of State. *Phys. Rev.*, D78:024024, 2008.

[44] S. Bernuzzi, A. Nagar, and R. De Pietri. Dynamical excitation of spacetime modes of compact objects. *Phys. Rev.*, D77:044042, 2008.

[45] E. Berti, V. Cardoso, J. A. Gonzalez, and U. Sperhake. Mining information from binary black hole mergers: a comparison of estimation methods for complex exponentials in noise. *Phys. Rev.*, D75:124017, 2007.

[46] E. Berti et al. Inspiral, merger and ringdown of unequal mass black hole binaries: A multipolar analysis. *Phys. Rev.*, D76:064034, 2007.

[47] H. A. Bethe and M. B. Johnson. Dense baryon matter calculations with realistic potentials. *Nucl. Phys.*, A230:1–58, 1974.

[48] L. Blanchet and T. Damour. Radiative gravitational fields in general relativity. I. General structure of the field outside the source. *Royal Society of London Proceedings Series A*, 320:379–430, 1986.

[49] L. Blanchet and T. Damour. Tail transported temporal correlations in the dynamics of a gravitating system. *Phys. Rev.*, D37:1410, 1988.

[50] L. Blanchet, T. Damour, and G. Schafer. Postnewtonian hydrodynamics and postnewtonian gravitational wave generation for numerical relativity. *Mon. Not. Roy. Astron. Soc.*, 242:289–305, 1990.

[51] M. Bocquet, S. Bonazzola, E. Gourgoulhon, and J. Novak. Rotating neutron star models with a magnetic field. *Astron. Astrophys.*, 301:757–+, Sept. 1995.

[52] C. Bona, J. Massó, E. Seidel, and J. Stela. New Formalism for Numerical Relativity. *Phys. Rev. Lett.*, 75:600–603, 1995.

[53] S. Bonazzola, E. Gourgoulhon, M. Salgado, and J. A. Marck. Axisymmetric rotating relativistic bodies: A new numerical approach for 'exact' solutions. *Astron. Astrophys.*, 278:421–443, Nov. 1993.

[54] S. Bonazzola and J. Schneider. An Exact Study of Rigidly and Rapidly Rotating Stars in General Relativity with Application to the Crab Pulsar. *Astrophys. J.*, 191:273–290, July 1974.

[55] R. L. Bowers, A. M. Gleeson, and R. Daryl Pedigo. Relativistic superdense matter in cold systems: Applications. *Phys. Rev.*, pages 3056–3068, Nov. 1975.

[56] R. L. Bowers, A. M. Gleeson, and R. Daryl Pedigo. Relativistic superdense matter in cold systems: Theory. *Phys. Rev.*, pages 3043–3055, Nov. 1975.

[57] E. M. Butterworth. On the structure and stability of rapidly rotating fluid bodies in general relativity. II - The structure of uniformly rotating pseudopolytropes. *Astrophys. J.*, 204:561–572, Mar. 1976.

[58] E. M. Butterworth and J. R. Ipser. On the structure and stability of rapidly rotating fluid bodies in general relativity. I - The numerical method for computing structure and its application to uniformly rotating homogeneous bodies. *Astrophys. J.*, 204:200–223, Feb. 1976.

[59] CACTUS Code Homepage. http://www.cactuscode.org/.

[60] K. Camarda and E. Seidel. Three-dimensional simulations of distorted black holes. I. Comparison with axisymmetric results. *Phys. Rev.*, D59:064019, 1999.

[61] M. Campanelli and C. O. Lousto. Second order gauge invariant gravitational perturbations of a Kerr black hole. *Phys. Rev.*, D59:124022, 1999.

[62] A. Campolattaro and K. S. Thorne. Non-radial Pulsation of General-Relativistic Stellar Models. V. Analytic Analysis for L = 1. *Astrophys. J.*, 159:847, Mar. 1970.

[63] V. Canuto and S. M. Chitre. Crystallization of dense neutron matter. *Phys. Rev.*, pages 1587–1613, 1974.

[64] CARPET Code Homepage. http://www.carpetcode.org/.

[65] P. Cerda-Duran et al. CFC+: Improved dynamics and gravitational waveforms from relativistic core collapse simulations. 2004.

[66] S. Chandrasekhar. The Dynamical Instability of Gaseous Masses Approaching the Schwarzschild Limit in General Relativity. *Astrophys. J.*, 140:417, Aug. 1964.

[67] S. Chandrasekhar and V. Ferrari. On the non-radial oscillations of a star. *Proc. Roy. Soc. Lond.*, A432:247–279, 1991.

[68] S. Chandrasekhar and A. King. Book-Review - the Mathematical Theory of Black-Holes. *The Observatory*, 104:39–+, Feb. 1984.

[69] K. S. T. Charles W. Misner and J. A. Wheeler. *Gravitation.* W. H. Freeman and Company, San Francisco, 1973.

[70] P. Colella and P. R. Woodward. *J. Comput. Phys.*, 54:174, 1984.

[71] G. B. Cook, S. L. Shapiro, and S. A. Teukolsky. Rapidly rotating polytropes in general relativity.

[72] G. B. Cook, S. L. Shapiro, and S. A. Teukolsky. Spin-up of a rapidly rotating star by angular momentum loss - Effects of general relativity. *Astrophys. J.*, 398:203–223, Oct. 1992.

[73] G. B. Cook, S. L. Shapiro, and S. A. Teukolsky. Rapidly rotating neutron stars in general relativity: Realistic equations of state. *Astrophys. J.*, 424:823, 1994.

[74] T. Damour, A. Nagar, M. Hannam, S. Husa, and B. Brugmann. Accurate Effective-One-Body waveforms of inspiralling and coalescing black-hole binaries. 2008.

[75] M. Davis, R. Ruffini, and J. Tiomno. Pulses of gravitational radiation of a particle falling radially into a schwarzschild black hole. *Phys. Rev.*, D5:2932–2935, 1972.

[76] R. De Pietri. Private Communication, 2008.

[77] H. Dimmelmeier, J. A. Font, and E. Muller. Relativistic simulations of rotational core collapse. II. Collapse dynamics and gravitational radiation. *Astron. Astrophys.*, 393:523–542, 2002.

[78] H. Dimmelmeier, C. D. Ott, H.-T. Janka, A. Marek, and E. Mueller. Generic gravitational wave signals from the collapse of rotating stellar cores. *Phys. Rev. Lett.*, 98:251101, 2007.

[79] H. Dimmelmeier, N. Stergioulas, and J. A. Font. Non-linear axisymmetric pulsations of rotating relativistic stars in the conformal flatness approximation. *Mon. Not. Roy. Astron. Soc.*, 368:1609–1630, 2006.

[80] E. N. Dorband, E. Berti, P. Diener, E. Schnetter, and M. Tiglio. A numerical study of the quasinormal mode excitation of Kerr black holes. *Phys. Rev.*, D74:084028, 2006.

[81] F. Douchin and P. Haensel. A unified equation of state of dense matter and neutron star structure. *Astron. Astrophys.*, 380:151–167, 2001.

[82] M. D. Duez et al. Evolving black hole-neutron star binaries in general relativity using pseudospectral and finite difference methods. *Phys. Rev.*, D78:104015, 2008.

[83] Z. B. Etienne et al. Fully General Relativistic Simulations of Black Hole-Neutron Star Mergers. *Phys. Rev.*, D77:084002, 2008.

[84] V. Ferrari, L. Gualtieri, J. A. Pons, and A. Stavridis. Gravitational Waves from Rotating Proto-Neutron Stars. *Class. Quant. Grav.*, 21:S515–S519, 2004.

[85] V. Ferrari, L. Gualtieri, J. A. Pons, and A. Stavridis. Rotational effects on the oscillation frequencies of newly born proto-neutron stars. *Mon. Not. Roy. Astron. Soc.*, 350:763, 2004.

[86] V. Ferrari and K. D. Kokkotas. Scattering of particles by neutron stars: Time-evolutions for axial perturbations. *Phys. Rev.*, D62:107504, 2000.

[87] L. S. Finn and C. R. Evans. Determining gravitational radiation from Newtonian self-gravitating systems. *Astrophys. J.*, 351:588–600, Mar. 1990.

[88] J. A. Font. Numerical hydrodynamics in general relativity. *Living Reviews in Relativity*, 6(4), 2003.

[89] J. A. Font, H. Dimmelmeier, A. Gupta, and N. Stergioulas. Axisymmetric Modes of Rotating Relativistic Stars in the Cowling Approximation. *Mon. Not. Roy. Astron. Soc.*, 325:1463, 2001.

[90] J. A. Font et al. Three-dimensional general relativistic hydrodynamics. II: Long-term dynamics of single relativistic stars. *Phys. Rev.*, D65:084024, 2002.

[91] B. Friedman and V. R. Pandharipande. Hot and cold, nuclear and neutron matter. *Nuclear Physics A*, 361:502–520, 1981.

[92] J. L. Friedman, L. Parker, and J. R. Ipser. Rapidly rotating neutron star models. *Astrophys. J.*, 304:115, 1986.

[93] e. . Frolov, V. P. and e. . Novikov, I. D. Black hole physics: Basic concepts and new developments. Dordrecht, Netherlands: Kluwer Academic (1998) 770 p.

[94] U. H. Gerlach and U. K. Sengupta. Gauge invariant perturbations on most general spherically symmetric space-times. *Phys. Rev.*, D19:2268–2272, 1979.

[95] U. H. Gerlach and U. K. Sengupta. Gauge invariant coupled gravitational, acoustical, and electromagnetic modes on most general spherical space-times. *Phys. Rev.*, D22:1300–1312, 1980.

[96] T. Goodale, G. Allen, G. Lanfermann, J. Massó, T. Radke, E. Seidel, and J. Shalf. The Cactus framework and toolkit: Design and applications. In *Vector and Parallel Processing – VECPAR'2002, 5th International Conference, Lecture Notes in Computer Science*, Berlin, 2003. Springer.

[97] E. Gourgoulhon. An introduction to relativistic hydrodynamics. *EAS Publ. Ser.*, 21:43, 2006.

[98] E. Gourgoulhon. 3+1 Formalism and Bases of Numerical Relativity. 2007.

[99] L. Gualtieri, E. Berti, J. A. Pons, G. Miniutti, and V. Ferrari. Gravitational signals emitted by a point mass orbiting a neutron star: A perturbative approach. *Phys. Rev.*, D64:104007, 2001.

[100] L. Gualtieri and V. Ferrari. Private Communication, 2007.

[101] C. Gundlach and J. M. Martin-Garcia. Gauge-invariant and coordinate-independent perturbations of stellar collapse. I: The interior. *Phys. Rev.*, D61:084024, 2000.

[102] L. Gunnarsen, H.-A. Shinkai, and K.-I. Maeda. Finding principal null directions for numerical relativists. 1994.

[103] P. Haensel and B. Pichon. Experimental nuclear masses and the ground state of cold dense matter. *Astron. Astrophys.*, 283:313–318, 1994.

[104] P. Haensel and A. Y. Potekhin. Analytical representations of unified equations of state of neutron-star matter. *Astron. Astrophys.*, 428:191–197, 2004.

[105] P. Haensel, A. Y. Potekhin, and D. G. Yakovlev. *Neutron stars 1: Equation of state and structure.* Springer, New York, USA, 2007.

[106] P. Haensel and M. Proszynski. Pion condensation in cold dense matter and neutron stars. *Astrophys. J.*, 258:306–320, July 1982.

[107] A. Harten, B. Engquist, S. Osher, and S. R. Chakrabarty. Uniformly high order accurate essentially non-oscillatory schemes III. *J. Comput. Phys.*, 71:2311, 1987.

[108] A. Harten, P. D. Lax, and B. van Leer. *SIAM Rev.*, 25:35, 1983.

[109] J. B. Hartle. *An introduction to Einstein's general relativity.* Addison-Wesley, San Francisco, USA, 2003.

[110] J. Ibáñez, M. Aloy, J. Font, J. Mart´i, J. Miralles, and J. Pons. In E. Toro, editor, *Godunov methods: theory and applications*, New York, 2001. Kluwer Academic/Plenum Publishers.

[111] J. R. Ipser and K. S. Thorne. Relativistic, Spherically Symmetric Star Clusters. I. Stability Theory for Radial Perturbations. *Astrophys. J.*, 154:251–+, Oct. 1968.

[112] L. E. Kidder. Using Full Information When Computing Modes of Post-Newtonian Waveforms From Inspiralling Compact Binaries in Circular Orbit. 2007.

[113] K. D. Kokkotas and J. Ruoff. Radial oscillations of relativistic stars. *Astron. Astrophys.*, 366:565, 2001.

[114] K. D. Kokkotas and J. Ruoff. Instabilities of relativistic stars. 2002.

[115] K. D. Kokkotas and B. Schmidt. Quasi-normal modes of stars and black holes. *Living Reviews in Relativity*, 2(2), 1999.

[116] K. D. Kokkotas and B. F. Schutz. W-modes: A New family of normal modes of pulsating relativistic stars. *Mon. Not. Roy. Astron. Soc.*, 225:119, 1992.

[117] H. Komatsu, Y. Eriguchi, and I. Hachisu. Rapidly rotating general relativistic stars. I - Numerical method and its application to uniformly rotating polytropes. *Mon. Not. Roy. Astron. Soc.*, 237:355–379, Mar. 1989.

[118] H. Komatsu, Y. Eriguchi, and I. Hachisu. Rapidly rotating general relativistic stars. II - Differentially rotating polytropes. *Mon. Not. Roy. Astron. Soc.*, 239:153–171, July 1989.

[119] M. Koppitz, D. Pollney, C. Reisswig, L. Rezzolla, J. Thornburg, P. Diener, and E. Schnetter. Getting a kick from equal-mass binary black hole mergers. *Phys. Rev. Lett.*, 99:041102, 2007.

[120] O. Korobkin, B. Aksoylu, M. Holst, E. Pazos, and M. Tiglio. Solving the Einstein constraint equations on multi-block triangulations using finite element methods. 2008.

[121] W. G. Laarakkers and E. Poisson. Quadrupole moments of neutron stars. *Astrophys. J.*, 512:282, 1998.

[122] L. D. Landau and E. M. Lifsits. *Teoria dei campi.* Editori Riuniti Mir, Roma, 3rd edition, 1999.

[123] J. M. Lattimer and M. Prakash. Neutron Star Observations: Prognosis for Equation of State Constraints. *Phys. Rept.*, 442:109–165, 2007.

[124] S. R. Lau. Analytic structure of radiation boundary kernels for blackhole perturbations. *J. Math. Phys.*, 46:102503, 2005.

[125] P. Lax and B. Wendroff. Sistem of conservation law. *Commun. Pure Appl. Math.*, 13:217–237, 1960.

[126] L. Lehner. Numerical relativity: A review. *Class. Quant. Grav.*, 18:R25–R86, 2001.

[127] G. Leiler and L. Rezzolla. On the iterated Crank-Nicolson method for hyperbolic and parabolic equations in numerical relativity. *Phys. Rev. D*, 73:044001, 2006.

[128] R. J. LeVeque. *Finite Volume Methods for Hyperbolic Problems.* Cambridge University Press, 2002.

[129] L. Lindblom and S. L. Detweiler. The quadrupole oscillations of neutron stars. *Astrophys. J. Suppl. Ser.*, 53:73–92, Sept. 1983.

[130] C. P. Lorenz, D. G. Ravenhall, and C. J. Pethick. Neutron star crusts. *Physical Review Letters*, 70:379–382, Jan. 1993.

[131] D. R. Lorimer. Binary and millisecond pulsars. *Living Reviews in Relativity*, 11(8), 2008.

[132] K. Martel and E. Poisson. Gravitational perturbations of the schwarzschild spacetime: A practical covariant and gauge-invariant formalism. *Physical Review D (Particles, Fields, Gravitation, and Cosmology)*, 71(10):104003, 2005.

[133] J. M. Mart´i, J. M. Ibáñez, and J. A. Miralles. Numerical relativistic hydrodynamics: Local characteristic approach. *Phys. Rev. D*, 43:3794, 1991.

[134] J. M. Mart´i and E. Müller. Numerical hydrodynamics in special relativity. *Living Reviews in Relativity*, 6(7), 2003.

[135] J. M. Martin-Garcia and C. Gundlach. Gauge-invariant and coordinate-independent perturbations of stellar collapse. II: Matching to the exterior. *Phys. Rev.*, D64:024012, 2001.

[136] D. W. Meltzer and K. S. Thorne. Normal Modes of Radial Pulsation of Stars at the End Point of Thermonuclear Evolution. *Astrophys. J.*, 145:514, Aug. 1966.

[137] V. Moncrief. Gravitational perturbations of spherically symmetric systems. I. The exterior problem. *Ann. Phys.*, 88:323–342, 1974.

[138] V. Moncrief. Gravitational perturbations of spherically symmetric systems. ii. perfect fluid interiors. *Ann. Phys.*, 88(2):343 – 370, 1974.

[139] A. Nagar. *The Time Evolution of Non-Spherical Perturbations of Compact Object and Gravitational Radiation.* PhD These, Universitá degli Studi di Parma, 2004.

[140] A. Nagar and G. Diaz. Fluid accretion onto relativistic stars and gravitational radiation. *in Proceedings of 27th Spanish Relativity Meeting (ERE 2003): Gravitational Radiation, Alicante, Spain, 11-13 Sep 2003*, 2004.

[141] A. Nagar, G. Diaz, J. A. Pons, and J. A. Font. Accretion-driven gravitational radiation from non-rotating compact objects. I: Radially infalling quadrupolar shells. *Phys. Rev.*, D69:124028, 2004.

[142] A. Nagar, J. A. Font, O. Zanotti, and R. De Pietri. Gravitational waves from oscillating accretion tori: Comparison between different approaches. *Phys. Rev.*, D72:024007, 2005.

[143] A. Nagar and L. Rezzolla. Gauge-invariant non-spherical metric perturbations of Schwarzschild black-hole spacetimes. *Class. Quant. Grav.*, 22:R167, 2005.

[144] T. Nakamura, K. Oohara, and Y. Kojima. General relativistic collapse to black holes and gravitational waves from black holes. *Prog. Theor. Phys. Suppl.*, 90:1–218, 1987.

[145] A. Nerozzi. Scalar functions for wave extraction in numerical relativity. *Phys. Rev.*, D75:104002, 2007.

[146] E. T. Newman and P. R. *J. Math. Phys.*, 3:566, 1962.

[147] H.-P. Nollert. TOPICAL REVIEW: Quasinormal modes: the characteristic ‘sound’ of black holes and neutron stars. *Class. Quant. Grav.*, 16:R159–R216, 1999.

[148] T. Nozawa, N. Stergioulas, E. Gourgoulhon, and Y. Eriguchi. Construction of highly accurate models of rotating neutron stars - comparison of three different numerical schemes. *Astron. Astrophys. Suppl. Ser.*, 132:431, 1998.

[149] J. R. Oppenheimer and G. M. Volkoff. On massive neutron cores. *Phys. Rev.*, 55:374–381, 1939.

[150] V. R. Pandharipande. Dens neutron Matter with Realistic Interactions. *Nucl. Phys.*, A174:641, 1971.

[151] V. R. Pandharipande. Hyperonic matter. *Nucl. Phys.*, A178:123–144, 1971.

[152] P. Papadopoulos and J. A. Font. Analysis of relativistic hydrodynamics in conservation form. 1999.

[153] A. Passamonti, M. Bruni, L. Gualtieri, A. Nagar, and C. F. Sopuerta. Coupling of radial and axial non-radial oscillations of compact stars: Gravitational waves from first-order differential rotation. *Phys. Rev.*, D73:084010, 2006.

[154] A. Passamonti, M. Bruni, L. Gualtieri, and C. F. Sopuerta. Coupling of radial and non-radial oscillations of relativistic stars: gauge-invariant formalism. *Phys. Rev.*, D71:024022, 2005.

[155] A. Passamonti, N. Stergioulas, and A. Nagar. Gravitational waves from nonlinear couplings of radial and polar nonradial modes in relativistic stars. *Phys. Rev.*, D75:084038, 2007.

[156] V. Pavlidou, K. Tassis, T. W. Baumgarte, and S. L. Shapiro. Radiative Falloff in Neutron Star Spacetimes. *Phys. Rev.*, D62:084020, 2000.

[157] E. Pazos et al. How far away is far enough for extracting numerical waveforms, and how much do they depend on the extraction method? *Class. Quant. Grav.*, 24:S341–S368, 2007.

[158] D. Pollney, C. Reisswig, L. Rezzolla, B. Szilágyi, M. Ansorg, B. Deris, P. Diener, E. N. Dorband, M. Koppitz, A. Nagar, and E. Schnetter. Recoil velocities from equal-mass binary black-hole mergers: A systematic investigation of spin-orbit aligned configurations. *Physical Review D (Particles, Fields, Gravitation, and Cosmology)*, 76(12):124002, 2007.

[159] J. A. Pons, E. Berti, L. Gualtieri, G. Miniutti, and V. Ferrari. Gravitational signals emitted by a point mass orbiting a neutron star: Effects of stellar structure. *Phys. Rev.*, D65:104021, 2002.

[160] W. H. Press. Long Wave Trains of Gravitational Waves from a Vibrating Black Hole. *Astrophys. J.*, 170:L105+, Dec. 1971.

[161] W. H. Press, S. A. Teukolsky, W. T. Vetterling, and B. P. Flannery. *Numerical Recipes in C, The Art of Scientific Computing.* Cambridge University Press, 2^{nd} edition, 1992.

[162] F. Pretorius. Binary Black Hole Coalescence. 2007.

[163] R. Price and K. S. Thorne. Non-Radial Pulsation of General-Relativistic Stellar Models. II. Properties of the Gravitational Waves. *Astrophys. J.*, 155:163, Jan. 1969.

[164] R. H. Price. Nonspherical perturbations of relativistic gravitational collapse. I. Scalar and gravitational perturbations. *Phys. Rev.*, D5:2419–2438, 1972.

[165] R. H. Price. Nonspherical Perturbations of Relativistic Gravitational Collapse. II. Integer-Spin, Zero-Rest-Mass Fields. *Phys. Rev.*, D5:2439–2454, 1972.

[166] T. Regge and J. A. Wheeler. Stability of a Schwarzschild singularity. *Phys. Rev.*, 108:1063–1069, 1957.

[167] L. Rezzolla et al. On the final spin from the coalescence of two black holes. *Phys. Rev.*, D78:044002, 2008.

[168] P. L. Roe. Approximate riemann solvers, parameter vectors and difference schemes. *J. Comput. Phy.*, 43:357, 1981.

[169] J. Ruoff. New approach to the evolution of neutron star oscillations. *Phys. Rev.*, D63:064018, 2001.

[170] J. Ruoff, P. Laguna, and J. Pullin. Excitation of neutron star oscillations by an orbiting particle. *Phys. Rev.*, D63:064019, 2001.

[171] M. Salgado, S. Bonazzola, E. Gourgoulhon, and P. Haensel. High precision rotating netron star models 1: Analysis of neutron star properties. *Astron. Astrophys.*, 291:155–170, Nov. 1994.

[172] M. Salgado, S. Bonazzola, E. Gourgoulhon, and P. Haensel. High precision rotating neutron star models. II. Large sample of neutron star properties. *Astron. Astrophys.*, 108:455–459, Dec. 1994.

[173] O. Sarbach and M. Tiglio. Gauge invariant perturbations of Schwarzschild black holes in horizon-penetrating coordinates. *Phys. Rev.*, D64:084016, 2001.

[174] E. Schnetter, S. H. Hawley, and I. Hawke. Evolutions in 3D numerical relativity using fixed mesh refinement. *Class. Quantum Grav.*, 21(6):1465–1488, 21 March 2004.

[175] S. L. Shapiro and S. A. Teukolsky. *Black holes, white dwarfs, and neutron stars: The physics of compact objects.* Wiley, New York, USA, 1983.

[176] M. Shibata. Numerical relativity. *Astronomical Herald*, 96:609–612, Nov. 2003.

[177] M. Shibata, M. D. Duez, Y. T. Liu, S. L. Shapiro, and B. C. Stephens. Magnetized hypermassive neutron star collapse: a central engine for short gamma-ray bursts. *Phys. Rev. Lett.*, 96:031102, 2006.

[178] M. Shibata, Y. T. Liu, S. L. Shapiro, and B. C. Stephens. Magnetorotational collapse of massive stellar cores to neutron stars: Simulations in full general relativity. *Phys. Rev.*, D74:104026, 2006.

[179] M. Shibata and T. Nakamura. Evolution of three-dimensional gravitational waves: Harmonic slicing case. *Phys. Rev. D*, 52:5428, 1995.

[180] M. Shibata and Y.-I. Sekiguchi. Gravitational waves from axisymmetrically oscillating neutron stars in general relativistic simulations. *Phys. Rev.*, D68:104020, 2003.

[181] M. Shibata and Y.-i. Sekiguchi. Gravitational waves from axisymmetric rotating stellar core collapse to a neutron star in full general relativity. *Phys. Rev.*, D69:084024, 2004.

[182] M. Shibata and Y.-i. Sekiguchi. Three-dimensional simulations of stellar core collapse in full general relativity: Nonaxisymmetric dynamical instabilities. *Phys. Rev.*, D71:024014, 2005.

[183] M. Shibata, K. Taniguchi, and K. Uryu. Merger of binary neutron stars with realistic equations of state in full general relativity. *Phys. Rev.*, D71:084021, 2005.

[184] M. Shibata and K. Uryu. Merger of black hole - neutron star binaries: Nonspinning black hole case. *Phys. Rev.*, D74:121503, 2006.

[185] M. Shibata and K. Uryu. Merger of black hole-neutron star binaries in full general relativity. *Class. Quant. Grav.*, 24:S125–S138, 2007.

[186] A. Stavridis and K. D. Kokkotas. Evolution equations for slowly rotating stars. *Int. J. Mod. Phys.*, D14:543, 2005.

[187] N. Stergioulas. Rotating stars in relativity. *Living Reviews in Relativity*, 6(3), 2003.

[188] N. Stergioulas, T. A. Apostolatos, and J. A. Font. Nonlinear Pulsations in Differentially Rotating Neutron Stars: Mass-Shedding-Induced Damping and Splitting of the Fundamental Mode. *Mon. Not. Roy. Astron. Soc.*, 352:1089, 2004.

[189] N. Stergioulas and J. L. Friedman. Comparing models of rapidly rotating relativistic stars constructed by two numerical methods. *Astrophys. J.*, 444:306, 1995.

[190] J. Stewart. *Advanced general relativity.* Cambridge University Press, 1991.

[191] F. D. Swesty. Thermodynamically consistent interpolation for equation of state tables. *J.Comput.Phys.*, 127(1):118–127, 1996.

[192] S. A. Teukolsky. *Astrophys. J.*, 185:635, 1973.

[193] S. A. Teukolsky. On the stability of the iterated crank-nicholson method in numerical relativity. *Phys. Rev. D*, 61:087501, 2000.

[194] K. S. Thorne. Non-radial Pulsation of General-Relativistic Stellar Models. III. Analytic and Numerical Results for Neutron Stars. *Astrophys. J.*, 158:1, Oct. 1969.

[195] K. S. Thorne. Nonradial Pulsation of General-Relativistic Stellar Models.IV. The Weakfield Limit. *Astrophys. J.*, 158:997, Dec. 1969.

[196] K. S. Thorne. Multipole Expansions of Gravitational Radiation. *Rev. Mod. Phys.*, 52:299–339, 1980.

[197] R. C. Tolman. Static solutions of einstein's field equations for spheres of fluid. *Phys. Rev.*, 55:364–373, 1939.

[198] K. Tominaga, M. Saijo, and K.-i. Maeda. Gravitational waves from a test particle scattered by a neutron star: Axial mode case. *Phys. Rev.*, D60:024004, 1999.

[199] K. Tominaga, M. Saijo, and K.-i. Maeda. Gravitational waves from a spinning particle scattered by a relativistic star: Axial mode case. *Phys. Rev.*, D63:124012, 2001.

[200] R. F. Tooper. General Relativistic Polytropic Fluid Spheres. *Astrophys. J.*, 140:434, Aug. 1964.

[201] R. F. Tooper. Adiabatic Fluid Spheres in General Relativity. *Astrophys. J.*, 142:1541, Nov. 1965.

[202] E. F. Toro. *Riemann Solvers and Numerical Methods for Fluid Dynamics.* Springer-Verlag, 2^{nd} edition, 1999.

[203] A. Trautmann, F. A. E. Pirani, and H. Bondi. *Lectures on general relativity.* Brandeis University Summer Institute in Theoretical Physics, 1964, Englewood Cliffs: Prentice-Hall, —c1965, edited by Trautmann, Andrzej; Pirani, F.A.E.; Bondi, Hermann, 1965.

[204] J. van Meter, J. G. Baker, M. Koppitz, and D.-I. Choi. How to move a black hole without excision: gauge conditions for the numerical evolution of a moving puncture. *Phys. Rev. D*, 73:124011, 2006.

[205] C. V. Vishveshwara. Scattering of Gravitational Radiation by a Schwarzschild Black-hole. *Nature*, 227:936–938, Aug. 1970.

[206] C. V. Vishveshwara. Stability of the schwarzschild metric. *Phys. Rev. D*, 1(10):2870–2879, May 1970.

[207] J. D. Walecka. A theory of highly condensed matter. *Annals of Physics*, 83:491–529, 1974.

[208] WHISKY Code Homepage. http://www.whiskycode.org/.

[209] R. B. Wiringa, V. Fiks, and A. Fabrocini. Equation of state for dense nucleon matter. *Phys. Rev.*, C38:1010–1037, 1988.

[210] T. Yamamoto, M. Shibata, and K. Taniguchi. Simulating coalescing compact binaries by a new code SACRA. 2008.

[211] J. W. York. Kinematics and dynamics of general relativity. In L. L. Smarr, editor, *Sources of gravitational radiation*, pages 83–126. Cambridge University Press, Cambridge, UK, 1979.

[212] S. Yoshida and Y. Kojima. Accuracy of the relativistic Cowling approximation in slowly rotating stars. *Mon. Not. R. Astron. Soc.*, 289:117–122, 1997.

[213] F. J. Zerilli. Effective potential for even parity Regge-Wheeler gravitational perturbation equations. *Phys. Rev. Lett.*, 24:737–738, 1970.